Nonlinear filters and deep learning for removing chest compression artifacts from electrocardiogram measurements during cardiac arrest

Sarah Delaja Verboom

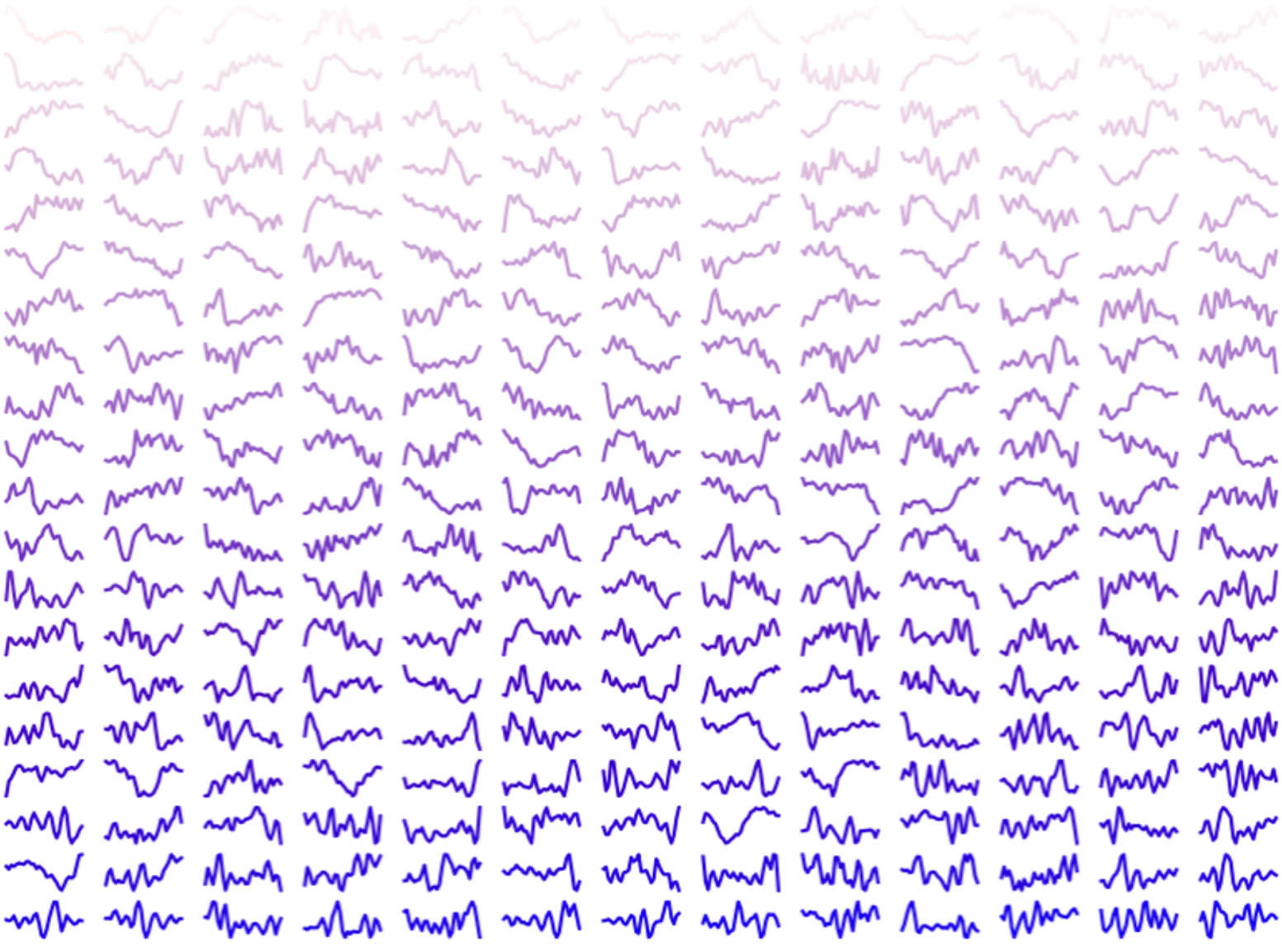

Nonlinear filters and deep learning for removing chest compression artifacts from electrocardiogram measurements during cardiac arrest

Master thesis

Sarah Delaja Verboom

Applied Mathematics & Technical Medicine

22 October 2020

Graduation committee

Chairman	Prof. dr. S.A. van Gils
Medical supervisors	Dr. M.A. Brouwer and J. Thannhauser MSc
Technical supervisor	Prof. dr. C. Brune
Process supervisor	R.J. Haarman MSc

UNIVERSITY OF TWENTE.

Radboudumc

Acknowledgements

Throughout the process of writing this thesis the past year, I received help and support from many people I would like to thank.

I would first like to thank my direct supervisor from the Radboudumc, Jos Thannhauser, who invested much time in helpful and also fun conversations with me. You were always enthusiastic and challenged me to question my results. I would also like to thank Marc Brouwer from the Radboudumc. You taught me to now and then stand back and look at my project in the bigger picture and to question the clinical relevance.

From the mathematics department of the University of Twente, I would like to thank Christoph Brune for your guidance in the past year. We had many long video calls in which you patiently helped me and always provided interesting new angles to my thesis. I would also like to thank Stephan van Gils. Even though we did not speak often, I want to thank you for your involvement in the project and your supervision from a distance.

The only supervisor who followed my professional development for multiple years is Rian Haarman. I would like to thank you for the interesting conversations. You helped me explore my strengths and weaknesses in my professional role.

During the first half of my internship at the Radboudumc, department of cardiology, I had the privilege to work with colleagues and other students. I always enjoyed the working environment there. There was always room for a good discussion or an informal chat with a cup of coffee. During the pandemic, I have worked from home with my lovely roommates, who have become my new 'colleagues' and supported me throughout the process.

Lastly, I would like to thank my family and friends for there patience with my sometimes long and puzzling stories. In particular, Yorick, who patiently listened to all my struggles and celebrated my accomplishments.

Summary

The key treatment actions of cardiac arrest include high-quality chest compression and quick defibrillation. Quick defibrillation is an effective treatment for so-called shockable underlying rhythms, which can be distinguished from non-shockable rhythms by analysis of the electrocardiogram (ECG). Unfortunately, chest compressions create artifacts in the ECG which impedes the analysis of the ECG. Interruptions of chest compressions are therefore necessary, however, pauses of the chest compressions decrease the chances of survival. The importance of continuing chest compressions on one side and ECG analysis on the other side poses a contradiction in the treatment of cardiac arrest. A solution to this contradiction would be to create a method that would allow interpretation of the ECG even during ongoing chest compressions.

Many methods have been proposed to remove chest compression artifacts from ECGs during resuscitation. Most existing filters are post-processing techniques based on the Fourier transform. However, the frequency spectra of chest compression artifacts and cardiac rhythms during cardiac arrest overlap considerably, leading to a problem in filtering in the frequency spectrum. A shift from Fourier based filters to filters based on a nonlinear transform could improve chest compression artifact reduction.

In this thesis, we generalize existing filter methods based on linear transforms to nonlinear alternatives such as nonlinear spectral analysis and deep learning-based methods. We proposed a deep learning-based filter from the field of audio processing. This neural network embeds a recurrent separation network that separates the chest compression artifact from the ECG in an autoencoder. The resulting filter learns both the transform (autoencoder) and a transfer function (recurrent network) and can operate nearly in real-time.

This introduced deep learning filter significantly improved the signal to noise ratio of artificially mixed ECG signals more compared to an existing linear Fourier based filter. Furthermore, the amplitude spectral area (AMSA) can be calculated after filtering artificially mixed ECG signals with only a small error after filtering. The association between pre-shock AMSA and shock success remained present for filtered ECG but with a different cut-off value. It remains unclear what the added value is of the deep learning filter on measured corrupted ECG signals.

To conclude, we have introduced a nonlinear deep learning method for removing chest compression artifacts from ECG measurements during cardiac arrest. This method has shown to improve the signal quality of artificially mixed ECG and can be further improved to be generalized to measured corrupted ECG.

Samenvatting

Borstcompressies en snelle defibrillatie zijn onderdeel van de belangrijkste behandelacties tijdens een circulatiestilstand. Snelle defibrillatie is een effectieve behandeling voor zogenaamde schokbare onderliggende ritmes, die door analyse van het elektrocardiogram (ECG) kunnen worden onderscheiden van niet-schokbare ritmes. Borstcompressies creëren echter verstoringen in het ECG die de analyse van het ECG belemmeren. Daarom zijn er onderbrekingen van borstcompressies noodzakelijk, maar tussenpozen van de borstcompressies verlagen de overlevingskans. Het belang van ononderbroken borstcompressies aan de ene kant en ECG-analyse aan de andere kant, vormt een tegenstrijdigheid in de behandeling van een circulatiestilstand. Een oplossing voor deze tegenstrijdigheid zou zijn om een methode te creëren die interpretatie van het ECG mogelijk maakt, ook tijdens borstcompressies.

Er zijn veel methoden gepubliceerd om borstcompressie verstoringen te verwijderen uit ECG's tijdens reanimatie. De meeste bestaande filters zijn nabewerkingstechnieken op basis van de Fouriertransformatie. De frequentiespectra van borstcompressie verstoringen en hartritmes tijdens een circulatiestilstand overlappen elkaar echter aanzienlijk, wat leidt tot een probleem bij het filteren in het frequentiespectrum. Een verschuiving van op Fourier gebaseerde filters naar filters op basis van een non-lineaire transformatie zou het filteren van de borstcompressie verstoringen kunnen verbeteren.

De geïntroduceerde deep learning filter verbetert de signaal-ruisverhouding van kunstmatig verstoorde ECG-signalen significant meer dan een bestaande op de Fourier transformatie gebaseerde filter. Bovendien kan de 'amplitude spectral area' (AMSA) worden berekend na het filteren van kunstmatig verstoorde ECG-signalen met slechts een kleine fout. De associatie tussen pre-shock AMSA en schoksucces bleef aanwezig voor gefilterde ECG, maar met een andere afkapwaarde. Het blijft onduidelijk wat de toegevoegde waarde is van de deep learning filter op echte verstoorde ECG-signalen.

Concluderend hebben we een non-lineaire deep learning-methode geïntroduceerd voor het verwijderen van borstcompressie verstoringen uit ECG-metingen tijdens een circulatiestilstand. Deze methode blijkt de signaalkwaliteit van kunstmatig verstoorde ECG-signalen significant te verbeteren en de methode kan nog verder worden verbeterd om generaliseerbaar te worden naar echte verstoorde ECG-metingen.

Contents

Abbreviations

ACD active compression-decompression.

ACF autocorrelation function.

AED automated external defibrillator.

AHA American Heart Association.

ALS advanced life support.

AMSA amplitude spectrum area.

AUC area under the curve.

BLS basic life support.

CC chest compression.

CLR coherent line removal.

CPR cardiopulmonary resuscitation.

DL deep learning.

ECG electrocardiogram.

EMD emperical mode decomposition.

EMS emergency medical services.

FC fully connected.

FFT fast Fourier transform.

IAP intra-arterial pressure.

ICA independent component analysis.

LMS least mean-square.

LSTM long short-term memory.

MC-RAMP multichannel recursive adaptive matching pursuit.

MSE mean squared error.

OHCA out-of-hospital cardiac arrest.

OR organized rhythm.

PCA principal component analysis.

PDE partial differential equation.

PEA pulseless-electrical activity.

PIT permutation invariant training.

PSD power spectral density.

pVT pulseless ventricular tachycardia.

RLS recursive least squares.

RNN recurrent neural network.

ROC receiver operating characteristic.

ROOR return of organized rhythm.

ROSC return of spontaneous circulation.

SAA shock advisory algorithm.

SNR signal-to-noise ratio.

SR sinus rhythm.

SVD singular value decomposition.

TTI transthoracic impedance.

TV total variation.

VF ventricular fibrillation.

VSS-LMS variable step size LMS.

CHAPTER 1

Introduction

Out-of-hospital cardiac arrests (OHCAs) are a major public health problem. In Europe, the incidence rate varies around 56 per 100,000 population per year and the chance of survival is low (8%, range 0-18) [1]. The key treatment actions include high-quality cardiopulmonary resuscitation (CPR) and quick defibrillation [2]. High-quality CPR mainly consists of chest compressions (CCs) aiming to maintain (oxygenated) blood flow to vital organs. Quick defibrillation is an effective treatment for so-called shockable underlying rhythms, which can be distinguished from non-shockable rhythms by analysis of the electrocardiogram (ECG). Unfortunately, CCs create artifacts in the ECG which impedes the analysis of the ECG [3, 4]. Interruptions of CCs are therefore necessary, to decide if defibrillation is the correct treatment [2, 5]. On contrary, pauses of the CCs decrease the chance of return of spontaneous circulation (ROSC) and lower chances of survival [6–8].

The importance of continuing CCs on one side and ECG analysis on the other side poses a contradiction in the treatment of OHCAs. A solution to this contradiction would be to create a method that would allow interpretation of the ECG even during ongoing CCs. This is not a novel idea, as many filters have been proposed to remove the CC-artifact from ECG recordings. Recently, some articles have been published that apply such a filter method as a pre-processing step before shock advice, resulting in a clinically applicable performance [9–13]. However, these good results were mostly due to changes in the shock advisory algorithm (SAA) rather than the filter method.

The main challenge with CC-artifact filters results from the transform they rely on, namely the Fourier transform. The frequency spectra of CC-artifacts and cardiac rhythms during cardiac arrest overlap considerably, leading to a problem in filtering based on the Fourier representation. Decreasing the presence of a frequency associated with CCs will partially remove CC-artifact, but will also lead to loss of the desired ECG signal. This type of filtering will always result in either signal loss or a residue of the CC-artifact, making it challenging to visually interpret the ECG signals and calculate representative waveform measures, such as amplitude spectrum area (AMSA). Furthermore, these techniques are all post-processing techniques unsuitable for (near) real-time implementation, which is needed for clinical implementation.

The solution to these challenges might lie in using a filter that is based on a different transform of the ECG than the Fourier transform, with less spectral overlap. In this thesis, we will generalize filtering with linear transforms to nonlinear transforms such as nonlinear spectral analysis and deep learning methods. We will propose a deep learning-based filter from the field of audio processing. This neural network embeds a recurrent separation network in an autoencoder. The autoencoder applies a learned nonlinear transform that can be used to gain a better understanding of the ECG signal. A recurrent network can then eliminate certain information in a signal, such as CC-artifacts, based on the temporal relationships in the signal. This filter will be tested on its ability to improve the diagnostic interpretation such as rhythm classification and ventricular fibrillation (VF) waveform interpretation.

Outline of thesis

This thesis will start with background information on OHCA treatment, characteristics of cardiac arrest ECGs, and the CC-artifact in Chapter 2. Then we will review the current state of published CC-artifact filter methods and conclude what the challenges and their possible solutions are in Chapter 3. In Chapter 4 we generalize these classical filters to nonlinear transforms and filters and propose a deep learning-based filter method. A simple explanation of the proposed filter is given in Appendix B. This method is then validated and compared to a classical filter on different ECG interpretation tasks in Chapter 5. In Chapter 6 we will test if the proposed method can preserve the predictive property of AMSA on shock success. This thesis will end with an overall discussion and conclusion in Chapter 7 and 8.

CHAPTER 2

Background

2.1 Out of hospital cardiac arrests

Cardiac arrest is a condition where the heart abruptly loses its contractility and the cardiac output stops. The chance of survival is dismal, varying around 8% (range 0-18%) [1]. There are many different causes of a cardiac arrest including cardiac and non-cardiac causes. The most common cardiac cause is ischemic coronary disease, commonly called a 'heart attack' [14]. Examples of irreversible cardiac causes are cardiomyopathies, valvular heart disease, and inherited arrhythmia's [14, 15]. There are also many reversible causes, of which most can be categorized in the four H's and T's: hypoxemia, hypovolemia, hypothermia, hyper/hypo electrolytes, tensionpneumothorax, tamponade, trombo-embolism, and toxicity.

All these causes can lead to cardiac arrhythmia's that do not produce cardiac output. These arrhythmia's can be categorized into two types based on the corresponding treatment: shockable and non-shockable rhythms, shown in Figure 2.1. Shockable rhythms include VF and pulseless ventricular tachycardia (pVT) and can be terminated by a defibrillator shock. VF is the most common first observed rhythm in cardiac arrests. During VF, the heart has a chaotic electrical activity that does not result in contractions but in a chaotic vibrating of the ventricles. With pVT, the electrical activity of the heart originates from a focus in the ventricles resulting in a wide complex tachycardia often deteriorating into VF. Non-shockable rhythms that can not be terminated by a defibrillator shock include pulseless-electrical activity (PEA), and asystole. In case of a PEA the electrical activity of the heart remains organized, but does not result in contractions with cardiac output. In the absence of any electrical cardiac activity the heart is in asystole.

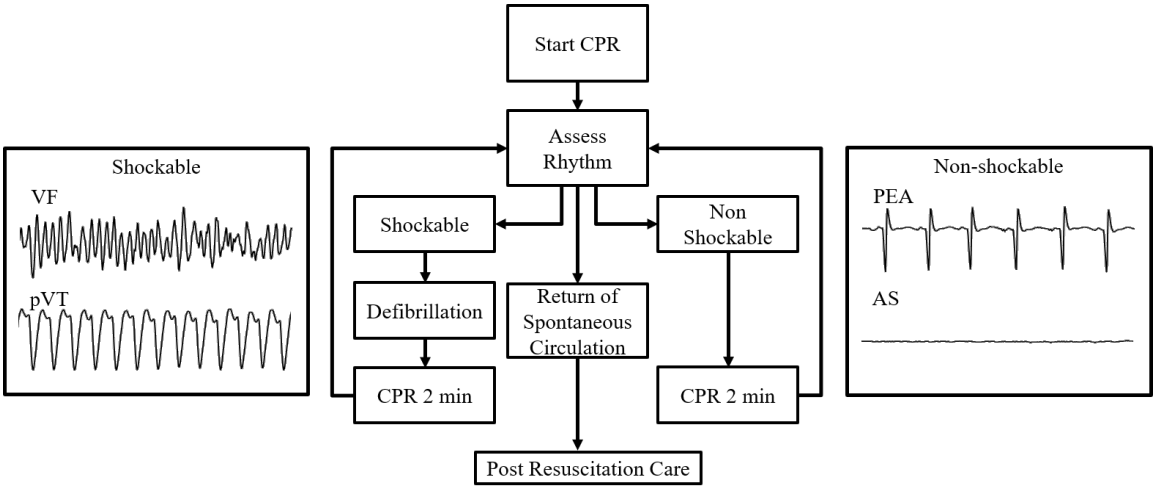

Figure 2.1. *Schematic overview of main action in the advanced life support (ALS) protocol (based on the European advanced life support (ALS) protocol [5]). With four-second examples of the different shockable and non-shockable rhythms from the OHCA-database previously described by Thannhauser et al. [16].*

2.1.1 Life support protocol

The Chain of Survival, shown in Figure 2.2, is the basis of the European guidelines for resuscitation and summarizes the vital links for the survival of a cardiac arrest. It consists of four vital shackles: early recognition and call for help, early CPR, early defibrillation, and post-resuscitation care. Early recognition of symptoms enables a rapid response of the emergency medical services (EMS) and fast

initiation of bystander CPR. A fast start of CCs by bystanders can double the chances survival [17–19]. Early defibrillation, for example by an automated external defibrillator (AED), can convert shockable cardiac rhythms to organized rhythms producing cardiac output. Finally, post-resuscitation care is needed to correct causal factors and maximize change of good neurological outcome.

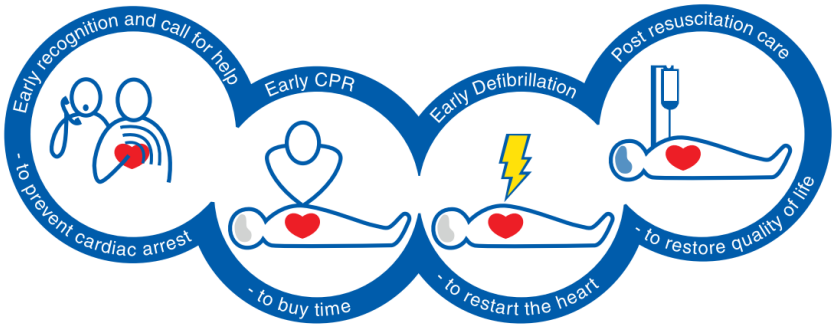

Figure 2.2. *The chain of survival (copied from the European Resuscitation Council Guidelines [2])*

After notifying the EMS, bystanders can start the basic life support (BLS) protocol. The protocol advises to start CPR immediately, consisting of alternating CCs and ventilations in a 30:2 ratio. Bystanders can also connect an AED if available, that can give a defibrillator shock. It is advised to continue CPR until the EMS arrive or the patient regains consciousness. In case of persistent cardiac arrest upon EMS arrival the ALS protocol is started, shown in Figure 2.1, consisting of cycles of 2 minutes. Each cycle consists of alternating CCs and ventilations in a 30:2 ratio. During CPR a defibrillator is connected with defibrillator pads to measure the ECG. After 2 minutes, CCs and ventilations are interrupted for a rhythm check. During a rhythm check the ECG signal is analyzed by the EMS personnel while palpating the pulse. There are some AEDs on the market that claim to filter the ECG and give a reliable ECG for analysis even during CCs [20]. Based on the observed rhythm, the treatment including medication (amiodarone and epinephrine) is adjusted and the 2 minute cycles are repeated until there is ROSC.

In case of a shockable rhythm, VF or pVT, ROSC can be achieved with a defibrillator shock. A shock of 150 to 360 Joule is given via the defibrillator pads or with handheld paddles. During charging of the defibrillator and immediately after the defibrillator shock, CPR is continued to minimize CC pauses. Both PEA and asystole are nonshockable rhythms, meaning that a defibrillator can not cause ROSC. In case of an organized rhythm with a palpable pulse or ROSC, the patient is transported to the hospital for post resuscitation care. During these cycles, the EMS also searches for possible reversible causes described by the four H's and T's.

During an OHCA, the cardiac rhythm can change over time. It is possible that a non-shockable rhythm spontaneously converts to a shockable rhythm and vice versa within a 2 minute cycle. These changes usually go unnoticed until the next rhythm check because changes are often hidden behind CC-artifacts. One of these changes that is especially of interest is the spontaneous return of VF after successfully terminating VF by a previous shock, called refibrillation or recurrent VF [21, 22]. It is hypothesized that the duration of refibrillation is inversely related to survival [23].

2.1.2 Chest compressions

The main purpose of CCs is to sustain a small blood flow to the vital organs. Following the guidelines, manual CCs should be delivered with a depth between 5 and 6 cm and a complete recoil after each compression [2]. The rate of compressions should be between 100 and 120 per minute with minimal interruptions [2]. Interruptions such as pre- and post-shock pauses shorter than 10 seconds and CC fraction above 60% are associated with improved outcomes [6, 8, 24, 25].

To this date, there is no consensus on the physiological mechanism of how CCs cause a blood flow. Two major theories exist, the cardiac pump mechanism and the thoracic pump mechanism [26]. The cardiac pump was the first hypothesis in 1960 [27]. It is based on the assumption that a CC results in

a compression of the ventricles between the sternum and spine, increasing the intraventricular pressure. The increased intraventricular pressure closes the atrioventricular valves and pushes the blood into the pulmonary artery and the aorta [28]. Later, an alternative theory was introduced, the thoracic pump [29]. In this hypothesis, a CC is believed to not only increase the intraventricular pressure, but the pressure of the whole intrathoracic compartment. All cardiac valves will remain open during compression and blood will be forced out of the thorax where pressure is lower. Retrograde venous flow is prevented by venous valves and collapsing of veins at the thoracic inlet.

In several studies, it has been attempted to find the mechanism of blood flow during CPR. Most of these studies used (contrast) transesophageal echocardiography to visualize opening and closing of the valves and flow direction during CPR [28, 30–33]. Although some other theories exist, the cardiac and thoracic pump were most supported. Cipani *et al.* hypothesized that the cardiac pump is the dominant mechanism in early CPR. In prolonged CPR the thoracic pump mechanism becomes more relevant when the myocardium stiffens [26].

In addition to manual CCs, mechanical CCs have become more common [34]. Mechanical CC devices can be divided into three different classes: mechanical pistons, load-distributing bands, and active compression-decompression (ACD) devices [26]. These three types are based on the different physiological mechanisms of CCs. Mechanical piston compress the chest mid-sternal and are most similar to manual chest compressions. These devices are mostly based on the cardiac pump theory. Newer mechanical devices such as load distribution bands and ACD devices are based on the thoracic pump theory. Load distribution bands compress a band around the thorax and thereby increase the intrathoracic pressure. ACD devices are semi-automatic and also introduce a negative intrathoracic pressure.

There is no consensus on the benefit of mechanical CC devices [26]. Based on three large randomized control trials [35–37], it is not recommended to use them routinely [5, 38]. However, there are situations where mechanical CC devices can be considered, for example, in prolonged attempts at resuscitation or in a situation where manual CCs are impractical or unsafe for the provider [5]. The AutoPulse is a load-distributing band that is used in some OHCA in the area of Nijmegen, and is also present in our dataset. With a CC-rate of 80±5 cpm, it delivers CCs outside of the range of the CPR protocol [39]. However, the CC depth is within the advised range with 20% of the anterior-posterior depth.

2.2 The electrocardiogram

The electrocardiogram (ECG) is an important noninvasive diagnostic tool that measures the electrical activity of the heart. The most common way to measure an ECG is with 10 electrodes (three limb electrodes, six precordial electrodes, and one ground electrode) resulting in a 12-lead ECG. Each lead represents a different view direction. During a cardiac arrest, there is no time to use ten electrodes in most cases. Instead, an ECG is measured using the defibrillator pads shown in Figure 2.3a. A single lead is enough to distinguish between the four main rhythm types.

Figure 2.3b shows a representative example of 40 seconds of ECG and TTI during cardiac arrest. At 85 seconds a shock is given to the observed VF, the shock causes extreme values in both measurements, making them unsuitable for analysis for a couple of seconds. In this example the shock is successful in returning organized rhythm (OR) as visible from 107 to 110 seconds. However, the heart rhythm returns to VF quickly during CCs.

ECG measurements are in the order of millivolts and are therefore vulnerable for disturbances. Abnormalities in the ECG that do not originate from the electrical activity of the heart are called artifacts [40]. artifacts can be caused by breathing or loose electrodes which create a low-frequency baseline wander. Other causes can be muscle activity, implanted electrical devices, or electromagnetic interference, these cause a high-frequency noise. Some of these artifacts are easily distinguishable from physiological electrical heart activity, while others are sometimes mistaken for abnormal heart activity.

The ECG is normally pre-processed before visual or automatic analysis, to remove some of these artifacts. Typically, a lowpass filter is applied to remove baseline wander, and a highpass filter to remove high-frequency disturbances from electromagnetic interference. Cut-off frequencies vary, with 0.1-1.0 Hz

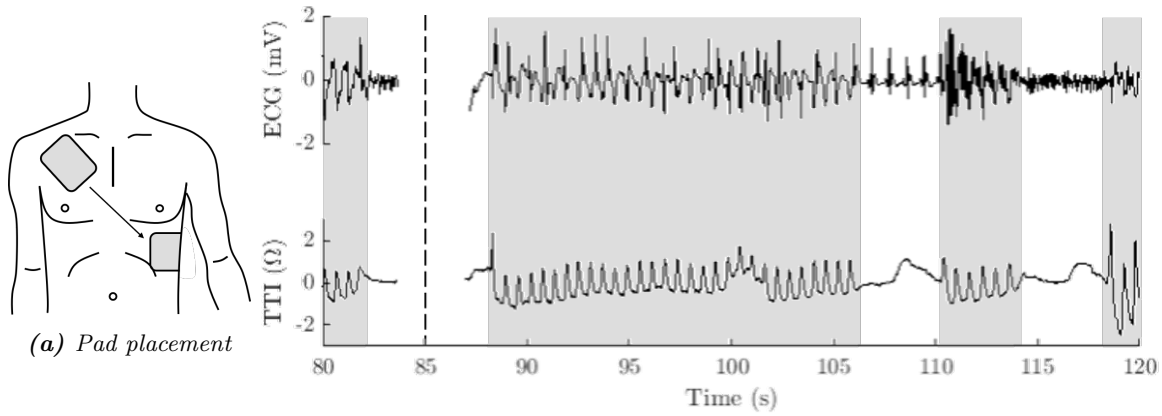

(a) Pad placement

(b) Example of measurements

Figure 2.3. *An example of a ECG measurement during out-of-hospital cardiac arrest (OHCA). Figure (a) shows the the placement of ECG electrodes (in gray), The arrow indicates the direction of the ECG measurement. Figure (b) shows an example of ECG and transthoracic impedance (TTI) measurements. The gray areas indicate presence of chest compressions (CCs) also visible by the waveforms in the transthoracic impedance (TTI). A shock was given at 85 seconds (indicated by the dashed line) causing measurements around that time to be absent.*

for the lowpass and 30-100 Hz for the high pass filter [41]. These filters remove most of the artifacts that are present during measurements where the patient does not move.

2.2.1 The chest compression artifact

Chest compressions (CCs) cause artifacts that are not removed by pre-processing, these artifacts are visible in Figure 2.3b in the gray areas. The CC artifact can have many different morphologies, Figure 2.4 shows several examples of the CC-artifact during asystole. Given the absence of cardiac electrical activity during asystole, it can be assumed that the ECG predominantly reflects the CC-artifact. As seen in the figure, there is a wide variety of CC-artifacts. There are not only differences in the CC-rate but also in the morphology of the artifact. Moreover, there is also a difference between CC-artifact caused by manual and mechanical CCs. Manual CCs cause a smoother, sine-like artifact with a variable frequency, whereas mechanical CCs have a fixed frequency and sharper transitions.

The power spectral densitys (PSDs) in figure 2.5 shows the frequency spectra of ECG-segments of our own OHCA-cohort, of which details have been described previously [16, 42] with different cardiac rhythms in the absence and presence of different CC-artifacts. The PSDs of asystole predominantly show the frequency spectra of the CC-artifacts. We found a fundamental frequency of 1.6-2.2 Hz (96-132 min^{-1}) for manual CCs, which approximates the optimal CC-rate as advised by the guidelines [2]. For mechanical CCs, we found a lower fundamental frequency of 1.4 Hz (84 min^{-1}) corresponding to the frequency of a mechanical CC device, in this case, the AutoPulse [39]. The total bandwidth of the CC-artifact is approximately 0-20 Hz for manual CC and 0-30 Hz for mechanical CCs.

Importantly, the bandwidth of the artifact overlaps with the bandwidth of the ECG signals of cardiac rhythms measured during cardiac arrest, making it difficult to filter CC with classic filter techniques. In accordance with previous studies on CC-artifact filtering, we distinguished three categories of cardiac rhythms during OHCAs: asystole, OR, and VF [43]. Organized rhythms include all rhythms with QRS-complexes (e.q. sinus rhythm, PEA, and ventricular tachycardia). Figure 2.5 illustrates a significant overlap in the frequency components of CC-artifacts and the ECG-signals of the cardiac rhythms.

There is a paucity of evidence on the underlying mechanisms of CCs and the resulting artifacts on the ECG. To date, there is only one study that has experimentally investigated the source of CC-artifacts. Fitzgibbon et al. used an experimental canine model and found that the skin-electrode interface causes a

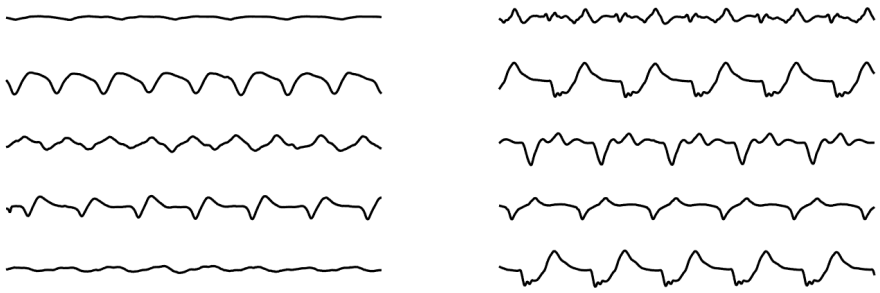

(a) *Manual CC* ***(b)*** *Mechanical CC*

Figure 2.4. *Ten examples of ECG-segments with chest compression artifacts (CC-artifacts) measured during asystole. Manual CC commonly create a smoother artifact with a higher fundamental frequency and a lower amplitude. Segments are from a cohort previously described [16, 42]. Mechanical chest compressions were given with a standard mechanical CC device (AutoPulse, Zoll Medical, Chelmsford, USA)*

significant part of the artifact [3]. Other studies confirmed that characteristics of the CC-artifact depend on the type of electrodes that were used [44]. Larger electrodes, defibrillator pads for example, have shown to cause a more profound artifact than smaller electrodes [3].

Most articles that published on CC-artifact filter methods, assumed the artifact to be an additive noise. Notably, with that assumption, there is no interaction between the CCs and the cardiac rhythm. In experimental canine studies, CC-artifacts were only visible on the surface ECG and not on the myocardial ECG [3], supporting the assumption of CC-artifacts to be an additive noise. In contrast, it has been shown in a porcine study that CC-artifacts differ when measured during different cardiac rhythms [44]. The latter finding suggests an interaction of the appearance of the CC-artifacts on the ECG and the underlying cardiac rhythm.

2.2.2 ECG interpretation

ECG measurements during cardiac arrest are not only useful to determine if a shock should be applied with a SAA. Especially in case of VF, the ECG holds more information about the patient. The VF waveform can be described by different quantitative VF-waveform measures. These measures can be defined in the time domain, the frequency domain, or both. Some VF-waveform measures are associated with shock success[16, 45], duration of cardiac arrest [46] and even the cause of cardiac arrest [46, 47]. VF with a higher amplitude and frequency, also called coarse VF, is more likely to be terminated by a defibrillator shock than fine VF with a lower frequency and amplitude [48–51].

Over the years, AMSA has gained increasing interest [16, 52, 53]. It is a measure that combines information of the frequency and amplitude [54] that is associated with shock success in retrospective studies [16, 48, 53]. A current international study is focussed on the real-time implementation of AMSA to guide defibrillation timing [55].

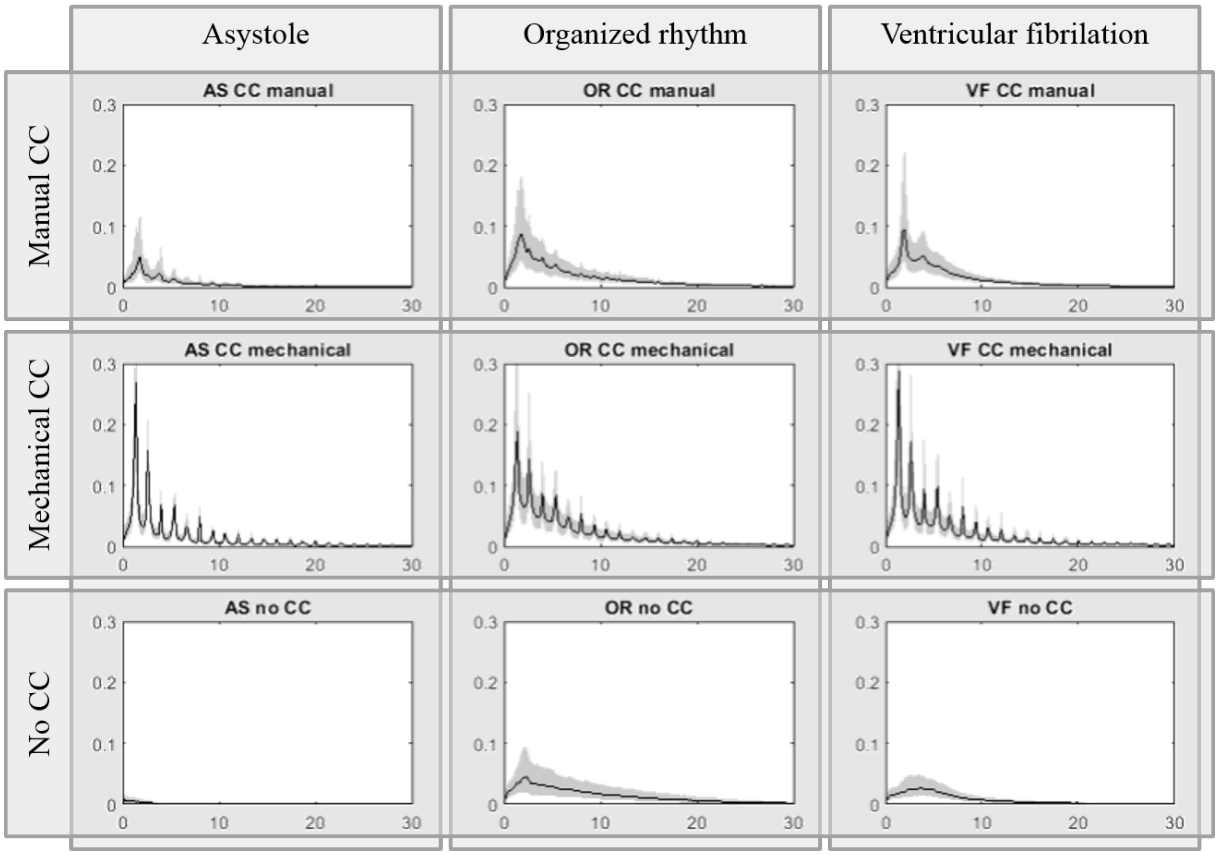

Figure 2.5. *Power spectral density (PSD) plots of electrocardiogram (ECG) signals of different cardiac rhythms during resuscitation. Differentiation has been made between ECG-segments without chest compression (CC), with manual CC and with mechanical CC. PSDs are presented as medians (black line) with interquartile ranges (gray area). The PSDs were calculated from 23,064 non-overlapping 5-second segments of 79 cardiac arrest events, from a cohort previously described [16, 42]. Mechanical chest compressions were given with a standard mechanical CC device (AutoPulse, Zoll Medical, Chelmsford, USA).*

CHAPTER 3

Existing filter methods for removing the chest compression artifact

3.1 Introduction

Removing CC-artifacts from ECG measurements during cardiac arrest is a difficult task, as discussed in the previous chapter. The first method to allow better ECG interpretation during CCs has been described in 1996 when Strohmenger et al. successfully removed CC-artifacts from porcine ECGs with a simple high-pass filter [56]. However, the frequency components of the underlying human ECG overlap with the frequencies of the CC-artifacts, making such filters inadequate [44]. Over the years, more sophisticated filter methods have been proposed to remove CC-artifacts from human ECGs. Existing reviews [43, 57, 58] on this topic only cover methods published up to 2012, but the performance of these filters has further increased since then. Recently, shock advice after new filter methods surpassed the minimum requirements of a sensitivity of 90% and specificity and 95% as set by the American Heart Association (AHA) [59]. The changes in the methodology that have led to this increased performance have not yet been analyzed and the steps that are needed to make CC-filtering clinically applicable, remain largely unknown. In this review, we provide an overview of the current progress of CC-artifact filtering from ECG data and aim to identify the challenges for the implementation of such algorithms into clinical practice.

3.2 Literature search

Literature was searched systematically for a complete overview of studies on CC-artifact filter methods. The Web of Science, Pubmed and Scopus databases were searched with the last search performed on April 7th 2020. Moreover, a manual search was performed of citations from primary articles. All articles were screened based on title and abstract and, if needed, assessed based on the full-text. All articles introducing a new method to remove or reduce CC-artifacts in human ECGs, to identify or quantify the underlying rhythm, were included. Excluded studies involved articles in which the methodology was not (sufficiently) explained, no human ECGs were used, or those written in a language other than English or dutch.

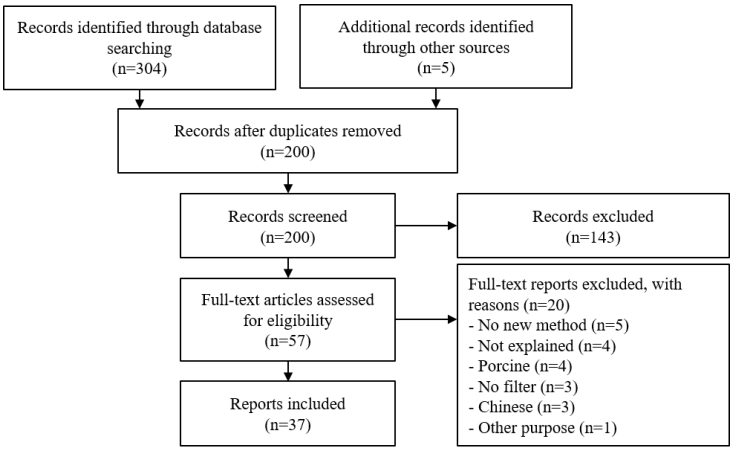

Figure 3.1. *Flow diagram of the inclusion of research articles.*

3.3 Results

The literature search provided 268 unique articles that were screened based on title and abstract, see Figure 3.1. Based on this screening, 56 articles were assessed based on full-text. Finally, 35 articles introducing 39 filter methods were included. An overview of the 39 introduced filter methods is shown in Table 3.1. Every filter method made several different choices in CC-artifact filtering. Figure 3.2 shows a schematic representation of the most important choices. The similarities and differences between the filter methods in these choices are described in this section.

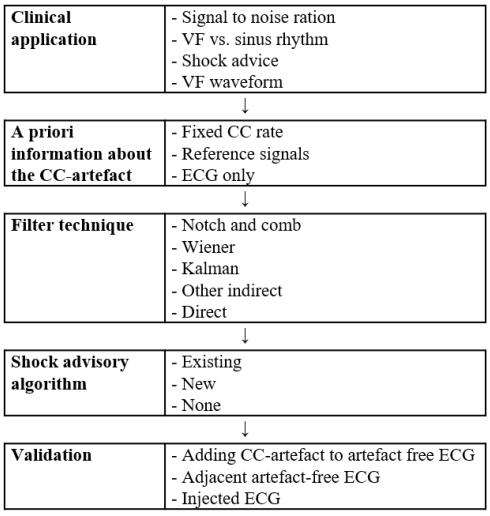

Figure 3.2. *Schematic overview of the choices in CC-artifact filtering. chest compression (CC); ventricular fibrillation (VF)*

3.3.1 Clinical application of filter methods

The application of the published filter methods can be divided into four categories: signal-to-noise ratio (SNR) improvement, VF and sinus rhythm (SR) classification, shock advice, and calculation VF waveform measures. Older articles aimed at increasing the SNR of corrupted ECG segments. Table 3.1 shows the absolute increase of the SNR for input signals with SNR=0, meaning that the power of the clean signal and the noise are the same. Although SNR is an important measure of signal quality, it does not fully quantify the quality of the ECG for clinical application. More recent articles tested the filtered ECG segments on rhythm recognition.

Most studies aimed to distinguish shockable and non-shockable rhythms. The categorization is done by an existing SAA that is suitable for clean ECG signals or by a newly introduced SAA that is tailored for filtered ECG signals. The performance of the categorization is shown in Table 3.1 with sensitivity and specificity. Sensitivity is the ability of the method to recognize shockable rhythms, specificity the ability to recognize non-shockable rhythms. The AHA advised a minimal sensitivity and specificity of 90 and 95% for a method to be clinically useful [59].

Only two articles focused on calculating VF waveform characteristics [60, 61]. Lo et al. [60] compared the AMSA of original and filtered ECG segments and found a strong relationship and an unchanged predictive property for shock success. However, cut-off values changed when the original SNR was low. Coult et al. calculated VF waveform measures directly from corrupted and clean ECG segments and evaluated their predictive property for survival and prognosis [61]. The predictive power for survival was not reduced for corrupted ECG segments compared to clean segments. However, the measures had a different cut-off point for corrupted and clean ECG segments.

Table 3.1. *Comparison of published a CC-artifact filter method for human ECGs up to June 2019. Studies are divided based on their application. If no reference signal was used, the method of extracting a priori knowledge is also noted in the filter method. The source of data was either from out-of-hospital cardiac arrest, clean ECG mixed with CC artifact, or human ECG 'injected' in a porcine model. CCs were administered Manual (Ma), Mechanical (Me), both (Bo) or were unspecified (Un). The sensitivity and specificity were based on filtered ECG segments. ΔSNR is the improvement of SNR for an input signal with SNR= 0.*

Study	Year	Ref	Method	Data	CC	Performance	
			VF waveform measures				
Coult[61]	2019	No	Direct (optimize parameters)	OHCA	Un		
Lo[60]	2013	No	Wiener (EMD + LMS)	Mixed	Ma		
			Shock advise			Sens	Spec
Isasi[9]	2019	No	Wiener (fixed LMS + new SAA)	OHCA	Me	97.5	98.2
Isasi[9]	2019	No	Wiener (fixed RLS + new SAA)	OHCA	Me	97.0	98.3
Isasi[10]	2019	No	Wiener (fixed RLS + new SAA)	OHCA	Me	91.7	98.1
Isasi[11]	2018	Depth	Wiener (RLS + new SAA)	OHCA	Ma	93.5	96.5
Alonso[62]	2018	Depth	Wiener (LMS)	OHCA	Un	90.3	66.4
Isasi[63]	2017	No	Wiener (fixed RLS)	OHCA	Me	99.0	87.3
Isasi[63]	2017	No	Wiener (fixed Goertzel)	OHCA	Me	97.0	80.2
Gong[64]	2017	TTI	Wiener (LMS + spike suppression)	OHCA	Un	90.8	92.1
Aramendi[12]	2016	TTI	Wiener (LMS)	OHCA	Me	97.6	95.9
Aramendi[12]	2016	No	Wiener (fixed LMS)	OHCA	Me	98.9	81.5
Aramendi[12]	2016	No	Fixed comb filter	OHCA	Me	97.9	84.1
Ayala[13]	2014	Depth	Wiener (LMS + new SAA)	OHCA	Ma	91.0	96.6
Babaeizadeh[65]	2014	TTI	Comb filter	OHCA	Un	84	95
Aramendi[66]	2012	TTI	Wiener (LMS)	OHCA	Un	95.4	86.3
Granegger[67]	2011	Multi	ICA	Injected	Ma	99.7	83.2
Ruiz[68]	2010	Depth	Kalman	OHCA	Un	93.3	89.1
Krasteva[69]	2010	No	Direct (BP + features + rule-based)	OHCA	Bo	90.1	85.9
Irusta[70]	2009	Depth	Wiener (LMS)	OHCA	Un	95.6	85.6
Ruiz de Gauna[71]	2008	No	PSD + Kalman	OHCA	Un	90.1	80.4
Li[72]	2008	No	Direct (wavelet + mean + AMSA)	OHCA	Un	93.3	88.6
Li[73]	2007	No	Direct (wavelet + mean + AMSA)	OHCA	Un	91.0	84.0
Eilevstjonn[4]	2004	Multi	Wiener (MC-RAMP)	OHCA	Un	96.7	79.9
			VF and sinus rhythm classification			Sens	Spec
Zhang[74]	2016	No	Wiener (PSD + LMS + new SAA)	Mixed	Ma	95.5	93.3
Yu[75]	2016	No	Wiener (EMD + LMS + new SAA)	Mixed	Un	92.7	81.2
Li[76]	2012	No	Direct (wavelet + mean)	OHCA	Un	91	85
Aramendi[77]	2007	No	Notch filter	Mixed	Ma	98.1	-
			Signal to noise ratio (VF)			ΔSNR	
Amann[78]	2010	No	CLR	Mixed	Me	8.0 $\pm$ 2.7	
Wherther[79]	2009	IAP	Gabor Mulitpliers	Mixed	Ma	7.0 $\pm$ 1.1	
Rheinberger[80]	2008	IAP	Kalman	Mixed	Un	7.9 $\pm$ 1.8	
Aramendi[81]	2005	No	Notch filter	Mixed	Un	4.8	
Irusta[82]	2005	Depth	Wiener (VSS-LMS)	Mixed	Un	5.9 $\pm$ 1.5	
Ruiz de Gauna[83]	2005	Depth	Kalman	Mixed	Bo	4.8 $\pm$ 1.2	
Rheinberger[84]	2005	No	ACF + Kalman	Mixed	Un	3.0 $\pm$ 1.1	
Ruiz[85]	2003	No	PSD + Kalman	Mixed	Ma	4.7 $\pm$ 0.7	
Husøy[86]	2002	Multi	Wiener (MC-RAMP)	Mixed	Ma	6.9	
Langhelle[44]	2001	Multi	Wiener	Mixed	Me	9.0 $\pm$ 0.7	
Aase[87]	2000	Multi	Wiener	Mixed	Me	3.3	

ACF: autocorrelation function; AMSA: amplitude spectrum area; CLR: coherent line removal; EMD: emperical mode decomposition; IAP: intra-arterial pressure; ICA: independent component analysis; LMS: least mean-square; MC-RAMP: multichannel recursive adaptive matching pursuit; PSD: power spectral density; RLS: recursive least squares; SAA: shock advisory algorithm; TTI: transthoracic impedance; VSS-LMS: variable step size LMS;

3.3.2 A priori information about the chest compression artifact

Most filter methods need a priori information about the CC-artifact. Important information is the fundamental CC-frequency representing the CC-rate or the presence of higher harmonics. There are different ways of gaining a priori information. Some studies use additional reference signals such as the TTI or compression depth derived from the acceleration of the defibrillation pads. Some studies even use invasive methods such as intra-arterial pressure (IAP) [79, 80]. Filters that do not require reference signals rely on the extraction of CC properties from the ECG itself.

The easiest and least adaptive method to get a priori information about the CC-rate is to assume that the frequency is constant (notated as 'fixed' in Table 3.1). Only seven methods rely on fixing the CC-rate [9, 10, 12, 63]. This is a strong assumption and only possible when CCs are administered by a mechanical device with a narrow bandwidth. The known CC-rate of the devices is used as a priori information, making the method dependent on the type of mechanical CC device. Most methods also assume a fixed number of harmonics, one method introduced a variable number of harmonics [10]. Filters that rely on a fixed CC-rate are not applicable to manual CC-artifacts due to the varying properties of the artifact.

A more adaptive method is to derive the mean CC-rate or a time-dependent signal that represents the CC-artifact from the ECG itself. The most common method to find the mean CC-rate is in the PSD of the ECG [71, 77, 78, 85]. This is often done in a certain frequency window around the expected CC-rate. Two published methods use the emperical mode decomposition (EMD) of the corrupted ECG [60, 75] to create reference signals. EMD is a nonlinear decomposition of the signal into intrinsic modes. The intrinsic mode functions are extracted from the highest local frequency to the lowest. One or more modes can be selected that represent the CC-artifact.

Other methods use a reference signal to get a time dependent CC-rate. Commonly, every compression instant $t_i = n_i/f_s$ is marked by a peak detector (and sometimes manually). Where f_s is the sampling frequency which is commonly 250Hz. One oscillatory cycle is identified as the time between two consecutive compressions. The frequency is assumed constant within one oscillatory cycle. This results in a piece-wise constant function of the CC-rate and phase

$$\psi(n) = \frac{2\pi}{\Delta n_i}(n - n_i) + i2\pi, \quad n_i \leqslant n < n_{i+1}. \tag{3.1}$$

Many filters use the fixed CC-rate, mean CC rate or time dependent CC-rate to create a model for the CC-artifact based on the article of Irusta et al. from 2005 [9–13, 60, 62, 63, 66, 68, 70, 71, 74, 82]. They proposed to model the CC-artifact as a Fourier series with the CC-rate as the fundamental frequency

$$\hat{\eta} = A(n) \sum_{k=1}^{M} \big(\alpha_k(n)\cos(k\psi(n)) + \beta_k(n)\sin(k\psi(n))\big), \tag{3.2}$$

where M is the number of harmonics included in the sum. An extra variable $A(n)$ is introduced to model when CCs are given and when there is a pause. $A(n)$ is one when there are CCs and zero when there is a pause. Rewriting the CC-artifact model as a vector multiplication shows that the CC-artifact is modeled with sine and cosine basis functions

$$\hat{\eta} = \underbrace{A(n)\begin{bmatrix}\cos(\psi(n)) & \dots & \cos(M\psi(n))\end{bmatrix}}_{\mathbf{b_1}^T(n)} \underbrace{\begin{bmatrix}\alpha_1(n)\\ \dots \\ \alpha_M(n)\end{bmatrix}}_{\mathbf{h_1(n)}} + \underbrace{A(n)\begin{bmatrix}\sin(\psi(n)) & \dots & \sin(M\psi(n))\end{bmatrix}}_{\mathbf{b_2^T(n)}} \underbrace{\begin{bmatrix}\beta_1(n)\\ \dots \\ \beta_M(n)\end{bmatrix}}_{\mathbf{h_2}(n)}, \tag{3.3}$$

where α_k and β_k are the filter coefficients that are updated each time step.

3.3.3 Filter techniques

All filters that are published can be divided into indirect and direct techniques. Direct techniques do not apply a filter first, but directly use the corrupted ECG for a specific application. However, most filters

are indirect, meaning a filter is applied to get an estimate of the clean ECG and then used for further applications. An elaborate explanation of each technique and comparison of the different implementations is included in Appendix A. Most included filter methods are adaptive filtering methods, which are suitable because the CC-artifact is non-stationary. During CPR the rescuer tires, switches to another rescuer, or to mechanical CCs. Most filters need a priori information about the CC-artifact and are applied at windows of 4.8 to 15 seconds.

Notch and comb

Notch and comb filters are the simplest filters and assume that the CC-rate is constant in a certain window. These linear filters remove or reduce the dominant CC-rate and in the case of comb filters also its higher harmonics. The disadvantage of these filters is that there is a relatively large loss of clean ECG signal. Furthermore, these filters assume that the CC frequency does not change in the analyzed window and are therefore less applicable when CCs are given manually.

Wiener

Most filters (20 out of 39) are based on the Wiener filter. The schematic representation of such a filter $\mathscr{H}$ with the use of a reference signal b is shown in Figure 3.3. Wiener filters assume that the CC-artifact η is strictly additive. The goal of this filter is to minimize a cost function of the difference between the actual artifact η and the estimation of the artifact $\hat{\eta}$ by adjusting the filter coefficients. With the assumption that x and (w, η) are uncorrelated, this is the same as minimizing a cost function of the difference between u and $\hat{\eta}$

$$C(h) = P(u - b^T h) = P(u - \hat{\eta}), \tag{3.4}$$

where P is some measure. Since u and w are both available signals, an optimal solution can be found. Wiener filters are well researched and there are many algorithms available (least mean-square (LMS), recursive least squares (RLS), multichannel recursive adaptive matching pursuit (MC-RAMP)) that can calculate the updates of the filter efficiently.

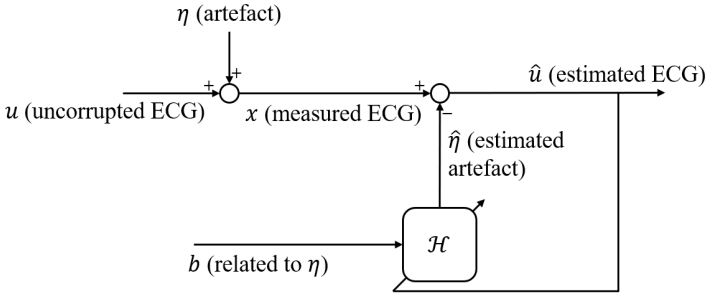

Figure 3.3. *Schematic representation of a Wiener filter with reference signal w. The uncorrupted ECG signal u is corrupted by the additive CC artifact η, which we measure as x. The filter $\mathscr{H}$ uses the reference signal b to create the estimation $\hat{\eta}$ of the artifact which is then subtracted from the measured signal x to get an estimate of the artifact free ECG $\hat{u}$.*

The reference signal b can be a measured signal or a created function. The most common reference signal b is described in Equation 3.3

$$b = A(n)\left[\cos(\psi(n)), \quad \ldots, \quad \cos(M\psi(n)), \quad \sin(\psi(n)), \quad \ldots, \quad \sin(M\psi(n))\right]. \tag{3.5}$$

Other options are using a measured reference signal and/or derivations of it [4, 44, 64, 86, 87] or manually selected empirical modes found by EMD [75]. The downside of a Wiener filter is that it can only remove parts of the signal that are a linear combination of the reference signal(s).

Kalman

A Kalman filter describes the ECG and CC interaction as a linear dynamical system. The goal is to estimate the state vector. The state vector resembles the vector in Equation 3.5 [68, 71], is another vector of sines and cosines [83, 85] or the last samples of the corrupted ECG. The dynamical system of the state vector is estimated based on assumptions of the dynamics. At each time step, the state vector is calculated based on the dynamical system and updated with the knowledge of the measured ECG. Kalman filters are relatively fast and provide an estimation of the quality of the filter. Unfortunately, it also assumes that the artifact is additive.

Other filters

Three other indirect techniques were only used by one article, independent component analysis (ICA), coherent line removal (CLR), and Gabor multipliers. ICA requires multiple ECG leads to reconstruct multiple independent sources. It assumes that the ECG leads are linear combinations of the sources. CLR is suitable to remove periodic signals with strong harmonics. The artifact is modeled as a sum of harmonic cosine wave with varying amplitude and slowly varying frequency. The filter based on Gabor multipliers strongly depends on a reference signal. It removes the frequencies that are strongly present in the reference signal.

Direct methods

Direct methods do not apply a filter to create an estimate of a clean ECG, but directly use the corrupted ECG for a specific application. These methods can therefore not be classified as filters. The application, mostly shock advice, is integrated into the method. A downside is that it is not possible for a physician to visualize the clean ECG. This makes it more difficult to check if the ECG with CC-artifacts is correctly interpreted by the algorithm.

3.3.4 Shock advisory algorithm

All indirect methods that have a shock advice application need an SAA to categorise the filtered ECG segments into shockable or nonshockable. Most methods use an existing SAA suitable for uncorrupted ECG to categorise shockable and non-shockable rhythms. Some of the more recent articles introduced a new SAA to categorise filtered ECG segments. Like most existing SAAs, these new SAAs shown in Table 3.2, are all nonlinear methods. Methods that implement a new SAA often show higher performance than comparable methods using an SAA designed for uncorrupted ECG segments. This indicates that a new SAA has a substantial influence on the shock advice performance.

Table 3.2. *Newly introduced shock advisory algorithm (SAA) for filtered ECG signals*

Study	Year	Method	Sens	Spec
Isasi[9]	2019	Wavelet + support vector machine	97.5	98.2
Isasi[10]	2019	RLS with multiple settings + existing SAA[88]	91.7	98.1
Isasi[11]	2018	Wavelet + random forest	93.5	96.5
Zhang[74]	2016	Phase space reconstruction	95.5	93.3
Yu[75]	2016	Neural network	92.7	81.2
Ayala[13]	2014	Energy + slope and frequency features + support vector machine	91	96.6

Studies that used a linear filter in combination with an SAA suitable for clean ECG, only have a linear method tailored to the artifact. The studies that added a new nonlinear SAA introduced a nonlinear part to handle the artifact. The trend that methods with a new SAA perform better suggests that the nonlinearity improves the performance. Indicating that the artifact might not be additive as is assumed in most articles.

3.3.5 Validation

There is no absolute knowledge about the true ECG during artifacts which makes it challenging to validate a filter method. Therefore, different validation methods are used for different applications. The validation methods used in literature can be divided into three types: using an adjacent artifact-free ECG segment, adding CC-artifacts to artifact-free ECG or 'injecting' human ECG into a porcine model.

Most articles use an artifact-free ECG segment before and/or after the CC interval. This validation assumes that the rhythm does not change during these segments and therefore, the rhythm is the same in the artifact-free segments as in the corrupted segments. This validation method is suitable for shock advice or rhythm classification. It does not assume any type of interaction of the CCs on the ECG. Unfortunately, it is not suitable for segments with rhythm changes such as refibrillation and it does not allow for calculation of distance measures, such as SNR.

The second validation method uses artificially mixed signals. ECG measurements, from animals or humans, with CCs during asystole are used as a representation of the pure CC-artifact. These segments are added to human artifact-free ECG measurements. This provides sets of ECG measurements with and without CC-artifacts. This mixing method is suitable for calculating the SNR because there is a ground truth of what the output of the filter should be. The downside of this method is the assumption that the CC-artifact is additive, and that the SNR of the input signal is chosen manually.

The last method is only used by Granegger et al. [67]. They used a porcine model in combination with human ECG. Sequences of human ECG during OHCA were converted to analogue signals. These signals were 'injected' close to the porcine heart. An ECG was measured on the skin of the pig with and without CCs. This method provides two measurements with an identical underlying rhythm but one with and one without CC-artifacts, without any assumptions on the mechanism of CC-artifacts. This validation method is suitable for all applications.

3.4 Discussion

Removing CCs from ECG measurements during cardiac arrest is proven to be a difficult task. The frequency spectra of the ECG measurement and CC-artifact overlap considerably. This review compared 39 published methods attempting to remove or reduce the CC-artifact from ECG. The majority of these methods (28 out of 39) rely on a Fourier representation of the CC-artifact, and sometimes also the clean ECG. Most articles follow the same filter techniques, with more than half using a method based on the Wiener filter. We also see a shift from methods with reference signals to methods without reference signals or only using readily available signals such as TTI or compression depth. Moreover, newer articles often use OHCA data and are more focused on shock advice rather than restoring SNR which is more common for older studies. There are already AEDs on the market with integrated filter methods by ZOLL. Tan et al. [20] evaluated its performance but did not elaborate on the filter method in the article and was therefore excluded from this review.

In recent years, the performance of filter methods has improved. The sensitivity and specificity standards of the AHA are met by six methods, shown in Table 3.3. Most articles that meet these high standards introduced a new SAA rather than adapting the method of filtering. The three most recent methods introduced by Isasi et al. [9, 10] relied on a fixed CC frequency. This was possible due to the usage of mechanical CCs by the LUCAS device. Unfortunately, this limits the applicability of these filter methods in clinical practice. Mechanical chest compressions are not possible in every situation or for every patient. Aramendi et al.[12] introduced a filter method that does not rely on a fixed CC-rate, but only tested their filter on ECG data that was corrupted by mechanical CCs. artifacts originating from mechanical CCs are more time-invariant and therefore easier to remove from corrupted ECGs. Studies applying the filter method on manual chest compressions as well are necessary to evaluate performance in a more realistic setting. The other two methods by Isasi et al. [11] and Ayala et al. [13] are most likely to be clinically applicable because they do not rely on specific a priori information and were tested on manual CCs. The only difficulty with implementing these methods is the dependency on compression depth which is not measured in most cases [43].

Table 3.3. *Subset of methods of Table 3.1 that meet the performance requirements set by the AHA of a minimal sensitivity of 90% and specificity of 95%.*

Study	Year	Ref	Method	Data	CC	Rhythm	Sens	Spec
Isasi[9]	2019	No	Fixed LMS + new SAA	OHCA	Me	All	97.5	98.2
Isasi[9]	2019	No	Fixed RLS + new SAA	OHCA	Me	All	97.0	98.3
Isasi[10]	2019	No	Fixed RLS + new SAA	OHCA	Me	All	91.7	98.1
Isasi[11]	2018	Depth	RLS + new SAA	OHCA	Ma	All	93.5	96.5
Aramendi[12]	2016	TTI	LMS	OHCA	Me	All	97.6	95.9
Ayala[13]	2014	Depth	LMS + new SAA	OHCA	Ma	All	91.0	96.6

LMS: least mean-square; RLS: recursive least squares; SAA: shock advisory algorithm; TTI: transthoracic impedance;

One of the main reasons to develop a CC-artifact filter is to minimize interruptions of CCs, but there are also other methods for this goal that are published or suggested. There are three other approaches found in the literature. The first approach is to use short segments without artifacts, such as ventilation pauses, for an SAA suitable for short segments [89]. This approach is an improvement on the current situation but still requires CC pauses and is unable to continuously monitor the heart rhythm. The second approach is to use multiple segments for shock advice: filtered ECG segments and a clean ECG segment for confirmation. This gives more certainty of the shock advice than solely using filtered ECG and only requires a short interruption [90, 91]. The last approach is closest to evaluating the rhythm during ongoing CCs. This approach is based on an SAA that uses filtered ECG segments to decide if the rhythm is shockable, non-shockable, or that it is uncertain. Then it advises the rescuer to pause CCs to analyze the clean ECG for a definite shock advice [65].

All well-performing filters are only accessed by their ability to get reliable shock advice based on the ECG. Although shock advice is clinically very important, it does not accurately represent the performance of the filter. Most filters still represent the CC-artifact in the frequency space or rely on frequency-based filter methods, even though the frequency spectra of CC-artifacts and cardiac rhythms during cardiac arrest overlap considerably. Decreasing the presence of a frequency associated with CCs will partially remove CC-artifact, but will also lead to loss of the desired ECG signal. This type of filtering will always result in either signal loss or a residue of the CC-artifact in the ECG estimate. Shock advice after such filtering might be possible, especially when the SAA is learned to cope with these residual CC-artifacts. However, the visual interpretation of the ECG estimate is presumable still difficult.

Furthermore, the techniques that perform well either fix the CC-rate which are not applicable in a clinical setting or require extensive a priori knowledge of the CC-artifact such as the phase described in Equation 3.1. The derivation of the time-dependent phase is only possible in post-processing. To make ECG interpretation possible during CPR, CC-artifact filtering must be implemented as a (near) real-time filter. The designs of the current filters are unsuitable for real-time applications since they need a large window (4.8 - 15 seconds) to apply the filter to. The window-based filtering also discards most temporal relationships in the signal, that might be of added value in filtering.

The solution to these challenges might lie in using a filter that is based on a different transform of the ECG than the Fourier transform where the spectral overlap is less. The results of this review show that the performance is improved for methods that use a nonlinear SAA which are specifically designed for filtered ECG signals. This suggests that nonlinear decomposition could potentially be a more suitable way of segmenting CC-artifacts from corrupted ECG signals. Furthermore, a filter that also considers temporal relationships might be applicable in real-time. Lastly, Better knowledge of the origin of the CC-artifact could give more insight into the interactions between the CCs, the ECG registration, the heart rhythm, the patient, and the resulting artifact. Understanding these interactions is valuable when designing CC-artifact filters.

3.5 Conclusion

Many methods have been proposed to remove CC-artifacts from ECGs during resuscitation. In the last five years, the sensitivity and specificity of shock advice based on filtered ECG segments surpassed the AHA requirements. Despite shock advice being the major clinical application after CC-artifact filtering, it is not a complete measure to evaluate filter performance. The majority of filter methods rely on the Fourier transform. However, the frequency spectra CC-artifacts and ECG during cardiac arrest largely overlap. A shift from Fourier based filters to filters based on another transform could improve CC-artifact reduction. The results of this review suggests that a nonlinear decomposition could potentially be a more suitable way of segmenting CC-artifacts from corrupted ECG signals.

Additionally, all included methods are post-processing techniques. In order to make a filter method clinically applicable, the filter method should be able to operate (near) real-time. Considering temporal relationships might aid in doing so. Lastly, greater knowledge of the origin of the CC-artifact could give more insight into the interactions between the CCs, the ECG registration, the heart rhythm, the patient, and the resulting artifact. Understanding these interactions is valuable when designing CC-artifact filters.

CHAPTER 4

From linear to nonlinear filter techniques

4.1 Introduction

The previous chapter gave an overview of current filter methods to filter out the CC-artifact from cardiac arrest ECG measurements. Current filter methods are mostly linear filters relying on the Fourier transform or are closely related to it. However, the spectra of clean ECGs and CC-artifacts overlap considerably, making it hard to filter correctly. In this chapter, we will generalize linear filters including the much-used Wiener filter from the previous chapter. Then, we will introduce nonlinear filter methods based on different transforms with increasing complexity. Finally, we will introduce a deep learning-based filter, that could potentially also filter near real-time.

Linear filters can be described as a three-step process. The discrete case is schematically drawn in Figure 4.1. The first step is to transform the time dependent input signal $x(t)$ with a transform function T into a linear combination of basic building blocks

$$y(\tau) = T[x(t)](\tau). \tag{4.1}$$

The transformation $y(\tau)$ depends on a new variable τ which can have multiple meanings depending on the chosen transform. A transformation of the input signal is not only useful for filtering, but can also be used to gain insight into properties of the signal. A common example is the Fourier transform where τ represents the frequency and $|y|$ is a spectrum of the presence of each frequency in the signal. The second step is to filter y in the new dimension with a transfer function $H(\tau)$. With the third step, the inverse transform T^{-1} is applied to return to a time-dependent signal

$$x^H(t) = T^{-1}[H(\tau)y(\tau)](t). \tag{4.2}$$

In the classical sense, a transfer function only depends on τ. However, there can be ways of filtering where the transfer function also depends on t or even the input signal x or its transform y.

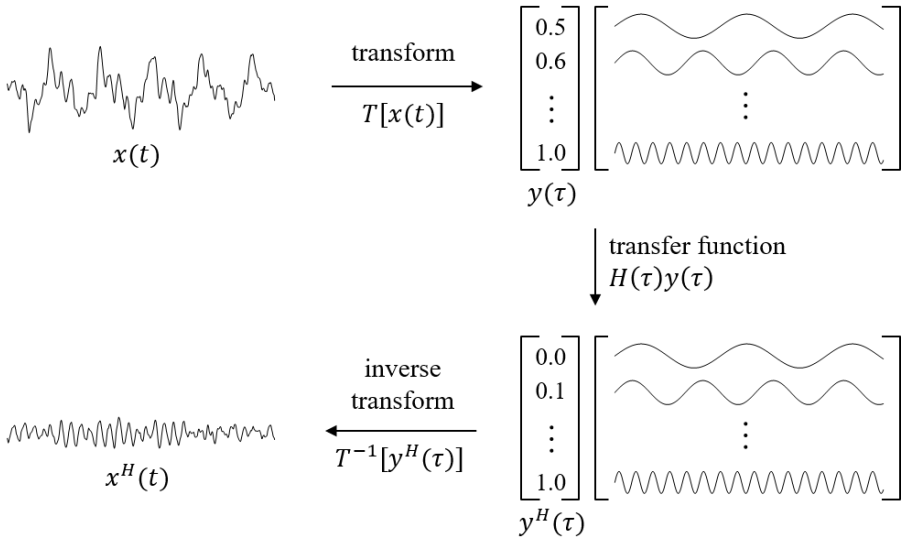

Figure 4.1. *Schematic overview of filtering a signal $x(t)$ based on a transform T of the signal. The transform returns a representation of the input as a linear combination of basis signals, in this case sine waves. The transfer function $H(\tau)$ amplifies some basis functions while reducing others. Afterwards, the filtered signal can be reconstructed by applying the inverse transform T^{-1}.*

Most existing CC-filters are based on the Fourier transform or are closely related to it. The Fourier transform is a linear transform that represents the input signal as a linear combination of sine and cosine functions of increasing frequency. The continuous Fourier transform and its inverse can be described by

$$X(f) = \mathscr{F}[x(t)](f) = \int_{-\infty}^{\infty} x(t)e^{-2\pi ift}\ \mathrm{d}t. \tag{4.3}$$

$$x(t) = \mathscr{F}^{-1}[X(f)](t) = \int_{-\infty}^{\infty} X(f)e^{2\pi ift}\ \mathrm{d}f. \tag{4.4}$$

If the input is a multiple pure sine or cosine with frequency f, the Fourier spectrum will be a Dirac delta function at the corresponding frequency f. The transfer function $H(f)$ can be defined such that only certain frequencies and phases remain in the filtered output. A common and simple version of this is a high-pass filter that removes low frequency components such as baseline wander. The transfer function $H(f)$ is zero for low frequencies up to a cut-off frequency f_c and 1 for higher frequencies

$$x^H(t) = \mathscr{F}^{-1}[H(f)X(f)](t) = \int_{f_c}^{\infty} X(f)e^{2\pi ift}\ \mathrm{d}f. \tag{4.5}$$

In the result frequencies below f_c are removed. Other examples are low-pass or band-pass filters. The transfer function is typically a more smooth function with a certain gain and phase for every frequency.

4.2 Wiener filter

In Chapter 3 we found the Wiener filter to be a popular choice for filtering out the CC-artifact. The classical Wiener filter is a linear filter that assumes that the input signal $x(t)$ is a summation of the desired signal $s(t)$ and an uncorrelated noise $\eta(t)$

$$x(t) = s(t) + \eta(t). \tag{4.6}$$

Assuming that both signals are linear stochastic processes with known spectral characteristics, the Wiener filter computes a statistical estimate using

$$\hat{s}(t) = \mathscr{H}(x(t)), \tag{4.7}$$

where $\mathscr{H}$ depends on the variance of the desired signal and the noise signal. However, these variances are not always known and are therefore assumed or estimated.

The classical Wiener filter can also be described as a partial differential equation (PDE), using the heat equation

$$\partial_\tau u(t,\tau) = C(\tau)\Delta u(t,\tau), \quad u(t,0) = x(t), \tag{4.8}$$

where $\Delta u = \frac{\partial^2 u}{\partial t^2}$ to easily generalize to the case where u is two or three dimensional. The solution $u(t,\tau)$ at a certain diffusion time τ [92] is the filtered signal that approximates $s(t)$. The coefficient C depends on the expected variance of the noise $\sigma^2_{\eta,\tau}$ and the estimated variance of the clean signal $\tilde{\sigma}^2_s$

$$C(\tau) = \frac{\sigma^2_{\eta,\tau}}{\tilde{\sigma}^2_s + \sigma^2_{\eta,\tau}}. \tag{4.9}$$

However, more often a locally adaptive version of the Wiener filter is used where the estimated variance of the clean signal $\tilde{\sigma}^2_s$ is locally approximated, making C dependent on t.

In CC-artifact filtering the Wiener filter is used in a slightly different form. Instead of filtering the measured signal where the spectral characteristics have to be assumed, it filters one or more reference signals $b(t)$ that are related to the CC-artifact to estimate the CC-artifact as described in Section 3.3.3. In that way no assumptions need to be made on the spectral characteristics. The corresponding heat equation remains the same up to the initial condition

$$\partial_\tau u(t,\tau) = C(\tau)\Delta u(t,\tau), \quad u(t,0) = b(t), \tag{4.10}$$

where $b(t)$ is a chosen reference signal. The estimate of the clean ECG signal $\hat{s}(t)$ is not given by the solution $u(t,\tau)$ at a certain τ, but by

$$\hat{s}(t) = x(t) - u_*(t;\tau). \tag{4.11}$$

In Section 3.3.2 we showed the most popular choice of reference signals $b(t)$ to be multiple reference signals equal to a Fourier series of higher harmonics of the CC-rate. However, instead of using a classical Fourier series, the input CC-artifact is assumed to be a linear combination of sine and cosine functions with a time-dependent frequency based on the varying CC-rate. To accomplish that, a time-dependent phase is used described in Equation 3.1, which is based on the detection of CCs in a measured reference signal or the ECG. This way of filtering allows for more adaptive cancellation of the CC-artifact.

A Wiener filter with using this type of reference signal can be related to a classical linear filter based on the Fourier transform with a time dependent transfer function $H(f,t)$. The transfer function reduces the time-dependent CC-frequency $f_0(t)$ and its higher harmonics in the ECG

$$x^H(t) = \mathscr{F}^{-1}[H(f,t)X(f)](t). \tag{4.12}$$

$$H(f,t) = \begin{cases} \alpha & \text{if } f = kf_0(t) \\ 1 & \text{else} \end{cases}, \tag{4.13}$$

where $\alpha < 1$ is iteratively optimized by a algorithm. The time-dependent CC-frequency can be described as a piecewise constant function assuming that the CC-frequency remains constant during one CC.

4.3 Nonlinear spectral decomposition

Recently, filtering with linear spectral transformations such as Fourier or Wavelet transforms in the classical sense as described by Equation 4.2 has been generalized to filtering with a nonlinear spectral representations. One of the nonlinear spectral representations was made by Gilboa [93, 94] using the total variation (TV) with a scale space or gradient flow

$$-\partial_\tau u(t,\tau) = p(t,\tau), \qquad p(t,\tau) \in \partial_u J(u), \qquad u(t,0) = x(t), \tag{4.14}$$

where $\partial J(\cdot)$ denotes the subdifferential of J. The regularization functional J was defined as the TV functional which is defined as

$$J_{TV}(u) = \int_\Omega |\nabla u(\tau)| \, \mathrm{d}\tau, \tag{4.15}$$

for smooth enough u ($\nabla u \in L^1$), here $\nabla u = \frac{\partial u}{\partial t}$. Burger et al generalized this type of spectral representation for J being a one-homogeneous functional [95]. One-homogeneous functionals between to vector spaces over real numbers are defined by their property

$$J(\alpha u) = \alpha J(u), \quad \alpha > 0. \tag{4.16}$$

The choice of the regularization functional J determines the type of decomposition. The functional J can also be chosen in such a way that the nonlinear spectral decomposition resembles a Fourier of Wavelet transform.

The gradient flow described in Equation 4.14 is not the only method to create a nonlinear spectral decomposition [95]. It can also be defined using the variational method

$$u(\tau) = \arg\min_u \frac{1}{2}\|u - x\|_2^2 + \tau J(u). \tag{4.17}$$

This is a minimization consisting of two parts, a data fidelity term $\frac{1}{2}\|u - x\|_2^2$ to keep u similar to x and some regularization functional $J(u)$, which is a convex one-homogeneous functional. The variational

method shows the same behavior as the gradient flow methods. Both method result in $u(0,t) = x(t)$, and if $x(t)$ is an eigenvector defined by

$$\lambda u \in \partial J(u) \tag{4.18}$$

$u(\tau, t)$ will linearly loose contrast, and vanish at $\tau = 1/\lambda$. The third option is the inverse scale space flow

$$\partial_s p(t,s) = x(t) - u(t,s), \qquad p(s) \in \partial_u J(u(t,s)), \qquad u(t,0) = 0. \tag{4.19}$$

The behavior of the inverse scale space flow differs from the other two methods on two points. First, the diffusion process of $u(t,s)$ is reversed, $u(t,s)$ converges back to the input signal $x(t)$. Second, if $x(t)$ is an eigenfunction the solution will result in a piecewise constant function with the singularity at $s = \lambda$. In this section we will use the variational method as it is most intuitive.

The solution of Equation 4.17 for a fixed τ can be seen as a diffusion filtering itself. When the TV functional is used this is known as the ROF model, or TV denoising where noise with a high TV is removed while retaining edges in the input signal or image. The solution ROF model can also be described as a PDE

$$\partial_\tau u = \nabla \cdot \frac{\nabla u}{|\nabla u|}, \quad u(t,0) = x(t). \tag{4.20}$$

This closely relates to nonlinear diffusion filtering proposed by Perona and Malik [96], which is given by the following PDE

$$\partial_\tau u = \nabla \cdot (g(\nabla u)\nabla u), \quad u(t,0) = x(t) \tag{4.21}$$

In case of TV denoising $g(\nabla u) = \frac{1}{\nabla u}$. In the specific case where $g(\nabla u, \tau) = C(\tau)$, the nonlinear diffusion will relate to the classical Wiener filter.

If $x(t)$ is a nonlinear eigenfunction of J by the definition of Equation 4.18, the variational method will have the solution

$$u(t,\tau) = \begin{cases} (1-\tau\lambda)x(t) & \text{for } t \leqslant \frac{1}{\lambda} \\ 0 & \text{else} \end{cases}. \tag{4.22}$$

In Fourier transforms, the nonlinear eigenfunctions $e^{2\pi i f t}$ appear as a Dirac delta function at the corresponding frequency. The nonlinear spectral transform was defined by Gilboa [93, 94] in a way to keep this property

$$\phi(t,\tau) = \tau \partial_{\tau\tau} u(t,\tau). \tag{4.23}$$

This transform is sometimes called a wavelength decomposition since it returns Dirac delta functions at $1/\lambda$ of the corresponding eigenvectors present in the input signal.

As with linear spectral transformations, the original signal can be completely reconstructed from the wavelength decomposition by an inverse transformation. The inverse transformation of a nonlinear spectral transformation is defined as a integration over the regularization parameter τ

$$x(t) = \int_0^\infty \phi(t,\tau)\ \mathrm{d}\tau. \tag{4.24}$$

Filtering can be done analogous to filtering with linear methods described in equation 4.2 by

$$x^H(t) = \int_0^\infty H(\tau)\phi(\tau,t)\ \mathrm{d}\tau. \tag{4.25}$$

The filtered function $x^H(t)$ is a version of the input where some eigenfunctions are amplified and others are diminished. If we translate this to the ECG case, $x^H(t)$ can be the ECG without CC-artifacts.

The wavelength decomposition can be visualized by a spectrum amplitude $S(t)$. In the case of a Fourier transformation, the spectrum is the absolute value of the Fourier transform. The nonlinear spectral response function can be defined in several ways, examples of them are

$$S_1(\tau) = \|\phi(t,\tau)\|_{L^1(\Omega)} = \int_\Omega |\phi(t,\tau)|\ \mathrm{d}t, \tag{4.26}$$

$$S_2^2(\tau) = \tau^2 \frac{\partial^2}{\partial \tau^2} J(u(\tau)) = \langle \phi(t,\tau), 2\tau p(t,\tau) \rangle, \tag{4.27}$$

$$S_3^2(\tau) = \langle \phi(t,\tau), x \rangle. \tag{4.28}$$

The spectrum amplitude is not only important to visualize the wavelength decomposition but can also help to differentiate between different patterns in the ECG.

Figure 4.2 shows the mean spectra for clean ECG segments and CC-artifact where $J(u)$ is the TV functional. In the beginning of the diffusion, the sharpest edges are removed, roughly corresponding to the higher frequencies. This is also visible in Figure 4.2. The clean ECG spectrum is more profound for lower diffusion time, whereas the CC-artifact is more dominant for high diffusion time. Despite the differences between these spectra, the overlap is still considerable, making it hard to filter with a transfer function as described by 4.25.

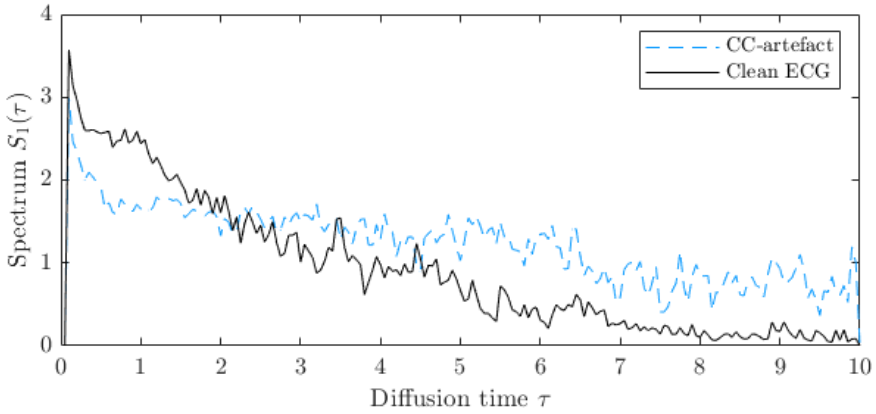

Figure 4.2. *Mean spectra $S_1(\tau)$ obtained with nonlinear spectral decomposition with the TV functional $J_{TV}(u)$. The mean spectra are calculated from 221 spectra each. For the CC-artifact spectra, 4-second ECG segments with an asystole and CCs were used. Clean ECG spectra were calculated with clean non-overlapping 4-second ECG-segments.*

Naturally, the spectral amplitude is merely a view of the spectral decomposition $\phi(t, \tau)$. There are more sophisticated ways of filtering than applying a transfer function that only depends on τ. Filtering can be generalized by defining a transfer function that also depends on the transform

$$x^H(t) := \int_0^\infty H(\phi(\tau, t), \tau, t)\ \mathrm{d}\tau. \tag{4.29}$$

Deciding for an optimal transfer function is a difficult task that requires a priori knowledge of the interaction of the clean ECG and the CC-artifact. In the next section we will discuss a data driven method for both the transform and the transfer function, that omits the need for assumptions about the transfer function.

4.4 Deep learning-based filtering

Deep learning offers the possibility to tailor a filter method based on a set of data. Deep learning is a specific type of machine learning based on artificial neural networks. Neural networks are a collection of artificial neurons which are connected. Each neuron contains a (nonlinear) function that takes several outputs from other neurons as input and produces one output. These artificial neurons are commonly ordered in layers. By correctly training a network, the variables of each neuron are trained such that the entire network learns a specific task. Neural networks can be used for a data driven filtering. Both the transform as well as the transfer function can be learned.

Autoencoders are a type of neural network for signal representation that learn to reproduce their input. They do so by transforming an input $x \in \mathbb{R}^L$ to a latent representation in $\mathbb{R}^P$ (encoding) and back to the

input space (decoding)

$$N_E : \mathbb{R}^L \to \mathbb{R}^P \tag{4.30}$$

$$N_D : \mathbb{R}^P \to \mathbb{R}^L. \tag{4.31}$$

The encoder N_E and decoder N_D are jointly trained by minimizing a certain loss function $L(N_D, N_E)$ over all N inputs. The loss function is the sum of a certain norm of the difference between the input and output of the network

$$L(N_D, N_E) = \sum_{n=1}^{N} \|x_n - N_D(N_E(x_n))\|^2. \tag{4.32}$$

When optimally trained the decoder approximates the inverse of the encoder. Autoencoders are traditionally used for dimensionality reduction or feature learning.

In the constricted case where the encoder and decoder consist of strictly linear layers and the loss function norm is the L^2 norm, the optimal solution is strongly related to the principal component analysis (PCA) [97]. PCA is a linear transformation that transforms a set of inputs into a new space where the first coordinate represents the principal component with the highest variance. The following principal components are all uncorrelated to each other and are ordered by decreasing variance. Similar to autoencoders, PCA is often used for dimensionality reduction by selecting only the first principal components, i.e. the principal components with the highest variance.

Baldi and Hornik [97] proved that the optimal solution of such an autoencoder is the orthogonal projection onto the space spanned by the first P eigenvectors of the autocorrelation matrix of the input vectors Σ. We will give a short sketch of this proof. In the case of linear layers the encoder and decoder can be seen as matrix multiplications with $N_E \in \mathbb{R}^{P\times L}$ and $N_D \in \mathbb{R}^{L\times P}$. The loss function then simplifies to

$$L(N_D, N_E) = \sum_{n=1}^{N} \|x_n - N_D N_E x_n\|^2. \tag{4.33}$$

For a fixed N_D, the loss function is convex in the coefficients of N_E, therefore the optimal solution is found for any N_E satisfying

$$N_D^T N_D N_E \Sigma = N_D \Sigma. \tag{4.34}$$

If the autocorrelation matrix Σ is invertible and N_D is of full rank P, then the solution is found for

$$N_E = (N_D^T N_D)^{-1} N_D^T. \tag{4.35}$$

For the optimal solution of the autoencoder we then have

$$A = N_D N_E = N_D (N_D^T N_D)^{-1} N_D^T = P_{N_D}, \tag{4.36}$$

where P_{N_D} is the projection onto the subspace spanned by the columns of N_D.

Similarly, for fixed N_E, the loss function is convex in the coefficients of N_D, and the optimal solution is found for any N_D satisfying

$$N_D N_E \Sigma N_E^T = \Sigma N_E^T. \tag{4.37}$$

Right side multiplication with N_D^T will give a constraint for matrix N_D via its the projection P_{N_D}

$$N_D N_E \Sigma N_E^T N_D^T = \Sigma N_E^T N_D^T \tag{4.38}$$

$$A \Sigma A^T = \Sigma A^T \tag{4.39}$$

$$P_{N_D} \Sigma P_{N_D}^T = \Sigma P_{N_D}^T. \tag{4.40}$$

The pair of N_E and N_D satisfying Equation 4.36 and 4.40 are the optimal solution for the minimization problem.

Assume that Σ has L distinct eigenvalues $\lambda_1 > \cdots > \lambda_N$. Let I denote a subsset of P eigenvalues, and $U_I \in \mathbb{R}^{L\times P}$ a matrix with the corresponding eigenvectors of Σ. Then N_E and N_D are the solution to a critical point (saddle point, local or global minimum) of L if and only if there exists an invertible matrix $C \in \mathbb{R}^{P\times P}$ such that

$$N_E = C^{-1}U_I^T \tag{4.41}$$
$$N_D = U_I C \tag{4.42}$$

At that critical point we have

$$A = P_{U_I} \tag{4.43}$$
$$L(N_E, N_D) = trace(\Sigma) - \sum_{i\in I} \lambda_i \tag{4.44}$$

This clearly shows that L is minimized when U_I contains the first P eigenvectors, with the largest eigenvalues and variation. Like PCA the autoencoder is a projection onto the subspace spanned by the first P principal components. However, in contrast to PCA, the basis signals found by the autoencoder are generally not orthogonal. The principle components can even be retrieved from the basis signals of the autoencoder by applying the singular value decomposition (SVD) [98].

A transform learned by an autoencoder combines the best of PCA and nonlinear spectral transforms. It inherits the property of PCA that the latent representation is learned to best describe the set of input signals. Nonlinear spectral transforms are limited in their representation by the eigenfunctions of the regularization functional $J(u)$. However, autoencoders do have the ability to create nonlinear transforms unlike PCA.

In the previous sections we described filtering by applying a transfer function H to the transform. The added benefit of using a neural network is that a transfer function can be learned instead of defined. This gives the freedom to define more sophisticated transfer function, that can also depend on the transform itself. A separation network can be described as a mapping from the latent representation of dimension P to a vector of twice the latent dimension $2P$

$$N_S : \mathbb{R}^P \to \mathbb{R}^{2P}. \tag{4.45}$$

The result of the separation network will be the approximation of the latent representation of the ECG $N_{S1}(y)$ and CC-artifact $N_{S2}(y)$ stacked above each other in one vector

$$N_S(y) = \begin{bmatrix} N_{S1}(y) \\ N_{S2}(y) \end{bmatrix}. \tag{4.46}$$

These two latent representations can be fed to the decoder separately to create two outputs that estimate the ECG and the CC-artifact

$$\hat{s_1} = N_D(N_{S1}(N_E(x))) \tag{4.47}$$
$$\hat{s_2} = N_D(N_{S2}(N_E(x))). \tag{4.48}$$

In the simplest case N_S will be a fully connected layer

$$N_S(y) = f(Wy + b), \quad W = \begin{bmatrix} W_1 \\ W_2 \end{bmatrix} \in \mathbb{R}^{2P\times P}, b \in \mathbb{R}^{2P}, \tag{4.49}$$

where f is some activation function. If f is the identity, b a zero vector and W_i are diagonal matrices, the separation network can be compared to the classical transfer function as used in Equation 4.2. Other choices for f, b and W will result in more complex transfer functions that will also depend on the transform itself. However, it is not capable of applying a time dependent transfer function since the latent representation does not include time. A similar problem arises in audio separation, where multiple instruments or voices are recorded at once and it is desirable to separate these audio recordings. In this

field recurrent neural networks (RNNs) are used to separate these audio signals in a latent representation [99–101].

Recurrent layers do not only depend on the current input y but also the previous hidden state. The hidden state h is an extra variable that depends on the past hidden states and inputs. A classical recurrent layer has the following update rules

$$h(t) = f_h(W_h y(t) + Uh(t-1) + b_h) \tag{4.50}$$
$$z(t) = f_z(W_z h(t) + b_z), \tag{4.51}$$

where f_h, f_z are activation functions and $z(t)$ is the current output of the recurrent layer. However, a latent representation found by an autoencoder does no longer depends on time, so how is it possible to apply a recurrent layer to the latent representation? A smart solution for this problem can also be found in audio separation. Instead of transforming the entire signal, the signal is first cut up into non-overlapping subsegments with each their own transform. A recurrent layer can then be applied to the series of transforms to create a time-dependent separation of the input signal.

4.5 Proposed filter

We propose a CC-artifact filter based on the audio separation network TasNet [101]. This network combines a nonlinear autoencoder with a RNN in the latent space for separation. An overview of the proposed architecture is given in Figure 4.3. The key property of this network is that an input signal $x(t)$ is cut up into K small subsegments of length L, where K varies based on the length of the input signal. In that way the time series is converted into a series of L-dimensional vectors. The encoder encodes each L-dimensional vector into the latent space of dimension P. A recurrent separator network uses the temporal relationship between the latent representations of each subsegment to return two estimates of latent representations of the clean ECG y_1 and the CC-artifact y_2. The decoder returns two sequences of L-dimensional vectors which can be pieced together to form an estimate of the clean ECG and an estimate of the CC-artifact.

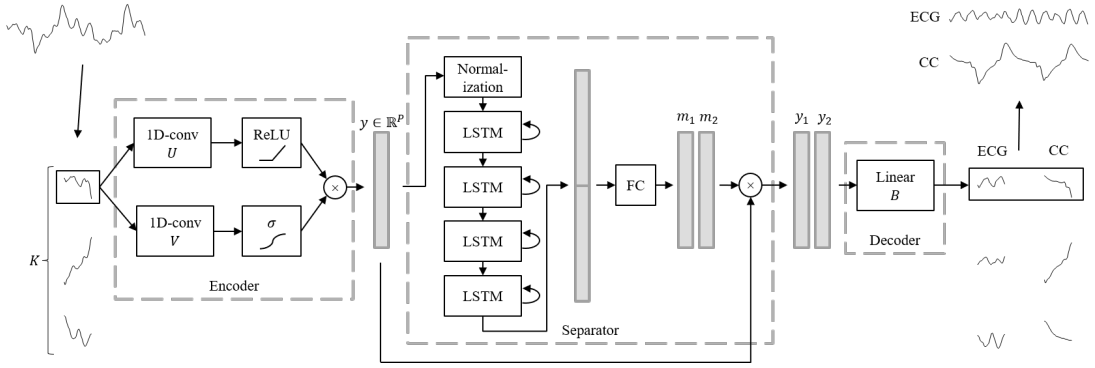

Figure 4.3. *Proposed architecture for a CC-artifact filter based on the audio separation network TasNet [101]. TasNet requires an input signal to be cut up into subsegments which create a series of vectors that are the input to the network. The encoder consists of two convolutional layers with different activation functions. The separator network applies a normalization layer and four long short-term memory (LSTM) layers before a fully connected (FC) layer to create two vectors m_1 and m_2. The element-wise product of y with these vectors is fed to the decoder which is a single linear layer.*

The autoencoder combines a nonlinear encoder N_E that generalizes the transform with a linear decoder

N_D defined by

$$N_E : \mathbb{R}^L \to \mathbb{R}^P \tag{4.52}$$
$$N_E(x) = ReLU(x * U) \odot \sigma(x * V) \tag{4.53}$$
$$N_D : \mathbb{R}^P \to \mathbb{R}^L \tag{4.54}$$
$$N_D(y) = By. \tag{4.55}$$

such that y is nonnegative and U and V are convolution operators. After training, the decoder is an approximation of the linear deconvolution [102] or inverse of the encoder. A linear decoder allows for easier interpretation of the learned transform. The columns of the matrix B represent the basis signals which relate to the eigenfunctions in nonlinear spectral analysis. Each input signal is transformed into a linear combination of these basis signals.

The encoder combines two activations ReLU and sigmoid (σ), called a gated convolutional layer. Gated convolutional neural networks optimize the benefits of linear activations and nonlinear activations [103]. The gradient of ReLU activations is 1 for nonnegative inputs, hence it lets gradients pass trough the active units unchanged. Therefore, using ReLU activations reduces the vanishing gradient problem. The sigmoid outputs can be viewed as gates that control the information passed on [103].

The choice of using convolutional layers for time series might seem like a counterintuitive choice. Convolutional layers are time-invariant, and therefore view a time series as an image, disregarding the temporal component of the time series. Moreover, convolutional layer operate locally rather than globally. However, convolutional neural networks have proven their use in ECG analysis [104–106]. Furthermore, by cutting a signal into subsegments of length L and separating with a recurrent network allows for temporal interpretation.

The separation network creates two vectors m_1 and m_2 with elements between 0 and 1. The output from the separation is given by element-wise multiplication with the latent representation

$$y_i = m_i \odot y. \tag{4.56}$$

The first layer of the separation network is a normalization layer [107] that creates scale invariant vectors. Normalization ensures more stable and efficient training of the following long short-term memory (LSTM) layers. Four causal (uni-directional) LSTM layers evaluate the temporal relationship of the latent representations of the subsegments. The number of units in the hidden state of the LSTM layers was set to $2P$. The LSTM layers are followed by a fully connected layer with a Softmax activation. This layer transforms the $2P$ vectors into two vectors m_i of length P. The Softmax activation ensures that all values of m_i are in $(0, 1)$.

Using this deep learning method for separation is similar to a transfer function that depends on the time-varying latent representation. Furthermore, this method does not assume the CC-artifact to be additive as existing methods do. It learns to represent the clean ECG and the CC-artifact by training and is therefore capable of learning different interactions. Furthermore, this technique can theoretically be applied in real-time, with only a small delay of the length of a subsegment.

The parameters in this architecture were trained by minimizing a loss function based on the SNR of the outputs. The SNR is a common choice in audio separation networks, since it not only compares the input to the output but also regularizes the output. The loss is defined as the negative mean SNR of both the ECG and CC-artifact estimate

$$\mathrm{SNR}_i := 10 \log_{10} \frac{\|s_i\|^2}{\|\hat{s}_i - s_i\|^2}. \tag{4.57}$$

Before calculation of the loss both the reference signals and estimates are normalized to have zero mean. During supervised training it is essential that the clean ECG and CC-artifact are known. The neural network is therefor trained with artificially combined input signals that are a summation of a clean ECG

s_1 and a CC-artifact s_2. The loss is then calculated by

$$Loss = -5 \log_{10} \left(\frac{\|s_1\|^2 \|s_2\|^2}{\|\hat{s}_1 - s_1\|^2 \|\hat{s}_2 - s_2\|^2} \right) \tag{4.58}$$

$$Loss = -5 \log_{10} \left(\frac{\|s_1\|^2 \|s_2\|^2}{\|N_D(N_{S1}(N_E(s_1 + s_2))) - s_1\|^2 \|N_D(N_{S2}(N_E(s_1 + s_2))) - s_2\|^2} \right). \tag{4.59}$$

$$\tag{4.60}$$

This limits the network to the unrealistic assumption that the CC-artifact is a additive artifact. However, it does provide a good starting point for the evaluation of this type of filtering. In further research the input signal during training can be made by a nonlinear combination that more closely match the actual interaction of the CC-artifact.

The network returns two signals. During training it optimizes the representation in basis signals as well as the weight vectors for each signal. As it creates these two weight vectors simultaneously, it is unknown which weight vector will correspond to which source signal. This problem is known as the label permutation problem [108]. In audio separation this problem is solved by permutation invariant training (PIT), as is also done with the TasNet [101]. However, in the case of ECG filtering we do care about permutation. It matters which output signal is the ECG signal estimate and which is the CC-artifact estimate. Because these signals are different in their appearance it is possible to use a convention that the first output signal will always represent the clean ECG signal [100]. Therefore, we will not use a PIT.

The minimization problem of the loss function was solved by the Adam algorithm [109]. Adam is an extension of the stochastic gradient decent that computes individual adaptive learning rates for different parameters. The adaptive learning rates are scaled by the step-size α. The initial step-size set to $\alpha = e^{-3}$ and halved when the loss of the validation set increased for three consecutive epochs. Training was stopped earlier if the loss of the validation set increased for ten consecutive epochs. The batch size was 125 and no further regularization was applied.

4.5.1 Training set

For the training dataset ECG and TTI data were used from an OHCA-cohort previously described by Thannhauser et al. [16]. This cohort includes non-traumatic OHCAs of adult patients with VF as the initial recorded rhythm. ECG and TTI data were simultaneously recorded with defibrillator paddles of defibrillators of the same manufacturer (ZOLL X Series R Monitor/ Defibrillator) with identical signal processing characteristics (e.g. built-in bandpass filters) for all subjects. ECG and TTI were recorded with a sampling frequency of 125 and 62.5 Hz respectively. TTI measurements were used to annotate CC-intervals. From these annotations, segments of 4 to 10 seconds were selected, prioritizing longer segments. Each selected segment had one cardiac rhythm and no onsets or offsets of CCs. Furthermore, all signals were adjusted to have zero mean.

For training, mixed segments were artificially composed, created by adding two measured signals: a clean ECG segment and a corrupted ECG segment measured during an asystole. The corrupted ECG segment with an asystole represents the CC-artifact. In the set of mixed signals, each clean ECG segment is used once with a randomly assigned to one of the 216 CC-artifact segments. This CC-artifact can be a manual or mechanical artifact. This data set was divided into a training and a validation set used in Section 5 in a ratio of 8:2. An overview of the training set is given in Table 4.1.

4.5.2 Hyperparameter optimization

The choices of the hyperparameters P and L greatly influence the transform as well as the separation. Therefore we applied a selective grid search to optimize these hyperparameters within a set range. The number of basis signals P also changes the training time. A large P will require more epochs to train.

Classical filters use windows in the range of 4.8 to 15 seconds. The result of a fast Fourier transform (FFT) would therefore be have a frequency resolution of 0.07 to 0.20Hz. The input ECG contains

Table 4.1. *Properties of the training dataset. The number of patients of which clean ECG segments are used and of which the CC-artifact is used during an asystole are also given. CC: chest compression, ECG: electrocardiogram, OR: organized rhythm, VF: ventricular fibrillation.*

	All	Asystole	OR	VF
nr of segments	5612	180	4217	1215
manual CC	1252	46	929	277
mechanical CC	4360	134	3288	938
mean length (s)	11.1	9.70	11.7	9.11
nr of patients (ECG)	144	53	130	138
nr of patients (CC)	54	43	52	54

frequencies of 0-30Hz, resulting into 192 to 450 meaningful distinct frequencies in the FFT result. That means these windows allow for decomposition into a Fourier series of 192 to 450 basis signals. A deep learning decomposition should probably have a similar amount of basis signals. The grid search was applied for

$$P \in \begin{bmatrix} 300 & 400 & 500 \end{bmatrix}. \tag{4.61}$$

A large P gives a better performance of the autoencoder on the training set. However, a small P creates a more generalizable network, since it is less adjusted to the training set.

The length of the sub-segments L in samples is also the length of the basis signals. Three different options were examined

$$L \in \begin{bmatrix} 31 & 68 & 93 \end{bmatrix}. \tag{4.62}$$

These values of L were chosen because they represent one period in samples, given a sampling frequency $f_s = 125Hz$, for respectively the upper bound of the dominant VF frequency (4Hz) [110], the optimal manual CC-rate ($1\frac{5}{6}$Hz), and the mechanical CC-rate ($1\frac{1}{3}$Hz). The final network should be able to change at least every compression to be adaptable enough.

The sets in Equations 4.61 and 4.62 result in nine different options for the selective grid search. Figure 4.4 shows the loss of the validation set for each epoch. The graph shows that the length of the basis signals L has a more profound effect on the validation loss than the number of basis signals P. Hyperparameter L has a great impact on the temporal flexibility of the network which is very important is this dynamic data set. Whereas P mostly influences the generalizability of the network, which seems a less notable issue in these data sets. The combination of $L = 31$ and $P = 400$ has the lowest validation loss.

4.5.3 Results of training

Figure 4.5 shows the loss of the training and validation set during training. The stopping criterion was reached at epoch 59. The learning rate was halved at each vertical line. The model is saved after epoch 27, where the validation loss was minimal. At this point the validation loss was -10.3 and the training loss -26.0.

During training the neural network created 400 different basis signals of 0.25s. An overview of all these signals is shown in Figure 4.6. The basis signals are ordered from most used to least used (top to bottom) based on the corresponding entries in vector y. This image shows that the most used signals are waves of one period. Some less used signals resemble a QRS complex. The least used signals tend to show high frequency, or noise-like signals. Using only the autoencoder function

$$A = N_D N_E \tag{4.63}$$

can show if these basis signals were adequate to model ECG signals during cardiac arrest. Ideally, the autoencoder should be the identity mapping $A = I$. If this is the case the output of the autoencoder will perfectly match any input with a zero mean squared error (MSE). MSE is a measure for the difference

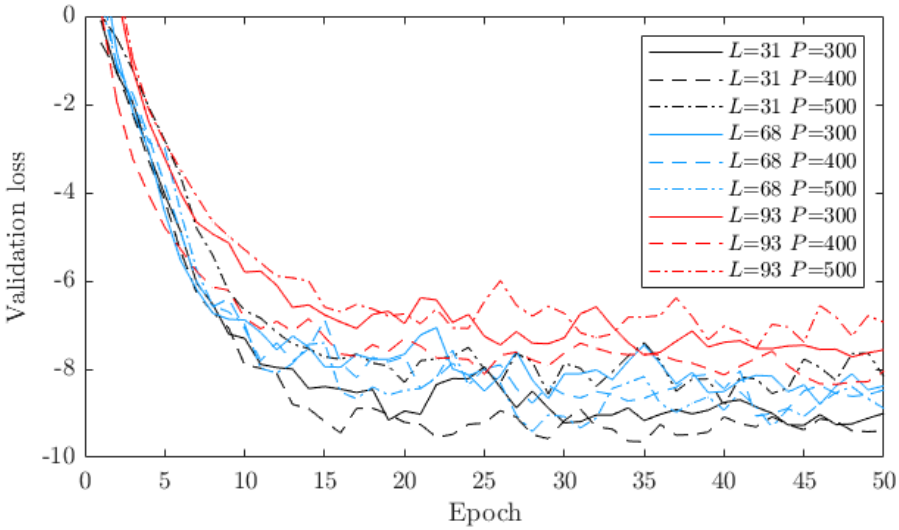

Figure 4.4. *Loss of the validation set for each combination in the grid search.*

between the input and output of the autoencoder

$$MSE := \frac{1}{n}\|A(x) - x\|^2, \tag{4.64}$$

where n denotes the length of the input signal in samples. The MSE for different sets is shown in Table 4.2, and is low for every set. This shows that the learned set of basis signals is generalizable to the validation set.

Table 4.2. *Results of the mean squared error (MSE) of the trained autoencoder for different sets.*

	Training	Validation
Mixed signals	$1.000 \cdot 10^{-3}$	$1.000 \cdot 10^{-3}$
Clean ECG	$5.408 \cdot 10^{-4}$	$5.273 \cdot 10^{-4}$

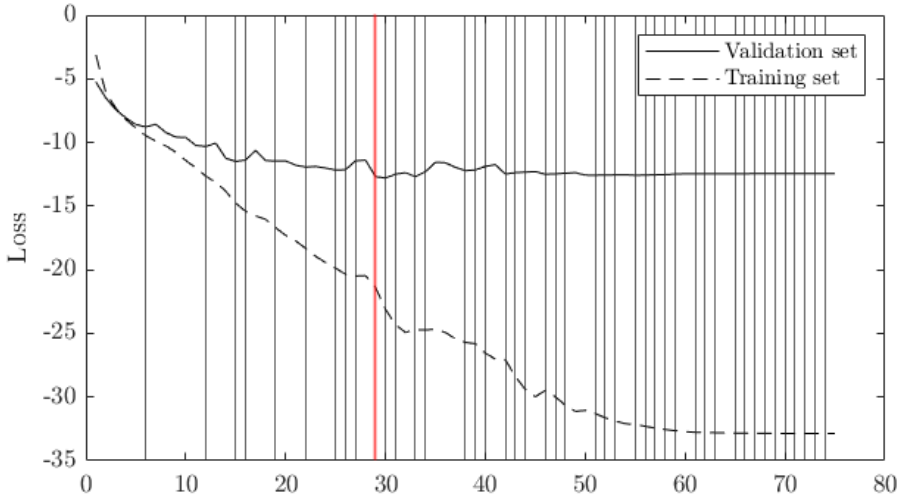

Figure 4.5. *Loss of training set and validation set during training. The black vertical lines indicated the epochs after which the step-size α was halved. The model is saved after epoch 27 (red vertical line) with a validation loss of -10.3 and a training loss of -26.0.*

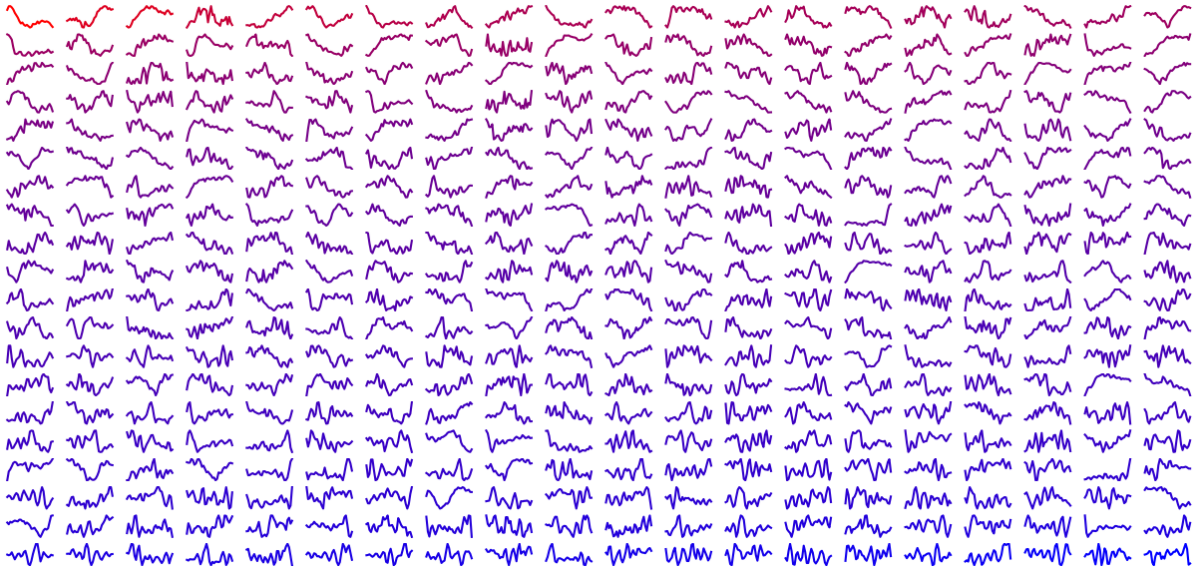

Figure 4.6. *Image of the 400 basis signals with a length of 0.25s (31 samples) ordered from most important (top, red) to least important (bottom, blue)*

CHAPTER 5

Validation of the deep learning-based filter

5.1 Introduction

In the previous chapter we introduced a neural network to remove the CC-artifact from cardiac arrest ECGs. This network uses only the ECG measurement with CC-artifact and does not require any reference signals to return an estimate of the ECG without any disturbances. In this chapter we asses the signal quality of the ECG estimate. Ideally, a clinically applicable filter should at least return a comparable, but ideally an improved signal quality relative to the existing filters.

The quality of an ECG signal can be measured in different ways. The most objective method is to compare the ECG estimate to a ground truth with a distance measure such as the widely used SNR. However, this is also an abstract method and requires a ground truth which is not always available. A more clinical approach is to evaluate if the ECG is suitable for a correct rhythm classification into shockable and nonshockable rhythms. Rhythm classification is one of the most important purposes of ECG measurements during cardiac arrest. In the case of VF, the ECG holds even more information about the patient and the optimal treatment. VF waveform measures, and especially the AMSA, have proven to be associated with shock success [16, 45], duration of cardiac arrest [46] and even the cause of cardiac arrest [46, 47]. In this chapter we will therefore validate the quality of the ECG estimate of the newly introduced deep learning (DL)-based filter in three stages: 1) SNR improvement, 2) rhythm classification, and 3) AMSA reconstruction.

5.2 Method

5.2.1 Cohort

For the current chapter ECG and TTI data were used from an OHCA-cohort previously described by Thannhauser et al. [16]. This cohort includes non-traumatic OHCAs of adult patients with VF as the initial recorded rhythm. Given the observational design, written informed consent was not necessary to obtain according to the Dutch Act on Medical Research involving Human Subjects. ECG and TTI data were recorded with defibrillator paddles of defibrillators of the same manufacturer (Lifepak12, Physio-Control, Redmond, USA) with identical built-in signal processing (e.g. bandpass filters) for all subjects. ECG and TTI data were recorded with a sampling frequency of 125 and 61 Hz respectively.

5.2.2 Data annotation

The cardiac rhythm was manually annotated in all ECG measurements as asystole, OR, VF. During CCs the rhythm can not be recognized accurately, therefore two different approaches were taken. If the cardiac rhythm before and after the CC interval was the same, it was assumed the cardiac rhythm during the CC remained the same as shown in Figure 5.1. If the cardiac rhythm was different after the CC interval the rhythm during CCs was annotated as unknown. Segments with pVT or where the rhythm was unknown were excluded.

The presence of CCs was manually annotated with the TTI measurements into CC intervals, intervals without CC and intervals where it was unknown if CCs were present. Segments where it was unknown if CCs were present were excluded. Furthermore, CC intervals were automatically categorized into manual CCs and mechanical CC administered by the Autopulse based on the dominant frequency of the TTI in the interval. If the dominant frequency was 80 ($\pm$5) per minute the interval was categorized as mechanical CC, otherwise it was categorized as manual CC.

From these annotations, non-overlapping segments of 4 to 10 seconds, prioritizing longer segments. Each selected segment had one cardiac rhythm and no onsets or offsets of CCs.

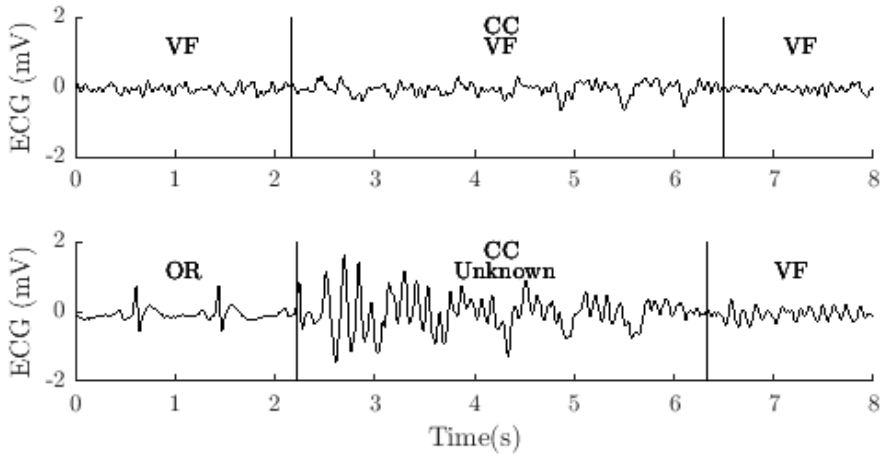

Figure 5.1. *Example of data annotation during a chest compression (CC) interval. The first examples shows ventricular fibrillation (VF) before and after a CC-interval, it is assumed that the cardiac rhythm during the CC-interval is also VF. In the second example, the rhythm before and after the CC-interval are different and therefore the cardiac rhythm during the CC-interval is unknown.*

5.2.3 Datasets

From the annotated measurements, three different datasets were defined:

- *Clean*: ECG segments without CCs
- *Mixed*: summation of a clean ECG segment with a CC-artifact. The added CC-artifact is a ECG segment with an asystole during CCs. Each clean ECG segment is used once with a randomly assigned manual or mechanical CC-artifact.
- *Corrupted*: ECG segments during CCs.

The mixed and clean dataset were identically separated with a ratio of 8:2 into a training set and a validation set, such that no clean ECG in the clean validation set is used in the mixed training set and vise versa. The entire corrupted dataset is used for validation.

5.2.4 Validation stages

Validation of the signal quality is done in three stages: 1) SNR improvement, 2) rhythm classification, and 3) AMSA reconstruction.

1) Signal-to-noise ratio improvement

In the first stage we compare the clean ECG estimate to the real clean ECG with the SNR defined by

$$\mathrm{SNR} := 10 \log_{10} \frac{\|s\|^2}{\|\hat{s} - s\|^2}, \tag{5.1}$$

where s denotes the clean ECG and $\hat{s}$ denotes the estimated clean ECG. The input SNR is calculated with s representing the clean ECG and $\hat{s}$ the corresponding mixed signal. The SNR improvement is then defined as the increase in SNR compared to the input SNR.

2) Rhythm classification

The first validation stage is an abstract approach of validating a CC-artifact filter method because it is based on artificially combined signals. The second validation stage uses the mixed and corrupted validation dataset and evaluates the performance on the important clinical application of rhythm classification into shockable and nonshockable rhythms. Rhythm classification was done on 4-second ECG segments with an asystole detector described by Irusta [88] followed by a SAA described by Figuera et al [111].

The asystole detector is based on the power of band passed filtered (2.5 - 30 Hz) sub-segments of 1.6 second. In contrast to the original asystole detection algorithm, the input ECG is separated in to overlapping sub-segments x_i. The power is calculated for each sub-segment of length L following the equation

$$Power_i = 10^3 \frac{1}{L} \sum x_i^2(n). \tag{5.2}$$

A 4-second segment is classified as an asystole if the minimal power of all sub-segments is below a threshold Th_{Power}. The threshold Th_{Power} is set to 0.95 such that no shockable rhythms in the clean training dataset were classified as asystole. However, a bradycardia might be classified as an asystole, this will not pose any clinical problem since both rhythms are classified as non-shockable.

The SAA was a boosted trees model using six features including temporal features that characterize amplitude or slope, spectral features that relate to power content in different frequency bands, time-frequency features such as wavelet-based features and complexity features. The six features were selected from 30 features by Figuera et al using a L_1 regularized logistic regression with OHCA data. The code for this SAA was made available on GitHub [112]. Before validation, the SAA was trained on our clean training dataset.

First, a baseline performance of classification is defined by using the clean validation set. The performance is defined by the accuracy, sensitivity (ability to recognize shockable rhythms), and specificity (ability to recognize non-shockable rhythms). The distribution of the performance metrics was assumed to be Gaussian. Therefore, a 95% confidence interval was calculated by $1.96\sqrt{p(100-p)/n}$, where p denotes the performance metric and n the sample size.

3) AMSA reconstruction

In the last validation stage we evaluated the ability to calculate a reliable AMSA of filtered signals from the mixed validation set. For each VF segment, the AMSA was calculated on non-overlapping 3-second subsegments of $L = 375$ samples and then averaged. Before calculation, the ECG was zero-phase filtered with a fourth-order Butterworth band-pass filter of 2-48Hz. The FFT A of the filtered ECG was used to calculate the AMSA

$$AMSA = \frac{2}{L} \sum_{i=13}^{145} A_i \cdot f_i, \tag{5.3}$$

where f is the corresponding frequency domain. Only elements where $i \in (13, 145)$ were taken into the summation which correspond to an interval of $(f_{13}, f_{145}) = (4, 48)$Hz. Furthermore, the difference between the AMSA of the ECG estimate and the clean ECG was calculated as ΔAMSA.

5.2.5 Filter comparison

We compared the signal quality after the DL filter proposed in Section 4.5 to the signal quality after an existing linear Wiener filter on 1) SNR improvement, 2) rhythm classification, and 3) AMSA reconstruction. A short explanation of the DL filter is given in Appendix B. The Wiener filter was build in Matlab based on the article of Aramendi et al [12]. This Wiener filter uses a Fourier series with a time-dependent CC-rate as the fundamental frequency as described in Equation 3.2 as the reference signal. The time dependent CC-rate is based on the concurrent TTI measurements.

The SNR improvement of both filters was compared with a one-sided Wilcoxon signed-rank test suitable for paired non-normally distributed data to test for superiority of the DL filter over the linear Wiener

filter. The metrics of rhythm classification were assumed to be significantly different when the 95% confidence intervals did not overlap. AMSA of the ECG estimates of both filters were compared to the AMSA of the clean ECG using a two-sided Wilcoxon signed-rank test, suitable for paired non-normally distributed data.

5.3 Results

A total of 144 patients were included in the cohort with a mean age of 63 (±14) year. The clean and mixed validation set consists of 1403 ECG segments of 139 patients. In 52 patients a total of 221 segments with asystole during CCs were found that were used as CC-artifacts in the mixed validation set. Table 5.1a shows that most segments had an organized rhythm and most segments were paired with a mechanical CC-artifact. The larger corrupted dataset consists of 4699 segments with a mean length of 31.3 seconds from all patients in the cohort. Table 5.1b shows that most segments have VF (2937) as the cardiac rhythm and are corrupted by mechanical CCs. Several examples of filtering results of the mixed validation set using both the Wiener filter and the DL-based filter are described in Appendix C.

Table 5.1. *Properties of the clean and mixed (a) and corrupted (b) validation dataset. The mixed and clean validation set are created with the same set of clean ECG signals. The number of segments are reported as n (%). The number of patients of which clean ECG segments are used and of which the CC-artifact is used during an asystole are described. CC: chest compression, ECG: electrocardiogram, AS: asystole, OR: organized rhythm, VF: ventricular fibrillation.*

(a) *Clean and mixed validation dataset*

	All	AS	OR	VF
nr of segments	1403	47 (3.3)	1034 (73.7)	322 (23.0)
manual CC	304 (21.7)	9 (0.6)	223 (15.9)	72 (5.1)
mechanical CC	1099 (78.3)	38 (2.7)	811 (57.8)	250 (17.8)
mean length (s)	11.1	10.4	11.7	9.16
nr of patients (ECG)	139	28	113	98
nr of patients (CC)	52	27	48	51

(b) *Corrupted validation dataset*

	All	AS	OR	VF
nr of segments	4699	256 (5.4)	1506 (32.0)	2937 (62.5)
manual CC	1801 (38.3)	64 (1.4)	469 (10.0)	1268 (27.0)
mechanical CC	2898 (61.7)	192 (4.1)	1037 (22.1)	1669 (35.6)
mean length (s)	31.3	27.2	37.3	28.6
nr of patients	144	57	124	142

5.3.1 Signal-to-noise ratio improvement

In the first validation stage 1403 ECG estimates were compared to the target ECGs from the mixed validation set using the SNR. Table 5.2 shows the median with interquartile ranges in brackets for the mixed validation set without filter, after the Wiener filter, and after the DL-based filter. The input SNR had a median of 1.41 (-7.05 - 4.18). The Wiener filter improved the SNR with a median 2.72 (-0.45 - 6.61). The DL-based filter increased the SNR significantly ($p < 0.001$) more with a median increase of SNR of 6.91 (3.31 - 10.79).

The SNR improvement was not the same for each cardiac rhythm, as shown in figure 5.2. Both filters were able to improve the signal quality of nearly all asystole segments. However, the median SNR improvement was lower for segments with OR and VF, the SNR even decreased for part of these segments.

Table 5.2. *Results of the first validation stage. In the column 'no filter' the signal-to-noise ratio (SNR) is calculated by comparing the clean ECG with the mixed ECG. For the two filters, the SNR is calculated by comparing the clean ECG and the estimate ECG. The SNR improvement (ΔSNR) is the difference of SNR after filtering compared to the input SNR. All values are described by the median and interquartile range in brackets. The last column shows the p value for a superiority test of the DL filter over the Wiener filter with a one-sided Wilcoxon signed rank test.*

	No filter	Wiener filter	DL filter	Wiener vs DL
SNR	-1.41 (-7.05 - 4.18)	2.46 (-0.75 - 4.30)	5.42 (2.78 - 8.46)	<0.001
ΔSNR		2.72 (-0.45 - 6.61)	6.91 (3.31 - 10.79)	<0.001

The DL-based filter improved the median SNR more than the Wiener filter for all cardiac rhythms and the SNR increased for more segments. There is also a difference between manual and mechanical CC. Figure 5.2 shows that SNR increased more for mechanical CCs for both filters. The DL-based filter improved the median SNR more than the Wiener filter for both CC-types and the SNR increased for more segments.

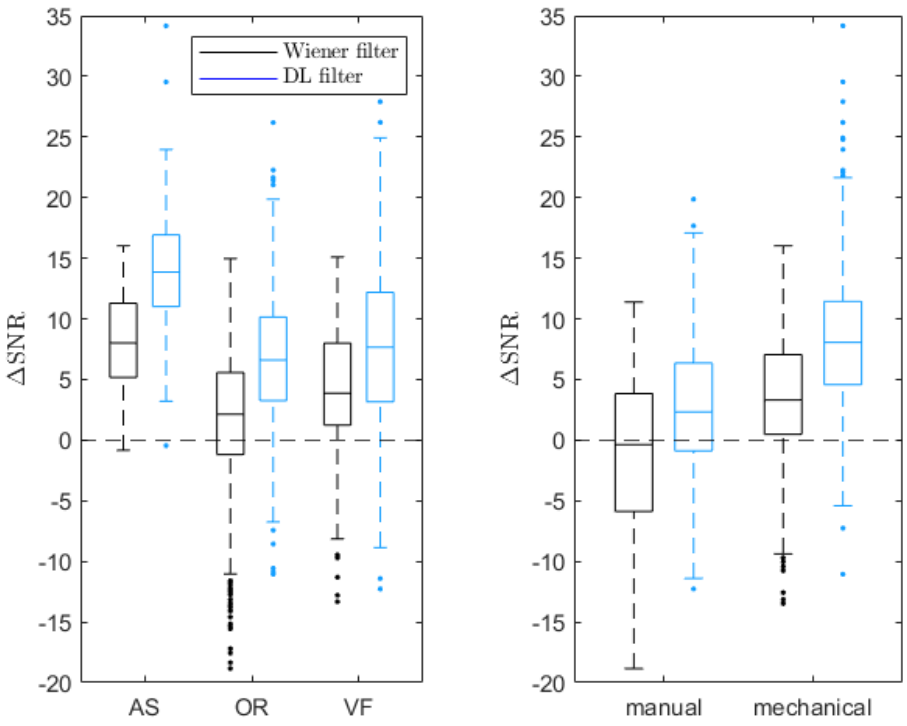

Figure 5.2. *The signal-to-noise ratio (SNR) improvement for (a) different cardiac rhythms and (b) different different CC-types after Wiener and DL-based filtering.*

5.3.2 Rhythm classification

The baseline accuracy, sensitivity (recognition of shockable rhythms), and specificity (recognition of non-shockable rhythms) of the rhythm classification on the clean validation set were 95.51%, 83.30%, and 98.38% respectively. The results in Table 5.3 show that the accuracy of the classification decreased significantly for the mixed set to 81.76% and for the corrupted set to 71.47%. After applying the Wiener

filter to the mixed dataset, the accuracy did not change significantly. However, the sensitivity increased and the specificity decreased. The opposite was seen after the DL-based filter, where the accuracy did decrease significantly, but the sensitivity and specificity did not change significantly. On the corrupted dataset both the Wiener filter and DL-based filter did not change the accuracy significantly. However, the sensitivity and specificity did change, where the sensitivity increased after Wiener filtering and the specificity increased after DL-based filtering.

Table 5.3. *Results of the second validation stage. This table shows the sensitivity, specificity and accuracy of shock advise of different datasets after no filter, a Wiener filter or a DL based filter. The clean dataset provides a baseline performance of the shock advise algorithm. All values are described by the mean and standard deviation in brackets.*

		No filter	Wiener filter	DL filter
Clean	accuracy	95.54 (94.46 - 96.62)		
	sensitivity	82.30 (80.30 - 84.30)		
	specificity	98.38 (97.72 - 99.04)		
Mixed	accuracy	81.76 (79.74 - 83.78)	77.98 (75.81 - 80.15)	71.47 (69.11 - 73.83)
	sensitivity	68.02 (65.58 - 70.46)	79.45 (77.34 - 81.56)	65.36 (62.87 - 67.85)
	specificity	84.71 (82.83 - 86.59)	77.69 (75.51 - 79.87)	79.48 (77.37 - 81.59)
Corrupted	accuracy	71.47 (70.18 - 72.76)	73.91 (72.65 - 75.17)	70.82 (69.52 - 72.12)
	sensitivity	65.37 (64.01 - 66.73)	74.18 (72.93 - 75.43)	53.89 (52.46 - 55.32)
	specificity	79.48 (78.33 - 80.63)	73.57 (72.31 - 74.83)	92.64 (91.89 - 93.39)

5.3.3 AMSA reconstruction

A total of 322 VF segments of the mixed dataset with a mean length of 9.16 seconds and an input SNR of -1.41 (-7.05 - 4.18) were analyzed in the last validation stage. The AMSA of the clean VF segments had a median of 7.50 (5.03-11.35), artificially adding a CC-artifact significantly increased the AMSA in nearly all cases (99%) with a median of 4.07 (2.14-6.79) as shown in Table 5.4. After filtering, the AMSA was significantly different from the AMSA of the clean segments for both the Wiener as the DL filter. However, differences were observed between the AMSA error after the Wiener filter 3.11 (1.19 - 5.86) and after the DL filter -0.65 (-1.82 - 0.76). Moreover, Table 5.4 also shows that mechanical CCs cause a larger error in the AMSA than manual CCs. After both filters ΔAMSA is higher for mechanical CCs compared to manual CCs.

Table 5.4. *Results of the third validation stage. All values are described by the median and interquartile range in brackets. Amplitude spectrum area (AMSA) in given in mVHz, ΔAMSA describes the error of AMSA compared to ground truth (clean ECG). The p value is the result of a two-sided Wilcoxon signed rank test comparing the AMSA calculated on the clean ECG with the AMSA of the corresponding column.*

	Clean ECG	No filter	Wiener filter	DL filter
AMSA	7.50 (5.03 - 11.35)	12.68 (9.48 - 17.73)	11.73 (8.55 - 17.64)	7.24 (4.61 - 11.48)
p-value		<0.001	<0.001	<0.001
ΔAMSA		4.07 (2.14 - 6.79)	3.11 (1.19 - 5.86)	-0.65 (-1.82 - 0.76)
manual		0.73 (0.33 - 1.60)	0.46 (0.15 - 1.14)	-1.03 (-1.89 - -0.34)
mechanical		4.70 (3.30 - 8.36)	3.89 (2.33 - 7.33)	-0.43 (-1.59 - 1.08)

The input ΔAMSA is correlated to the input SNR ($R = -0.53$) as shown in Figure 5.3, the ΔAMSA is greater when the input SNR is low. After applying the Wiener filter, this negative correlation remains largely unchanged ($R = -0.48$). However, after applying the DL based filter, the correlation largely disappears ($R = -0.14$) and ΔAMSA is more homogeneously distributed for all values of the input SNR.

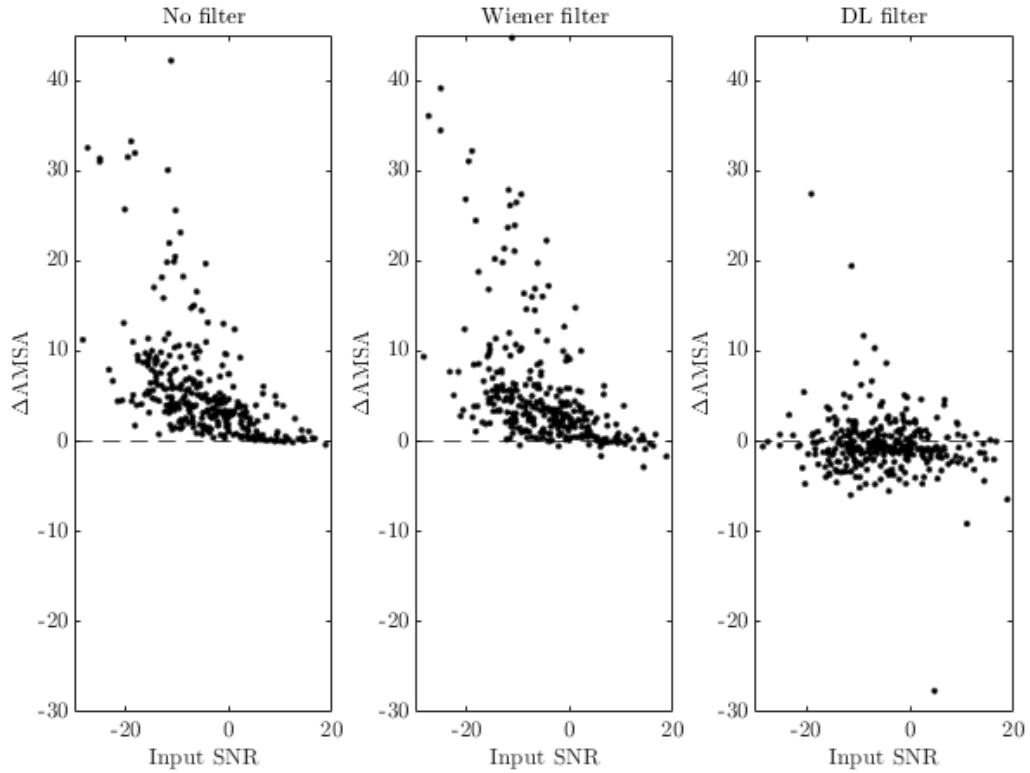

Figure 5.3. *Error in amplitude spectrum area (AMSA) after no filter, a Wiener filter and after a DL based filter with respect to input signal-to-noise ratio (SNR). The correlation coefficient was* $R = -0.53$ *after no filter,* $R = -0.48$ *after Wiener filter and* $R = -0.14$ *after DL-based filter.*

5.4 Discussion

The DL filter introduced in Section 4.5 was validated with three different methods and compared to a linear Wiener filter. These validation steps showed a significant improvement of the distance measures comparing the ECG estimate and the real ECG. The VF waveform measure AMSA could also be calculated from the ECG estimate with a median error of -0.65.

Published CC-artifact filters reported a SNR improvement between 3.3 and 9.0 on different datasets with an input SNR=0 as shown in Table 3.1. The highest improvements were seen with studies using only mechanical CC-artifacts. The median SNR improvement of the Wiener filter on our cohort of 2.72 is below the published range. A possible explanation can be found in the lower sampling frequency of 125Hz and 61Hz for ECG and TTI measurements respectively compared to 250Hz used by Aramendi et al [12]. The Wiener filter is highly dependent on the CC recognition in the TTI signal, therefore, a lower sampling frequency could decrease its performance. Despite the lower sampling frequency, we do see a SNR improvement for the DL-based that is comparable to published methods.

There are differences in performance for both filters regarding different cardiac rhythms and CC-artifacts. Both filters perform best on segments with asystole, where there is no interaction between the CC-artifact and the cardiac rhythm. Regarding CC-artifacts, both filters are better in reducing mechanical artifacts. These artifacts are more regular in frequency and morphology making it easier to remove by the Wiener filter. Mechanical CCs were also more represented in the training set of the DL-based filter, making the network better equipped to handle these artifacts.

The AHA has set recommendations for the evaluation and performance of SAAs in AEDs. Sensitivity for shockable rhythms should be no lower than 90% and specificity for non-shockable rhythms should

exceed 95% [59]. The baseline performance of the SAA on the clean validation set does not meet the required sensitivity of 90%, which can be caused by several factors. First, most AED algorithms are tested on holter recordings which are typically different from cardiac arrest ECG measurements [111]. During cardiac arrest, VF is usually older, and therefore of lower amplitude and lower frequency. Non-shockable rhythms are more often PEA which is commonly bradyarrhythmic with aberrant QRS complexes. The SAA used in this validation step was also tested on OHCA data by Figuera et al. However, the baseline sensitivity is well below their reported sensitivity range (90-99%). This can be caused by the lower sampling frequency of 125Hz of our cohort with respect to 250Hz where the SAA was designed for. Although the ECG segments were resampled from 125Hz to 250Hz, this might have caused a difference in the performance. Moreover, the SAA was designed with an older version of Matlab, since then the discrete wavelet function is updated making certain wavelets unavailable. This resulted in a difference of one of the features where the SAA is highly sensitive to.

For the mixed and corrupted validation set, the accuracy decreased as expected since the SAA was not designed to handle distorted ECG recordings. Surprisingly, the accuracy did not increase after either filter on both sets, even though sensitivity and specificity surpassed the AHA recommendations after Wiener filtering in the original article [12]. This can be due to the Wiener filter acting differently on this dataset as was also the case for the SNR. However, it is also likely that the result depends on the classification algorithm which is not robust and sensitive to small changes in the features. The DL-based filter increased the SNR considerably on the mixed validation dataset. Therefore, it is expected that the accuracy of the mixed dataset would increase, however, the accuracy of shock advice decreased. This shows that there is no correlation between SNR and rhythm classification, which suggests that this type of rhythm classification is not suitable for analyzing the signal quality.

For future implementation, it is possible to integrate the SAA in the network. The latent representation of the ECG estimate can be used as the input of a classification network. This network can also be trained with small added perturbations that would not influence the shock advice from a cardiologist, to create an even more robust SAA.

For mixed signals, the error in AMSA decreased more after the DL-based filter in comparison to the Wiener filter. However, the AMSA is still significantly different from the target AMSA with a median bias of -0.65. An error of 0.65 is comparable with an added noisy signal in the range of 0-0.01mV which does not change the visual interpretation. Lo et al [60] did a similar analysis with a Wiener filter using empirical modes of the ECG as a reference signal. They found a mean bias of AMSA from -0.19 to 3.33 depending on the input SNR from 0 to -9. Unfortunately, the definition of AMSA is not universal and differences in the definition lead to different values that are incomparable between studies. Lo et al used a smaller frequency range from 0.7-30Hz leading to overall lower AMSA values. However, we do see that the AMSA did not depend on the input SNR after the DL filter in contrast to the filter of Lo et al.

5.5 Conclusion

The purpose of this chapter was to validate the nonlinear CC-artifact filter introduced in Section 4.5 based on a neural network and compare it to an existing linear Wiener filter. The SNR improved significantly after applying the new filter to artificially mixed ECG signals compared to the Wiener filter. Shock advice based on a boosted trees model with six features was not robust enough to show the signal quality improvement after filtering with both the linear Wiener filter and the nonlinear DL-based filter. A manual classification into shockable and non-shockable will give a more fair interpretation of signal quality improvement of corrupted ECG signals after filtering. In a clinical application, shock advice can be optimally integrated with the new DL-based filter. The AMSA can be calculated more accurately after applying the new filter to mixed ECG, but a small bias remains.

To conclude, the nonlinear CC-artifact filter introduced in Section 4.5 based on a neural network significantly improved the signal quality of artificially mixed ECG signals, but it remains unclear what the signal quality improvement is of filtered corrupted ECG signals.

CHAPTER 6

The ventricular fibrillation waveform in relation to shock success on clean and filtered ECGs

6.1 Introduction

Ventricular fibrillation (VF) is the first observed rhythm in one out of four OHCAs [113, 114]. VF is a ventricular arrhythmia with uncoordinated chaotic movement of the ventricles that are ineffective and fail to produce cardiac output. Treatment of VF relies on defibrillation to terminate the VF and allow the start of an organized rhythm from the sinus node. Unfortunately, a defibrillator shock is not always successful in returning organized rhythm and multiple shocks are often required [115].

Over the years, VF waveform characteristics and especially AMSA have become a topic of interest. AMSA combines information of the frequency and amplitude [54] and is associated with ROSC, particularly in early shocks [16, 48, 53]. A current international randomized trial studies real-time AMSA analysis for guiding defibrillation timing [55]. The AMSA is calculated during CC pauses on clean ECG. In a recent study, Coult et al investigated the predictive property of AMSA during CCs for survival and ROSC and found a weaker, but still present predictive property [61]. However, they used a separate model for clean and corrupted ECG. The question remains if AMSA can predict shock success with one cut-off value with and without CCs.

The deep learning filter introduced in Section 4.5 has proven to return an ECG estimate from artificially mixed signals where the AMSA can be calculated with a small error. If this filter would be capable to do the same on corrupted ECG, analysis of AMSA would be possible for each ECG segment regardless of the presence of CC-artifacts. In this chapter we aim to research if the predictive property and cut-off value of AMSA to shock success remains unchanged for filtered ECG measurements.

6.2 Method

6.2.1 Cohort

For the current chapter ECG and TTI data were used from the same OHCA-cohort as the previous chapter, previously described by Thannhauser et al. [16]. This cohort includes non-traumatic OHCAs of adult patients with VF as the initial recorded rhythm. Given the observational design, written informed consent was not necessary to obtain according to the Dutch Act on Medical Research involving Human Subjects. ECG and TTI data were recorded with defibrillator paddles of defibrillators of the same manufacturer (Lifepak12, PhysioControl, Redmond, USA) with identical built-in signal processing (e.g. bandpass filters) for all subjects. ECG and TTI data were recorded with a sampling frequency of 125 and 61 Hz respectively.

6.2.2 Data annotation

The cardiac rhythm was manually annotated in all ECG measurements as asystole, OR, or VF. During CCs the rhythm can not be recognized accurately, therefore two different approaches were taken. If the cardiac rhythm before and after the CC interval was the same, it was assumed the cardiac rhythm during the CC remained the same as shown in Figure 5.1. If the cardiac rhythm was different after the CC interval the rhythm during CCs was annotated as unknown.

The presence of CCs was manually annotated using the TTI measurements into CC intervals, intervals without CC and intervals where it was unknown in CCs were present. Segments where it was unknown in CCs were present were excluded.

6.2.3 Per shock analysis

For each shock two pre-shock VF segments of 3 seconds were searched: the closest VF segment without CCs (clean) and the closest VF segment with CCs (corrupted). A shock was excluded if neither or only one of these segments was available in the 30 seconds before the shock or the shock was the 9th or more given. All pre-shock VF segments with CCs were filtered using the DL based filter described in Section 4.5. A short and easy explanation of the DL filter is given in Appendix B. This leads to three different sets: clean VF, corrupted unfiltered VF, and corrupted filtered VF.

All segments were zero-phase filtered with a fourth-order Butterworth band-pass filter of 2-48Hz. The FFT A of a filtered ECG was used to calculate the AMSA

$$AMSA = \frac{2}{L} \sum_{i=13}^{145} A_i \cdot f_i, \tag{6.1}$$

where f is the corresponding frequency domain and L the length of the segments in samples. Only elements where $i \in (13, 145)$ were taken into the summation which correspond to an interval of $(f_{13}, f_{145}) = (4, 48)$Hz.

6.2.4 Endpoint

The main goal was to examine the predictive property of AMSA on shock success before and after filtering. In absence of a measurement of the circulation, shock success was defined as return of organized rhythm (ROOR), i.e. at least 2 QRS-complexes within 5s, within 60s after shock delivery [116]. The AMSA of pre-shock VF before successful and unsuccessful shocks were compared with a two-sided Wilcoxon signed-rank test for clean, corrupted unfiltered, and corrupted filtered segments. The same comparison was done for early shocks (1-3) and late shocks (4-8).

Using the early shocks, a receiver operating characteristic (ROC) curve was made for AMSA calculated on clean, corrupted unfiltered, and corrupted filter pre-shock VF segments. The distribution of the area under the curve (AUC) was assumed to be Gaussian. Therefore, a 95% confidence interval was calculated by $1.96\sqrt{AUC(1-AUC)/n}$, where n denotes the sample size. The AUC was assumed to be significantly different when the 95% confidence intervals did not overlap. Moreover, for clean, corrupted unfiltered, and corrupted filtered segments a cut-off value was calculated when the sensitivity and specificity were equal as was done by Ristagno et al [53].

6.3 Results

In total, 377 shocks were analyzed of 139 OHCA-patients with VF as the first observed rhythm. Baseline characteristics of the study population are reported in Table 6.1. The mean age was 64 ± 14 and 71% was male. Baseline characteristics of the included shocks and pre-shock segments are reported in Table 6.1a and 6.1b. Of the 377 analyzed shocks, 46.7% (176/373) was successful. A total of 237 shocks were early shocks (1^{th}-3^{rd} shock), of which 44.3% (105/233) was successful compared to 140 late shocks (3^{rd}-8^{th} shock), of which 50.7% (71/140) was successful. The time from the end of the pre-shock VF to the shock was significantly shorter for the clean VF segments 0.14s (0.06-10.21) compared to corrupted VF segments 4.31s (0.06-12.60), p=0.024. The AMSA was significantly higher for corrupted VF segments 14.83 (10.31-22.56) compared to clean VF segments 8.56 (5.91-12.57). After filtering the AMSA decreased with a median of -3.45 (-6.82 - -1.98) to 10.91 (7.15 - 16.43).

For clean VF, AMSA was significantly higher before successful shocks 9.55mVHz (6.84-13.69) compared to unsuccessful shocks 7.57mVHz (5.30-11.09), p<0.001 (Table 6.3). The AMSA also differed significantly for early shocks (p<0.001), but did not differ significantly for late shocks (p=0.893). For corrupted unfiltered VF, AMSA did not differ between successful and unsuccessful shock for all shocks (p=0.092) and late shocks (p=0.087). However, AMSA was significantly higher before successful shocks 15.40mVHz (11.80-33.37) compared to unsuccessful shocks 13.95mVHz (9.36-22.68), p=0.001. After filtering, AMSA

was significantly higher before successful shocks 11.99mVHz (8.55-16.46) compared to unsuccessful shocks 9.85mVHz (5.86-16.37), p=0.014. The AMSA also differed significantly for early shocks (p<0.001), but did not differ significantly for late shocks (p=0.259).

Figure 6.1 shows the ROC curves of the prediction of AMSA for shock success of clean, corrupted unfiltered, and corrupted filtered pre-shock VF. The AUC for clean VF was 0.68 (0.62-0.74). The AUC was significantly lower for corrupted unfiltered 0.52 (0.46-0.59) and corrupted filtered 0.55 (0.49-0.62). The asterisks indicate the points where sensitivity and specificity were equal. At this point, clean pre-shock VF had a cut-off value of 9.30mVHz at a sensitivity and specificity of 59.9%. Cut-off values were higher for corrupted VF, with 16.5mVHz at sensitivity and specificity of 51.4% for unfiltered VF and 12.21mVHz with a sensitivity and specificity of 53.4% for filtered VF.

Table 6.1. *Baseline characteristics of study cohort. Categorical data were reported as numbers (percentages). Continuous variables were reported as mean ± stardard deviation for normal distributed variable and as median (interquartile range) otherwise. EMS: emergency medical services, ROSC: return of spontaneous circulation.*

Patient characteristics	
Age (years)	64 ± 13
Male gender	89 (71)
Arrest characteristics	
Public location arrest	49 (40)
Witnessed arrest	86 (75)
Response time (minutes)	8 (5-10)
Number of EMS shocks	4 (2-7)
Amiodarone	58 (57)
Adrenaline	88 (85)
Outcome characteristics	
Any ROSC during resuscitation	72 (59)
Sustained ROSC	54 (44)
Survival to discharge	28 (23)

Table 6.2. *Baseline characteristics of (a) shocks and (b) pre-shock VF segments. Categorical data were reported as numbers (percentages). Continuous variables were reported as medians (interquartile ranges). Amplitude spectrum area (AMSA) is given in mVHz and time to shock in seconds. CC: chest compression, VF: ventricular fibrillation*

(a) *Shock characteristics*

	Total	Early (1-3)	Late (4-8)	p
Nr of shocks	377	237 (62.9)	140 (37.1)	
Shock nr	3 (1-4)	2 (1-2)	5 (4-6)	<0.001
Successful	176 (46.7)	105 (44.3)	71 (50.7)	0.241

(b) *Pre-shock VF characteristics*

	Clean	Corrupted	p
Time to shock	0.14 (0.06-10.21)	4.31 (0.06-12.60)	0.024
AMSA	8.56 (5.91-12.57)	14.83 (10.31-22.56)	<0.001
Manual CC		140 (37.1)	

Table 6.3. *The amplitude spectrum area (AMSA) in relation to shock success (return of organized rhythm) for all shocks (377), 1^{th}-3^{rd} shocks (237), and 4^{th}-8^{th} shocks (140).*

(a) *Clean VF*

	Shock success	No shock success	p
AMSA (all shocks)	9.55 (6.84-13.69)	7.57 (5.30-11.09)	<0.001
AMSA (shock 1-3)	10.52 (7.41-14.85)	7.91 (5.51-11.24)	<0.001
AMSA (shock 4-8)	8.71 (6.07-11.76)	8.53 (5.88-12.59)	0.893

(b) *Corrupted unfiltered VF*

	Shock success	No shock success	p
AMSA (all shocks)	15.40 (11.80-22.37)	13.95 (9.36-22.68)	0.092
AMSA (shock 1-3)	17.14 (13.02-24.26)	13.99 (10.28-49.76)	0.001
AMSA (shock 4-8)	14.30 (9.68-17.66)	15.06 (10.62-23.47)	0.087

(c) *Corrupted filtered VF*

	Shock success	No shock success	p
AMSA (all shocks)	11.99 (8.55-16.46)	9.85 (5.86-16.37)	0.014
AMSA (shock 1-3)	12.39 (9.26-18.92)	10.00 (6.68-15.25)	<0.001
AMSA (shock 4-8)	10.35 (7.28-13.69)	11.15 (7.12-17.09)	0.259

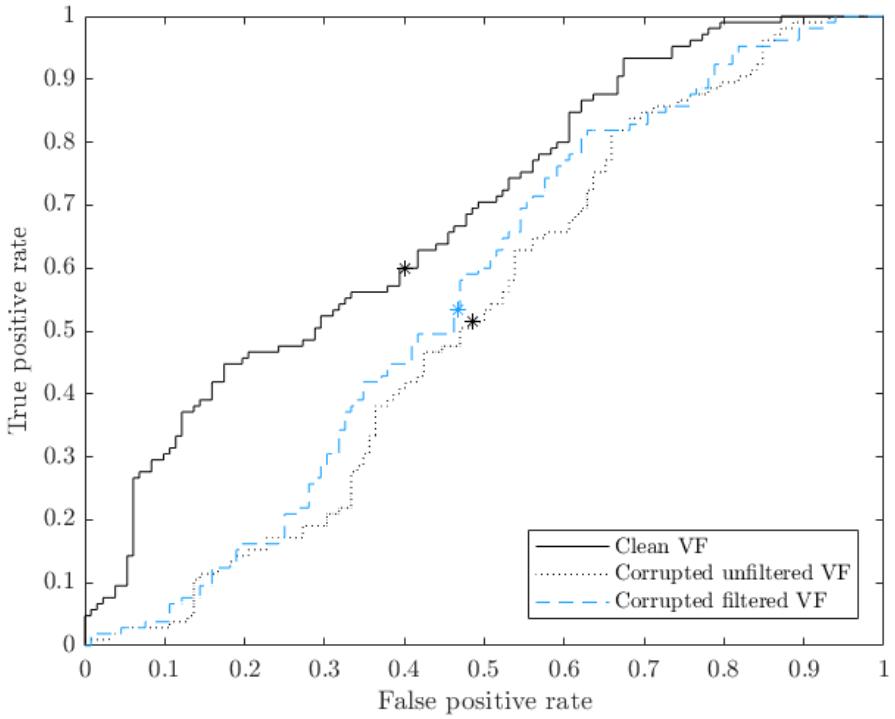

Figure 6.1. *Receiver operating characteristic (ROC) curve of the prediction of amplitude spectrum area (AMSA) for such success of early shocks (1^{st}-3^{rd}). The area under the curve (AUC) was 0.68 (0.62-0.74) for clean VF, 0.52 (0.46-0.59) for corrupted unfiltered VF, and 0.55 (0.49-0.62) for corrupted filtered VF. The asterisks indicate the points where the sensitivity and specificity were equal.*

6.4 Discussion

In this chapter we researched the predictive property of AMSA to shock success for clean pre-shock VF and pre-shock VF corrupted by CCs before and after filtering with the DL filter introduced in Section 4.5. For clean pre-shock VF, a high AMSA was associated with shock success for all shocks and for early shocks. This association was only present for early shocks in corrupted pre-shock VF segments. After filtering the association was seen for all shocks and early shocks but with a higher cut-off value compared to clean pre-shock VF segments.

Coult et al [61] also compared the predictive property of AMSA from clean and corrupted pre-shock VF to survival and shock success. In their analysis, the predictive property for survival and ROOR decreased, but was still present when corrupted segments were used. The same pattern is seen in the results of this chapter, where the association remained present, but the predictive property decreased. Coult et al calculated the predictive property separately for AMSA of clean and corrupted ECG. Ideally, the AMSA of clean and corrupted ECG would be comparable and only one cut-off value is needed. After filtering, the predictive property and cut-off values were different than for clean VF. Corrupted pre-shock VF had a significantly longer time to shock compared to clean pre-shock VF, this could explain part of the decreased relation between AMSA and shock success.

As expected, the AMSA was higher for corrupted pre-shock VF segments compared to clean pre-shock VF segments. From the previous chapter we have learned that adding a CC-artifact to clean VF increased the median AMSA with 5.18. For pre-shock VF we did not add CC-artifacts but searched for comparable segments with recorded CCs. In this chapter, the median AMSA of the corrupted VF was 6.28 higher and had a wider distribution than the AMSA of clean VF. The larger difference can have two multiple causes. First, the AMSA can be highly variable over time, two segments next to each other can have a different AMSA. The clean and corrupted pre-shock segments are not completely comparable in time to shock and can therefore have a different physiological AMSA regardless of the presence of CCs. Second, CCs were added linearly in the previous chapter, however, there may be an interaction in the ECG measurement of the cardiac rhythm and the CCs.

Filtering decreased the AMSA of the corrupted pre-shock segments with a median -3.45 (-6.82 - -1.98), which is less than the decrease of -4.64 (-7.31 - -2.78) of mixed signals in the previous chapter. This can be due to the filter that is not trained to handle corrupted signals where there is a possible interaction between the CC-artifact and the cardiac rhythm in the measurements.

The AMSA is higher after filtering compared to the clean VF segments. This again can be caused by inadequate filtering or by the possibly altered physiology during CCs. CCs create a small blood flow and might therefore also increase the perfusion of the myocardium. Increased perfusion can alter the metabolic state of the myocardium and therefore increase the AMSA. The results do not offer a conclusion if one or both mechanisms are causing the higher AMSA in corrupted filtered pre-shock VF.

6.5 Conclusion

The aim of the present research was to examine if the predictive property of AMSA of pre-shock VF remained unchanged for the AMSA calculated from filtered pre-shock VF. The association between AMSA and shock success decreased for pre-shock VF segments corrupted by CCs. The DL filter restored the VF such that the association between AMSA and shock success was present. However, the predictive value was lower and cut-off value higher for AMSA of filtered VF compared to clean VF. It is still uncertain if the difference in cut-off values is caused by inadequate filtering or a physiological mechanism where CCs improve the metabolic state of the myocardium and with that the AMSA.

CHAPTER 7

Discussion

Giving uninterrupted chest compressions is a key treatment action during cardiac arrest. However, CCs impede the interpretation of ECG which necessary for clinical decision making. In this thesis we aimed to introduce a nonlinear filter to remove the CC-artifact and improve ECG interpretation such as rhythm classification and VF waveform measurements.

Removing CCs from ECG measurements during a cardiac arrest has been proven to be a difficult task. Most published filters represent the CC-artifact in the frequency space or rely on frequency-based filter methods, even though the frequency spectra of CC-artifacts and cardiac rhythms during cardiac arrest overlap considerably. The results of the review show that rhythm classification after filtering improved for nonlinear rhythm classification. This suggests that a nonlinear transform might be more suitable than the Fourier transform for CC-artifact filtering.

In Chapter 4 we discussed two types on nonlinear transforms: the PDE driven nonlinear spectral representation and data-driven autoencoders. Both transforms can be used to filter a signal with a transfer function in the new space. The introduced filter of Section 4.5 used an autoencoder in combination with a recurrent neural network as the transfer function. The advantage of this combination is that both the transform and the transfer function are optimized based on the given data. However, it is also possible to use nonlinear spectral decomposition with a learned transfer function. Recently, Grossman et al [117] published a neural network approximation of nonlinear spectral decomposition. Such a network implicitly learns the underlying PDE much faster and can be more easily combined with a learned separation.

The introduced filter improved the signal quality (SNR) of artificially mixed signals compared to a linear Wiener filter based on an adaptive Fourier transform. However, it is uncertain what the improvement of signal quality is for corrupted ECG measurements. In Chapter 5 we attempted to judge the signal quality after filtering with a rhythm classification algorithm using the filter as a pre-processing step. However, the rhythm classification worsened after filtering for corrupted ECG as well as artificially mixed ECG signals. This shows that this rhythm classification does not correlate with SNR improvement and is therefore an unreliable method to judge signal quality. The most reliable method is manual rhythm classification because it truly evaluates the signal quality for ECG interpretation. This method is not used in this thesis because of its labor intensity.

The association between pre-shock AMSA and shock success was present for clean and filtered VF. However, the absolute values and cut-off value of AMSA differed between these groups. AMSA remained higher for the filtered group. Two main probable causes can be identified: the filter is inadequate to handle corrupted ECG because it is only trained on linearly combined signals, or the CCs increase the myocardial perfusion and therefore improve the metabolic state and increase AMSA. It is hard to validate which mechanism has the most influence on the increase in AMSA.

Evaluating the signal quality of corrupted ECG after filtering with a manual rhythm classification can give some insight into how well the filter performs on corrupted signals. However, the ideal method would be to measure the perfusion of the coronary arteries during CCs and measure the ECG directly on the myocardium. This method is very invasive and only possible in animal studies which are not completely generalizable to human cases. A noninvasive alternative is to calculate AMSA over time and evaluate the response of AMSA to CCs. If AMSA is higher after CCs and then decreases it suggests a positive influence of CCs on the metabolic state of the myocardium. Earlier studies have already shown that CCs prior to the first defibrillator shock for patients with prolonged VF can increase shock success and survival [118, 119].

The filter network does not inherently assume a certain interaction between the CC-artifact and the true ECG. However, the network must be trained with a dataset where the 'solution' is known. In this thesis we trained the network with artificially combined signals where the input signal is a linear combination of a clean ECG and a CC-artifact. Therefore, the network only learns to separate in a linear manner which might not be generalizable to real corrupted ECG measurements. The network can be

made more generalizable by training with a nonlinear combined signal. Ideally, the nonlinear combination of a glsecg and a CC-artifact must be comparable with the actual interaction during ECG measurements. To do so more information about the interaction between CCs and cardiac rhythm is needed.

CHAPTER 8

Conclusion

In this thesis we related existing linear CC-artifact filters to nonlinear alternatives, such as nonlinear spectral analysis and deep learning methods. We have proposed a deep learning-based filter from the field of audio processing. This neural network embeds a recurrent separation network in an autoencoder. The autoencoder applies a learned nonlinear transform that can be used to gain a better understanding of the ECG signal. A recurrent network then learns to separate the clean ECG signal from a CC-artifact, based on the temporal relationships in the signal.

The introduced deep learning filter significantly improved the signal to noise ratio of artificially mixed ECG signals more compared to an existing linear Fourier based filter. Furthermore, the AMSA can be calculated after filtering artificially mixed ECG signals with only a small error after filtering. The association between pre-shock AMSA and shock success remained present for filtered ECG but with a different cut-off value. It remains unclear what the added value is of the deep learning filter on measured corrupted ECG signals. To conclude, we have introduced a nonlinear deep learning method for removing chest compression artifacts from ECG measurements during cardiac arrest. This method has shown to improve the signal quality of artificially mixed ECG and can be further improved to be generalized for measured corrupted ECG.

References

[1] J.-T. Gräsner, J. Wnent, J. Herlitz, G. D. Perkins, R. Lefering, I. Tjelmeland, R. W. Koster, S. Masterson, F. Rossell-Ortiz, H. Maurer, B. W. Böttiger, M. Moertl, P. Mols, H. Alihodžić, I. Hadžibegović, M. Ioannides, A. Truhlář, M. Wissenberg, A. Salo, J. Escutnaire, N. Nikolaou, E. Nagy, B. S. Jonsson, P. Wright, F. Semeraro, C. Clarens, S. Beesems, G. Cebula, V. H. Correia, D. Cimpoesu, V. Raffay, S. Trenkler, A. Markota, A. Strömsöe, R. Burkart, S. Booth, and L. Bossaert, "Survival after out-of-hospital cardiac arrest in europe - results of the eureca two study," *Resuscitation*, vol. 148, pp. 218–226, 2020.

[2] G. D. Perkins, A. J. Handley, R. W. Koster, M. Castren, M. A. Smyth, T. Olasveengen, K. G. Monsieurs, V. Raffay, J. T. Grasner, V. Wenzel, G. Ristagno, and J. Soar, "European resuscitation council guidelines for resuscitation 2015: Section 2. adult basic life support and automated external defibrillation," *Resuscitation*, vol. 95, pp. 81–99, 2015.

[3] E. Fitzgibbon, R. Berger, J. Tsitlik, and H. R. Halperin, "Determination of the noise source in the electrocardiogram during cardiopulmonary resuscitation," *Critical Care Medicine*, vol. 30, no. 4 Suppl, pp. S148–S153, 2002.

[4] J. Eilevstjonn, T. Eftestol, S. O. Aase, H. Myklebust, J. H. Husoy, and P. A. Steen, "Feasibility of shock advice analysis during cpr through removal of cpr artefacts from the human ecg," *Resuscitation*, vol. 61, no. 2, pp. 131–41, 2004.

[5] J. Soar, J. P. Nolan, B. W. Bottiger, G. D. Perkins, C. Lott, P. Carli, T. Pellis, C. Sandroni, M. B. Skrifvars, G. B. Smith, K. Sunde, C. D. Deakin, and C. Adult advanced life support section, "European resuscitation council guidelines for resuscitation 2015: Section 3. adult advanced life support," *Resuscitation*, vol. 95, pp. 100–147, 2015.

[6] R. E. Sell, R. Sarno, B. Lawrence, E. M. Castillo, R. Fisher, C. Brainard, J. V. Dunford, and D. P. Davis, "Minimizing pre- and post-defibrillation pauses increases the likelihood of return of spontaneous circulation (rosc)," *Resuscitation*, vol. 81, no. 7, pp. 822–825, 2010.

[7] J. A. Olsen, C. Brunborg, M. Steinberg, D. Persse, F. Sterz, J. Lozano, M., M. Westfall, D. T. Travis, E. B. Lerner, M. A. Brouwer, and L. Wik, "Pre-shock chest compression pause effects on termination of ventricular fibrillation/tachycardia and return of organized rhythm within mechanical and manual cardiopulmonary resuscitation," *Resuscitation*, vol. 93, pp. 158–163, 2015.

[8] J. Christenson, D. Andrusiek, S. Everson-Stewart, P. Kudenchuk, D. Hostler, J. Powell, C. W. Callaway, D. Bishop, C. Vaillancourt, D. Davis, T. P. Aufderheide, A. Idris, J. A. Stouffer, I. Stiell, R. Berg, and I. Resuscitation Outcomes Consortium, "Chest compression fraction determines survival in patients with out-of-hospital ventricular fibrillation," *Circulation*, vol. 120, no. 13, pp. 1241–1247, 2009.

[9] I. Isasi, U. Irusta, A. Elola, E. Aramendi, U. Ayala, E. Alonso, J. Kramer-Johansen, and T. Eftestol, "A machine learning shock decision algorithm for use during piston-driven chest compressions," *IEEE Transactions on Biomedical Engineering*, vol. 66, no. 6, pp. 1752–1760, 2019.

[10] I. Isasi, U. Irusta, E. Aramendi, U. Ayala, E. Alonso, J. Kramer-Johansen, and T. Eftestol, "A multistage algorithm for ecg rhythm analysis during piston-driven mechanical chest compressions," *IEEE Transactions on Biomedical Engineering*, vol. 66, no. 1, pp. 263–272, 2019.

[11] I. Isasi, A. B. Rad, U. Irusta, M. Zabihi, E. Aramendi, T. Eftestol, J. Kramer-Johansen, and L. Wik, "Ecg rhythm analysis during manual chest compressions using an artefact removal filter and random forest classifiers," *Computing in Cardiology*, vol. 45, 2018.

[12] E. Aramendi, U. Irusta, U. Ayala, H. Naas, J. Kramer-Johansen, and T. Eftestol, "Filtering mechanical chest compression artefacts from out-of-hospital cardiac arrest data," *Resuscitation*, vol. 98, pp. 41–7, 2016.

[13] U. Ayala, U. Irusta, J. Ruiz, T. Eftestol, J. Kramer-Johansen, F. Alonso-Atienza, E. Alonso, and D. Gonzalez-Otero, "A reliable method for rhythm analysis during cardiopulmonary resuscitation," *BioMed Research International*, vol. 2014, p. 872470, 2014.

[14] C. X. Wong, A. Brown, D. H. Lau, S. S. Chugh, C. M. Albert, J. M. Kalman, and P. Sanders, "Epidemiology of sudden cardiac death: Global and regional perspectives," *Heart, Lung and Circulation*, vol. 28, no. 1, pp. 6–14, 2019.

[15] K. Patel and J. Hipskind, "Cardiac arrest." https://www.ncbi.nlm.nih.gov/books/NBK534866/, 2020. Last accessed 7 October 2020.

[16] J. Thannhauser, J. Nas, P. M. van Grunsven, G. Meinsma, H. J. Zwart, M. J. de Boer, N. van Royen, J. L. Bonnes, and M. A. Brouwer, "The ventricular fibrillation waveform in relation to shock success in early vs. late phases of out-of-hospital resuscitation," *Resuscitation*, vol. 139, pp. 99–105, 2019.

[17] R. A. Waalewijn, J. G. Tijssen, and R. W. Koster, "Bystander initiated actions in out-of-hospital cardiopulmonary resuscitation: results from the amsterdam resuscitation study (arresust)," *Resuscitation*, vol. 50, no. 3, pp. 273–9, 2001.

[18] M. Holmberg, S. Holmberg, and J. Herlitz, "Factors modifying the effect of bystander cardiopulmonary resuscitation on survival in out-of-hospital cardiac arrest patients in sweden," *European Heart Journal*, vol. 22, no. 6, pp. 511–9, 2001.

[19] I. Hasselqvist-Ax, G. Riva, J. Herlitz, M. Rosenqvist, J. Hollenberg, P. Nordberg, M. Ringh, M. Jonsson, C. Axelsson, J. Lindqvist, T. Karlsson, and L. Svensson, "Early cardiopulmonary resuscitation in out-of-hospital cardiac arrest," *New England Journal of Medicine*, vol. 372, no. 24, pp. 2307–15, 2015.

[20] Q. Tan, G. A. Freeman, F. Geheb, and J. Bisera, "Electrocardiographic analysis during uninterrupted cardiopulmonary resuscitation," *Critical Care Medicine*, vol. 36, no. 11 Suppl, pp. S409–12, 2008.

[21] A. P. van Alem, J. Post, and R. W. Koster, "Vf recurrence: characteristics and patient outcome in out-of-hospital cardiac arrest," *Resuscitation*, vol. 59, no. 2, pp. 181–8, 2003.

[22] R. W. Koster, "Refibrillation during out-of-hospital arrest: A frequent event with clinical consequences," *Signa vitae*, vol. 5, no. Suppl 1, pp. 66–68, 2010.

[23] J. Nas, J. L. Bonnes, J. Thannhauser, E. Starreveld, P. M. van Grunsven, G. Meinsma, N. van Royen, J. Smeets, M. J. de Boer, and M. A. Brouwer, "Shock success and its determinants in refractory ventricular fibrillation during out-of-hospital cardiac arrest," *Resuscitation*, vol. 130, p. e34, 2018.

[24] C. Vaillancourt, S. Everson-Stewart, J. Christenson, D. Andrusiek, J. Powell, G. Nichol, S. Cheskes, T. P. Aufderheide, R. Berg, and I. G. Stiell, "The impact of increased chest compression fraction on return of spontaneous circulation for out-of-hospital cardiac arrest patients not in ventricular fibrillation," *Resuscitation*, vol. 82, no. 12, pp. 1501–7, 2011.

[25] S. Cheskes, R. H. Schmicker, P. R. Verbeek, D. D. Salcido, S. P. Brown, S. Brooks, J. J. Menegazzi, C. Vaillancourt, J. Powell, S. May, R. A. Berg, R. Sell, A. Idris, M. Kampp, T. Schmidt, and J. Christenson, "The impact of peri-shock pause on survival from out-of-hospital shockable cardiac arrest during the resuscitation outcomes consortium primed trial," *Resuscitation*, vol. 85, no. 3, pp. 336–42, 2014.

[26] S. Cipani, C. Bartolozzi, P. Ballo, and A. Sarti, "Blood flow maintenance by cardiac massage during cardiopulmonary resuscitation: Classical theories, newer hypotheses, and clinical utility of mechanical devices," *Journal of the Intensive Care Society*, vol. 20, no. 1, pp. 2–10, 2019.

[27] W. B. Kouwenhoven, J. R. Jude, and G. G. Knickerbocker, "Closed-chest cardiac massage," *JAMA*, vol. 173, pp. 1064–7, 1960.

[28] R. F. Redberg, K. J. Tucker, T. J. Cohen, J. P. Dutton, M. L. Callaham, and N. B. Schiller, "Physiology of blood flow during cardiopulmonary resuscitation. a transesophageal echocardiographic study," *Circulation*, vol. 88, no. 2, pp. 534–542, 1993.

[29] M. L. Weisfeldt and N. Chandra, "Physiology of cardiopulmonary resuscitation," *Annual Review of Physiology*, vol. 32, pp. 435–42, 1981.

[30] S. T. Higano, J. K. Oh, G. A. Ewy, and J. B. Seward, "The mechanism of blood flow during closed chest cardiac massage in humans: transesophageal echocardiographic observations," *Mayo Clinic Proceedings*, vol. 65, no. 11, pp. 1432–40, 1990.

[31] A. C. Pell, U. M. Guly, G. R. Sutherland, D. J. Steedman, P. Bloomfield, and C. Robertson, "Mechanism of closed chest cardiopulmonary resuscitation investigated by transoesophageal echocardiography," *Journal of accident & emergency medicine*, vol. 11, no. 3, pp. 139–143, 1994.

[32] M. H. Ma, J. J. Hwang, L. P. Lai, S. M. Wang, G. T. Huang, K. G. Shyu, Y. L. Ko, J. L. Lin, W. J. Chen, K. L. Hsu, and et al., "Transesophageal echocardiographic assessment of mitral valve position and pulmonary venous flow during cardiopulmonary resuscitation in humans," *Circulation*, vol. 92, no. 4, pp. 854–61, 1995.

[33] H. Kim, S. O. Hwang, C. Lee, K. Lee, J.-Y. Kim, B. Yoo, S. H. Lee, J. Yoon, K. Choe, and A. Singer, "Direction of blood flow from the left ventricle during cardiopulmonary resuscitation in humans-its implications for mechanism of blood flow," *American heart journal*, vol. 156, pp. 1222.e1–7, 2009.

[34] P. A. Kahn, S. S. Dhruva, T. G. Rhee, and J. S. Ross, "Use of mechanical cardiopulmonary resuscitation devices for out-of-hospital cardiac arrest, 2010-2016," *JAMA Network Open*, vol. 2, no. 10, p. e1913298, 2019.

[35] L. Wik, J. A. Olsen, D. Persse, F. Sterz, J. Lozano, M., M. A. Brouwer, M. Westfall, C. M. Souders, R. Malzer, P. M. van Grunsven, D. T. Travis, A. Whitehead, U. R. Herken, and E. B. Lerner, "Manual vs. integrated automatic load-distributing band cpr with equal survival after out of hospital cardiac arrest. the randomized circ trial," *Resuscitation*, vol. 85, no. 6, pp. 741–8, 2014.

[36] S. Rubertsson, E. Lindgren, D. Smekal, O. Ostlund, J. Silfverstolpe, R. A. Lichtveld, R. Boomars, B. Ahlstedt, G. Skoog, R. Kastberg, D. Halliwell, M. Box, J. Herlitz, and R. Karlsten, "Mechanical chest compressions and simultaneous defibrillation vs conventional cardiopulmonary resuscitation in out-of-hospital cardiac arrest: the linc randomized trial," *JAMA*, vol. 311, no. 1, pp. 53–61, 2014.

[37] G. D. Perkins, R. Lall, T. Quinn, C. D. Deakin, M. W. Cooke, J. Horton, S. E. Lamb, A. M. Slowther, M. Woollard, A. Carson, M. Smyth, R. Whitfield, A. Williams, H. Pocock, J. J. Black, J. Wright, K. Han, and S. Gates, "Mechanical versus manual chest compression for out-of-hospital cardiac arrest (paramedic): a pragmatic, cluster randomised controlled trial," *Lancet*, vol. 385, no. 9972, pp. 947–55, 2015.

[38] K. Poole, K. Couper, M. A. Smyth, J. Yeung, and G. D. Perkins, "Mechanical cpr: Who? when? how?," *Critical Care (London, England)*, vol. 22, no. 1, pp. 140–140, 2018.

[39] Zoll Medical, "Autopulse reanimatiesysteem model 100 gebruikershandleiding." https://www.zoll.com/nl/producten/producthandleidingen?product=AutoPulse+Resuscitation+System, 2012. Last accessed 10 October 2020.

[40] A. Baranchuk, C. Shaw, H. Alanazi, D. Campbell, K. Bally, D. P. Redfearn, C. S. Simpson, and H. Abdollah, "Electrocardiography pitfalls and artifacts: the 10 commandments," *Critical Care Nurse*, vol. 29, no. 1, pp. 67–73, 2009.

[41] S. Kaplan Berkaya, A. K. Uysal, E. Sora Gunal, S. Ergin, S. Gunal, and M. B. Gulmezoglu, "A survey on ecg analysis," *Biomedical Signal Processing and Control*, vol. 43, pp. 216–235, 2018.

[42] D. V. M. Verhaert, J. L. Bonnes, J. Nas, W. Keuper, P. M. van Grunsven, J. L. R. M. Smeets, M. J. de Boer, and M. A. Brouwer, "Termination of resuscitation in the prehospital setting: A comparison of decisions in clinical practice vs. recommendations of a termination rule," *Resuscitation*, vol. 100, pp. 60–65, 2016.

[43] S. Ruiz de Gauna, U. Irusta, J. Ruiz, U. Ayala, E. Aramendi, and T. Eftestol, "Rhythm analysis during cardiopulmonary resuscitation: past, present, and future," *BioMed Research International*, vol. 2014, p. 386010, 2014.

[44] A. Langhelle, T. Eftestol, H. Myklebust, M. Eriksen, B. T. Holten, and P. A. Steen, "Reducing cpr artefacts in ventricular fibrillation in vitro," *Resuscitation*, vol. 48, no. 3, pp. 279–91, 2001.

[45] J. Coult, L. Sherman, H. Kwok, J. Blackwood, P. J. Kudenchuk, and T. D. Rea, "Short ecg segments predict defibrillation outcome using quantitative waveform measures," *Resuscitation*, vol. 109, pp. 16–20, 2016.

[46] J. H. Indik, M. Shanmugasundaram, D. Allen, A. Valles, K. B. Kern, R. W. Hilwig, M. Zuercher, and R. A. Berg, "Predictors of resuscitation outcome in a swine model of vf cardiac arrest: A comparison of vf duration, presence of acute myocardial infarction and vf waveform," *Resuscitation*, vol. 80, no. 12, pp. 1420–3, 2009.

[47] T. M. Olasveengen, T. Eftestol, K. Gundersen, L. Wik, and K. Sunde, "Acute ischemic heart disease alters ventricular fibrillation waveform characteristics in out-of hospital cardiac arrest," *Resuscitation*, vol. 80, no. 4, pp. 412–7, 2009.

[48] Y. Nakagawa, M. Amino, S. Inokuchi, S. Hayashi, T. Wakabayashi, and T. Noda, "Novel cpr system that predicts return of spontaneous circulation from amplitude spectral area before electric shock in ventricular fibrillation," *Resuscitation*, vol. 113, pp. 8–12, 2017.

[49] G. Ristagno, Y. Li, F. Fumagalli, A. Finzi, and W. Quan, "Amplitude spectrum area to guide resuscitation-a retrospective analysis during out-of-hospital cardiopulmonary resuscitation in 609 patients with ventricular fibrillation cardiac arrest," *Resuscitation*, vol. 84, no. 12, pp. 1697–703, 2013.

[50] Y. Nakagawa, Y. Sato, T. Kojima, T. Wakabayashi, S. Morita, M. Amino, and S. Inokuchi, "Electrical defibrillation outcome prediction by waveform analysis of ventricular fibrillation in cardiac arrest out of hospital patients," *Tokai J Exp Clin Med*, vol. 37, no. 1, pp. 1–5, 2012.

[51] L. Y. Lin, M. T. Lo, P. C. Ko, C. Lin, W. C. Chiang, Y. B. Liu, K. Hu, J. L. Lin, W. J. Chen, and M. H. Ma, "Detrended fluctuation analysis predicts successful defibrillation for out-of-hospital ventricular fibrillation cardiac arrest," *Resuscitation*, vol. 81, no. 3, pp. 297–301, 2010.

[52] J. Coult, H. Kwok, L. Sherman, J. Blackwood, P. J. Kudenchuk, and T. D. Rea, "Ventricular fibrillation waveform measures combined with prior shock outcome predict defibrillation success during cardiopulmonary resuscitation," *Journal of Electrocardiology*, vol. 51, no. 1, pp. 99–106, 2018.

[53] G. Ristagno, T. Mauri, G. Cesana, Y. Li, A. Finzi, F. Fumagalli, G. Rossi, N. Grieco, M. Migliori, A. Andreassi, R. Latini, C. Fornari, A. Pesenti, and G. Azienda Regionale Emergenza Urgenza Research, "Amplitude spectrum area to guide defibrillation: a validation on 1617 patients with ventricular fibrillation," *Circulation*, vol. 131, no. 5, pp. 478–87, 2015.

[54] T. Eftestol, L. Wik, K. Sunde, and P. A. Steen, "Effects of cardiopulmonary resuscitation on predictors of ventricular fibrillation defibrillation success during out-of-hospital cardiac arrest," *Circulation*, vol. 110, no. 1, pp. 10–5, 2004.

[55] R. G and L. R., "Real time amplitude spectrum area to guide defibrillation." https://clinicaltrials.gov/ct2/show/NCT03237910, 2017. Last accessed 7 October 2020.

[56] H. U. Strohmenger, K. H. Lindner, A. Keller, I. M. Lindner, and E. G. Pfenninger, "Spectral analysis of ventricular fibrillation and closed-chest cardiopulmonary resuscitation," *Resuscitation*, vol. 33, no. 2, pp. 155–61, 1996.

[57] Y. Gong, B. Chen, and Y. Li, "A review of the performance of artifact filtering algorithms for cardiopulmonary resuscitation," *Journal of Healthcare Engineering*, vol. 4, no. 2, pp. 185–202, 2013.

[58] R. Affatato, Y. Li, and G. Ristagno, "See through ecg technology during cardiopulmonary resuscitation to analyze rhythm and predict defibrillation outcome," *Current Opinion in Critical Care*, vol. 22, no. 3, pp. 199–205, 2016.

[59] R. E. Kerber, L. B. Becker, J. D. Bourland, R. O. Cummins, A. P. Hallstrom, M. B. Michos, G. Nichol, J. P. Ornato, W. H. Thies, R. D. White, and B. D. Zuckerman, "Automatic external defibrillators for public access defibrillation: recommendations for specifying and reporting arrhythmia analysis algorithm performance, incorporating new waveforms, and enhancing safety. a statement for health professionals from the american heart association task force on automatic external defibrillation, subcommittee on aed safety and efficacy," *Circulation*, vol. 95, no. 6, pp. 1677–82, 1997.

[60] M. T. Lo, L. Y. Lin, W. H. Hsieh, P. C. Ko, Y. B. Liu, C. Lin, Y. C. Chang, C. Y. Wang, V. H. Young, W. C. Chiang, J. L. Lin, W. J. Chen, and M. H. Ma, "A new method to estimate the amplitude spectrum analysis of ventricular fibrillation during cardiopulmonary resuscitation," *Resuscitation*, vol. 84, no. 11, pp. 1505–11, 2013.

[61] J. Coult, J. Blackwood, L. Sherman, T. D. Rea, P. J. Kudenchuk, and H. Kwok, "Ventricular fibrillation waveform analysis during chest compressions to predict survival from cardiac arrest," *Circ Arrhythm Electrophysiol*, vol. 12, no. 1, p. e006924, 2019.

[62] E. Alonso, E. Aramendi, U. Irusta, M. Daya, C. Corcuera, Y. Lu, and A. H. Idris, "Evaluation of chest compression artefact removal based on rhythm assessments made by clinicians," *Resuscitation*, vol. 125, pp. 104–110, 2018.

[63] I. Isasi, U. Irusta, E. Aramendi, U. Ayala, E. Alonso, J. Kramer-Johansen, and T. Eftestol, "Removing piston-driven mechanical chest compression artefacts from the ecg," *Computing in Cardiology*, pp. 1–4, 2017.

[64] Y. Gong, P. Gao, L. Wei, C. Dai, L. Zhang, and Y. Li, "An enhanced adaptive filtering method for suppressing cardiopulmonary resuscitation artifact," *IEEE Transactions on Biomedical Engineering*, vol. 64, no. 2, pp. 471–478, 2017.

[65] S. Babaeizadeh, R. Firoozabadi, C. Han, and E. D. Helfenbein, "Analyzing cardiac rhythm in the presence of chest compression artifact for automated shock advisory," *Journal of Electrocardiology*, vol. 47, no. 6, pp. 798–803, 2014.

[66] E. Aramendi, U. Ayala, U. Irusta, E. Alonso, T. Eftestol, and J. Kramer-Johansen, "Suppression of the cardiopulmonary resuscitation artefacts using the instantaneous chest compression rate extracted from the thoracic impedance," *Resuscitation*, vol. 83, no. 6, pp. 692–8, 2012.

[67] M. Granegger, T. Werther, and H. Gilly, "Use of independent component analysis for reducing cpr artefacts in human emergency ecgs," *Resuscitation*, vol. 82, no. 1, pp. 79–84, 2011.

[68] J. Ruiz, U. Irusta, S. Ruiz de Gauna, and T. Eftestol, "Cardiopulmonary resuscitation artefact suppression using a kalman filter and the frequency of chest compressions as the reference signal," *Resuscitation*, vol. 81, no. 9, pp. 1087–94, 2010.

[69] V. Krasteva, I. Jekova, I. Dotsinsky, and J. P. Didon, "Shock advisory system for heart rhythm analysis during cardiopulmonary resuscitation using a single ecg input of automated external defibrillators," *Annals of Biomedical Engineering*, vol. 38, no. 4, pp. 1326–36, 2010.

[70] U. Irusta, J. Ruiz, S. R. de Gauna, T. Eftestol, and J. Kramer-Johansen, "A least mean-square filter for the estimation of the cardiopulmonary resuscitation artifact based on the frequency of the compressions," *IEEE Transactions on Biomedical Engineering*, vol. 56, no. 4, pp. 1052–62, 2009.

[71] S. Ruiz de Gauna, J. Ruiz, U. Irusta, E. Aramendi, T. Eftestol, and J. Kramer-Johansen, "A method to remove cpr artefacts from human ecg using only the recorded ecg," *Resuscitation*, vol. 76, no. 2, pp. 271–8, 2008.

[72] Y. Li, J. Bisera, F. Geheb, W. Tang, and M. H. Weil, "Identifying potentially shockable rhythms without interrupting cardiopulmonary resuscitation," *Critical Care Medicine*, vol. 36, no. 1, pp. 198–203, 2008.

[73] Y. Li, J. Bisera, W. Tang, and M. H. Weil, "Automated detection of ventricular fibrillation to guide cardiopulmonary resuscitation," *Critical Pathways in Cardiology*, vol. 6, no. 3, pp. 131–4, 2007.

[74] G. Zhang, T. Wu, Z. Wan, Z. Song, M. Yu, D. Wang, L. Li, and F. Chen, "A new method to detect ventricular fibrillation from cpr artifact-corrupted ecg based on the ecg alone," *Biomedical Signal Processing and Control*, vol. 29, pp. 67–75, 2016.

[75] M. Yu, G. Zhang, T. Wu, C. Li, Z. Wan, L. Li, C. Wang, Y. Wang, H. Lu, and F. Chen, "A new method without reference channels used for ventricular fibrillation detection during cardiopulmonary resuscitation," *Australasian Physical and Engineering Sciences in Medicine*, vol. 39, no. 2, pp. 391–401, 2016.

[76] Y. Li, J. Bisera, M. H. Weil, and W. Tang, "An algorithm used for ventricular fibrillation detection without interrupting chest compression," *IEEE Transactions on Biomedical Engineering*, vol. 59, no. 1, pp. 78–86, 2012.

[77] E. Aramendi, S. R. de Gauna, U. Irusta, J. Ruiz, M. F. Arcocha, and J. M. Ormaetxe, "Detection of ventricular fibrillation in the presence of cardiopulmonary resuscitation artefacts," *Resuscitation*, vol. 72, no. 1, pp. 115–23, 2007.

[78] A. Amann, A. Klotz, T. Niederklapfer, A. Kupferthaler, T. Werther, M. Granegger, W. Lederer, M. Baubin, and W. Lingnau, "Reduction of cpr artifacts in the ventricular fibrillation ecg by coherent line removal," *BioMedical Engineering OnLine*, vol. 9, p. 2, 2010.

[79] T. Werther, A. Klotz, G. Kracher, M. Baubin, H. G. Feichtinger, H. Gilly, and A. Amann, "Cpr artifact removal in ventricular fibrillation ecg signals using gabor multipliers," *IEEE Transactions on Biomedical Engineering*, vol. 56, no. 2, pp. 320–7, 2009.

[80] K. Rheinberger, T. Steinberger, K. Unterkofler, M. Baubin, A. Klotz, and A. Amann, "Removal of cpr artifacts from the ventricular fibrillation ecg by adaptive regression on lagged reference signals," *IEEE Transactions on Biomedical Engineering*, vol. 55, no. 1, pp. 130–7, 2008.

[81] E. Aramendi, J. Ruiz, S. Ruiz De Gauna, U. Irusta, A. Lazkano, and J. Gutierrez, "A simple effective filtering method for removing cpr caused artefacts from surface ecg signals," *Computers in Cardiology*, vol. 32, pp. 547–550, 2005.

[82] U. Irusta, S. Ruiz De Gauna, J. Ruiz, E. Aramendi, A. Lazkano, and J. J. Gutierrez, "A variable step size lms algorithm for the suppression of the cpr artefact from a vf signal," *Computers in Cardiology*, vol. 32, pp. 179–182, 2005.

[83] S. Ruiz de Gauna, J. Ruiz, U. Irusta, E. Aramendi, A. Lazkano, and J. Gutierrez, "Cpr artefact removal from vf signals by means of an adaptive kalman filter using the chest compression frequency as reference signal," *Computers in Cardiology, 2005*, pp. 175–178, 2005.

[84] K. Rheinberger, M. Baubin, K. Unterkofler, and A. Amann, "Removal of resuscitation artefacts from ventricular fibrillation ecg signals using kalman methods," *Computers in Cardiology, 2005*, pp. 555–558, 2005.

[85] J. Ruiz, E. Aramendi, S. R. De Gauna, A. Lazkano, L. Leturiondo, and J. Gutierrez, "Ventricular fibrillation detection in ventricular fibrillation signals corrupted by cardiopulmonary resuscitation artifact," *Computers in Cardiology, 2003*, pp. 221–224, 2003.

[86] J. H. Husoy, J. Eilevstjonn, T. Eftestol, S. O. Aase, H. Myklebust, and P. A. Steen, "Removal of cardiopulmonary resuscitation artifacts from human ecg using an efficient matching pursuit-like algorithm," *IEEE Transactions on Biomedical Engineering*, vol. 49, no. 11, pp. 1287–98, 2002.

[87] S. O. Aase, T. Eftestol, J. H. Husoy, K. Sunde, and P. A. Steen, "Cpr artifact removal from human ecg using optimal multichannel filtering," *IEEE Transactions on Biomedical Engineering*, vol. 47, no. 11, pp. 1440–9, 2000.

[88] U. Irusta, *New signal processing algorithms for automated external defibrillators*. Thesis, University of the Basque Country, Leioa, Spain, 2010.

[89] U. Irusta, J. Ruiz, E. Aramendi, S. Ruiz de Gauna, U. Ayala, and E. Alonso, "A high-temporal resolution algorithm to discriminate shockable from nonshockable rhythms in adults and children," *Resuscitation*, vol. 83, no. 9, pp. 1090–7, 2012.

[90] F. Fumagalli, A. E. Silver, Q. Tan, N. Zaidi, and G. Ristagno, "Cardiac rhythm analysis during ongoing cardiopulmonary resuscitation using the analysis during compressions with fast reconfirmation technology," *Heart Rhythm*, vol. 15, no. 2, pp. 248–255, 2018.

[91] J. Eilevstjonn, J. Kramer-Johansen, T. Eftestol, M. Stavland, H. Myklebust, and P. A. Steen, "Reducing no flow times during automated external defibrillation," *Resuscitation*, vol. 67, no. 1, pp. 95–101, 2005.

[92] X. Zhang and X. Feng, "Multiple-step local wiener filter with proper stopping in wavelet domain," *Journal of Visual Communication and Image Representation*, vol. 25, no. 2, pp. 254–262, 2014.

[93] G. Gilboa, "A spectral approach to total variation," in *International Conference on Scale Space and Variational Methods in Computer Vision*, pp. 36–47, Springer Berlin Heidelberg, 2013.

[94] G. Gilboa, "A total variation spectral framework for scale and texture analysis," *SIAM Journal on Imaging Sciences*, vol. 7, no. 4, pp. 1937–1961, 2014.

[95] M. Burger, L. Eckardt, G. Gilboa, and M. Moeller, "Spectral representations of one-homogeneous functionals," *International Conference on Scale Space and Variational Methods in Computer Vision*, vol. arXiv:1503.05293, pp. 16–27, 2015.

[96] P. Perona and J. Malik, "Scale-space and edge detection using anisotropic diffusion," *IEEE Transactions on pattern analysis and machine intelligence*, vol. 12, no. 7, pp. 629–639, 1990.

[97] P. Baldi and K. Hornik, "Neural networks and principal component analysis: Learning from examples without local minima," *Neural Networks*, vol. 2, no. 1, pp. 53–58, 1989.

[98] E. Plaut, "From principal subspaces to principal components with linear autoencoders," *arXiv:1804.10253*, 2018.

[99] P.-S. Huang, M. Kim, M. Hasegawa-Johnson, and P. Smaragdis, "Joint optimization of masks and deep recurrent neural networks for monaural source separation," *IEEE/ACM Transactions on Audio, Speech, and Language Processing*, vol. 23, no. 12, pp. 2136–2147, 2015.

[100] M. Kolbæk, D. Yu, Z.-H. Tan, and J. Jensen, "Multitalker speech separation with utterance-level permutation invariant training of deep recurrent neural networks," *IEEE/ACM Transactions on Audio, Speech, and Language Processing*, vol. 25, no. 10, pp. 1901–1913, 2017.

[101] Y. Luo and N. Mesgarani, "Tasnet: time-domain audio separation network for real-time, single-channel speech separation," in *2018 IEEE International Conference on Acoustics, Speech and Signal Processing (ICASSP)*, pp. 696–700, IEEE, 2018.

[102] V. Dumoulin and F. Visin, "A guide to convolution arithmetic for deep learning," *arXiv:1603.07285*, 2016.

[103] Y. N. Dauphin, A. Fan, M. Auli, and D. Grangier, "Language modeling with gated convolutional networks," in *International conference on machine learning*, pp. 933–941, 2017.

[104] S. Kiranyaz, T. Ince, and M. Gabbouj, "Real-time patient-specific ecg classification by 1-d convolutional neural networks," *IEEE Transactions on Biomedical Engineering*, vol. 63, no. 3, pp. 664–675, 2015.

[105] U. R. Acharya, S. L. Oh, Y. Hagiwara, J. H. Tan, M. Adam, A. Gertych, and R. S. Tan, "A deep convolutional neural network model to classify heartbeats," *Comput Biol Med*, vol. 89, pp. 389–396, 2017.

[106] U. R. Acharya, H. Fujita, S. L. Oh, U. Raghavendra, J. H. Tan, M. Adam, A. Gertych, and Y. Hagiwara, "Automated identification of shockable and non-shockable life-threatening ventricular arrhythmias using convolutional neural network," *Future Generation Computer Systems-the International Journal of Escience*, vol. 79, pp. 952–959, 2018.

[107] J. Lei Ba, J. R. Kiros, and G. E. Hinton, "Layer normalization," *arXiv:1607.06450*, 2016.

[108] C. Weng, D. Yu, M. L. Seltzer, and J. Droppo, "Deep neural networks for single-channel multi-talker speech recognition," *IEEE/ACM Transactions on Audio, Speech, and Language Processing*, vol. 23, no. 10, pp. 1670–1679, 2015.

[109] D. P. Kingma and J. Ba, "Adam: A method for stochastic optimization," *arXiv:1412.6980*, 2014.

[110] H.-U. Strohmenger, T. Eftestol, K. Sunde, V. Wenzel, M. Mair, H. Ulmer, K. H. Lindner, and P. A. Steen, "The predictive value of ventricular fibrillation electrocardiogram signal frequency and amplitude variables in patients with out-of-hospital cardiac arrest," *Anesthesia & Analgesia*, vol. 93, no. 6, pp. 1428–1433, 2001.

[111] C. Figuera, U. Irusta, E. Morgado, E. Aramendi, U. Ayala, L. Wik, J. Kramer-Johansen, T. Eftestøl, and F. Alonso-Atienza, "Machine learning techniques for the detection of shockable rhythms in automated external defibrillators," *PLOS ONE*, vol. 11, no. 7, p. e0159654, 2016.

[112] C. Figuera, "ohca-vs-public-dbs." https://github.com/FelipeURJC/ohca-vs-public-dbs, 2016. Last accessed 10 October 2020.

[113] S. K. Goyal and J. N. Rottman, "Ventricular fibrillaiton." https://emedicine.medscape.com/article/158712-overview#a3, 2018. Last accessed 11 December 2019.

[114] J. Berdowski, R. A. Berg, J. G. Tijssen, and R. W. Koster, "Global incidences of out-of-hospital cardiac arrest and survival rates: Systematic review of 67 prospective studies," *Resuscitation*, vol. 81, no. 11, pp. 1479–87, 2010.

[115] R. W. Koster, R. G. Walker, and F. W. Chapman, "Recurrent ventricular fibrillation during advanced life support care of patients with prehospital cardiac arrest," *Resuscitation*, vol. 78, no. 3, pp. 252–7, 2008.

[116] R. W. Koster, R. G. Walker, and A. P. van Alem, "Definition of successful defibrillation," *Critical Care Medicine*, vol. 34, no. 12 Suppl, pp. S423–6, 2006.

[117] T. G. Grossmann, Y. Korolev, G. Gilboa, and C.-B. Schönlieb, "Deeply learned spectral total variation decomposition," *arXiv:2006.10004*, 2020.

[118] L. Wik, T. B. Hansen, F. Fylling, T. Steen, P. Vaagenes, B. H. Auestad, and P. A. Steen, "Delaying defibrillation to give basic cardiopulmonary resuscitation to patients with out-of-hospital ventricular fibrillation: a randomized trial," *JAMA*, vol. 289, no. 11, pp. 1389–1395, 2003.

[119] L. A. Cobb, C. E. Fahrenbruch, T. R. Walsh, M. K. Copass, M. Olsufka, M. Breskin, and A. P. Hallstrom, "Influence of cardiopulmonary resuscitation prior to defibrillation in patients with out-of-hospital ventricular fibrillation," *JAMA*, vol. 281, no. 13, pp. 1182–1188, 1999.

[120] J. Husoy and M. Abadi, "A comparative study of some simplified rls-type algorithms," *First International Symposium on Control, Communications and Signal Processing, 2004*, pp. 705–708, 2004.

APPENDIX A

Existing filter methods

A.1 Notch and comb filters

Notch and comb filters are the simplest filter methods used to remove the CC artifact. It relies on the assumption that the CC frequency is constant in the time window of analysis or completely constant when CCs are administered mechanically. The CC frequency is found from a reference signal [65] or from the ECG [77, 81]. A filter is then designed that suppresses the CC frequency (notch) or also its harmonics (comb) with a certain bandwidth.

The disadvantage of this filter type is that it assumes the CC frequency to be constant in the analyzed window which is between 4.5 and 15s. This assumption makes this filter type unsuitable for segments with CC pauses. Furthermore, the loss of signal is very high when the frequency of the ECG overlap with the CC frequency and its harmonics.

A.2 Wiener filter and iterative methods

The most used method for removing the CC artifact in literature is a special version of the Wiener filter. The schematic representation of such a filter with the use of a reference signal b is shown in Figure A.1. The reference signal b can be a measured signal or a created function. The most used option for the reference signal b is a Fourier series described in Equation 3.3, where $\phi(n)$ is a time dependent phase based on the fundamental CC-rate. The CC-rate can be fixed for a certain window or time-dependent when based on each CC instance. Using the latter will result in a more adaptive version of the Wiener filter. This type of filter is based on the assumption that the CC artifact η is strictly additive. The goal of this filter is to minimize a cost function of the difference between the actual artifact η and the estimation of the artifact $\hat{\eta}$ by adjusting the filter coefficients. With the assumption that u and (b, η) are uncorrelated, this is the same as minimizing a cost function of the difference between x and $\hat{\eta}$. The optimal filter h_* for this minimization problem is the solution of the Wiener-Hopf equations

$$\begin{bmatrix} acf_b(0) & acf_b(1) & \cdots & acf_b(M) \\ acf_b(1) & acf_b(0) & \cdots & acf_b(M-1) \\ \vdots & \vdots & \ddots & \vdots \\ acf_b(M) & acf_b(M-1) & \cdots & acf_b(0) \end{bmatrix} \begin{bmatrix} h_0 \\ h_1 \\ \vdots \\ h_M \end{bmatrix} = \begin{bmatrix} ccf_{xb}(0) \\ ccf_{xb}(1) \\ \vdots \\ ccf_{xb}(M) \end{bmatrix}. \tag{A.1}$$

Where $acf_w(k)$ is the auto correlation function of w and $ccf_{uw}(k)$ is the cross correlation function of u and w. Since u and w are both available signals, the optimal solution can be found.

Unfortunately, the direct calculation of the optimal filter is not feasible if h is chosen with a long length, due to the high computational cost. Aase et al. used a zero-order filter, where h becomes a scalar that updates every time step [87]. This simplification allows for a direct calculation of the optimal value of h without a too high computational cost. Other articles used an iterative method to find an estimate of the optimal filter coefficients such as LMS, RLS or MC-RAMP.

A.2.1 Least mean-squares

A LMS filter optimizes the coefficients of h_i for each reference signal b_i by minimizing the current quadratic cost function

$$C(h, n) = E\{\hat{x}^2(n)\} = E\left\{ \left(x(n) - \sum_i b_i^T(n) h_i(n) \right)^2 \right\}. \tag{A.2}$$

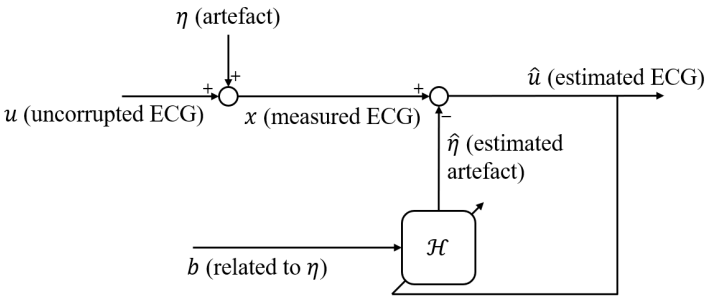

Figure A.1. *Schematic representation of a Wiener filter with reference signal b. The uncorrupted ECG signal u is corrupted by the additive CC-artifact η, which we measure as x. The filter $\mathscr{H}$ uses the reference signal b to create the estimation $\hat{\eta}$ of the artifact which is then subtracted from the measured signal x to get an estimate of the artifact free ECG $\hat{u}$.*

Each time step the filter coefficients are updated by adjusting the coefficients with a certain step size in the opposite direction as the gradient of the cost function $\nabla C(h)$. This leads to the following update steps each time step

$$h_i(n) = h_i(n-1) + 2\hat{u}(n-1)\Lambda b_i^T(n-1), \tag{A.3}$$

where Λ is the diagonal matrix with step sizes μ_k. These step sizes can be chosen and define how much the filter coefficients are changed each time step. The filter will converge to the optimal filter defined by the Wiener-Hopf equations.

Most LMS filters use Equation 3.3 for the reference signals b_i. The main differences between the articles the parameters of filtering (number of harmonics and filter order), how the CC-rate is found, and the data that is used. The recent changes that improve the performance up to the AHA standards are mainly in the method of classifying the segments after applying the LMS filtering. Two LMS articles used another reference signal. Yu et al. uses the summation of two intrinsic mode functions of the corrupted ECG found with EMD as the reference signal [75]. Gong et al. proposed multiple reference signals for the LMS filter and chose the one for each segment where the PSD correlated the most with the PSD of the corrupted ECG [64]. All candidate reference signals were derived from the TTI by differentiating or integrating the signal once or twice.

A.2.2 Recursive least squares

Four more recent articles used RLS to find an estimation of the optimal filter of the Wiener-Hopf equations [9–11, 63]. RLS is a deterministic model, whereas LMS is a stochastic model making it more suitable for time-varying signals. Moreover, RLS converges faster to the optimal solution but comes with a higher computational cost. Again the reference signals were defined as the Fourier series in Equation 3.3 but the vectors b_i and h_i were appended to create two vectors b and h. In contrast to LMS, the RLS method minimizes the total weighted cost of all past estimations instead of the current cost

$$C(h,n) = \sum_{k=1}^{n} \lambda^{n-k-1}\hat{u}^2(k) = \sum_{k=1}^{n} \lambda^{n-k-1}\left(x(k) - b^T(k)h(k)\right)^2. \tag{A.4}$$

Rather than calculating the optimal solution every time step, which is very costly, it uses a recursive algorithm where $h(n)$ is updated proportionately to $\hat{u}(n)$

$$h(n) = h(n-1) + F(n)b(n)\hat{u}(n) \tag{A.5}$$

$$F(n) = \frac{1}{\lambda}\left(F(n-1) - \frac{F(n-1)b(n)b^T(n)F(n-1)}{\lambda + b^T(n)F(n-1)b(n)}\right), \tag{A.6}$$

where F is the gain matrix. In contrast to LMS, RLS has a potentially infinite memory. The forgetting factor $0 \leqslant \lambda < 1$ regulates the importance of the older data compared to the newer data. When λ is large the model old data and new data are equally important and the system will react slowly to changes. A lower value of λ will have the effect that older samples are used less for estimating the model. The value of λ can also be adaptive such that the model will forget less when the estimations are good and forget more when the estimations are bad. The published articles all use a fixed forgetting factor [9–11]. An adaptive forgetting factor is computationally more expensive but might cope better with the start and finish of chest compressions, switching of rescuer, and switching from manual to mechanical chest compressions.

A.2.3 MultiChannel Recursive Adaptive Matching Pursuit

MC-RAMP can be interpreted as a partial RLS algorithm with a trade-off between complexity and performance [120]. It converges more slowly than RLS but is computationally more efficient. The cost function only refers to a rectangle window of length L instead of the entire past signal

$$C(h,n) = \sum_{k=n-L}^{n} \hat{u}^2(k) \tag{A.7}$$

The two articles that used MC-RAMP [4, 86] used 4 measured reference signals b_i. Reference signals included the TTI, ECG common, compression acceleration and the compression depth.

Each time step starts with an initial estimation of the uncorrupted ECG $\hat{u}_0(n)$ using the filter of the previous time step. The optimal filter coefficient $j_0(n)$ to update from all filters for each reference signal is chosen by the normalized inner product. Then, the optimal update is calculated by projecting the initial estimate $\hat{u}_0(n)$ on the corresponding selected reference vector. After updating the filter coefficients a new estimation $\hat{u}_1(n)$ is made. This procedure is then repeated for P times and the final estimate $\hat{x}(n)$ is calculated. In order to avoid rank deficiency, reference vectors with low norm are excluded from the selection process.

There are several differences between the two articles that used MC-RAMP. Eilevstjonn et al. [4] introduced four improvements on the original article of Husøy et al. [86]. Filter coefficients that correspond to a reference signal with low power or low correlation with the ECG decay to zero exponentially. Furthermore, the window length of the cost function was updated every 50 samples based on the correlation of ECG and the reference signals. Lastly, an extra low pass filter is applied to the CC artifact estimate $\hat{\eta}$ to remove frequencies above 11Hz.

A.3 Kalman filters

A Kalman filter is based on the state-space approach that describes a linear dynamical system. The goal is to estimate the state vector x that represents components of the CC artifact or the CC artifact and the uncorrupted ECG. However, the only available knowledge is a measured signal u that is often the corrupted ECG. Their relationship can be described by the state-space model

$$\begin{aligned} x(n) &= F(n)x(n-1) + v_1(n) \\ u(n) &= H(n)x(n) + v_2(n). \end{aligned} \tag{A.8}$$

F and H are the transition and observation matrix that can be fixed or variable and are defined with *a priori* knowledge. The vectors v_1 and v_2 are uncorrelated noise vectors that are normally distributed around zero with a covariance matrix of Q_1 and Q_2 respectively.

Each time step the state vector x is estimated in two steps: first predicted by Equation A.8 and then updated with the knowledge of the measured signal u as shown in Figure A.2. The prediction of x and its covariance matrix P uses only information of the previous time step and the known matrices

$$\begin{aligned} \hat{x}(n|n-1) &= F(n)x(n-1|n-1) \\ P(n|n-1) &= F(n)P(n-1|n-1)F^T(n) + Q_1(n). \end{aligned}$$

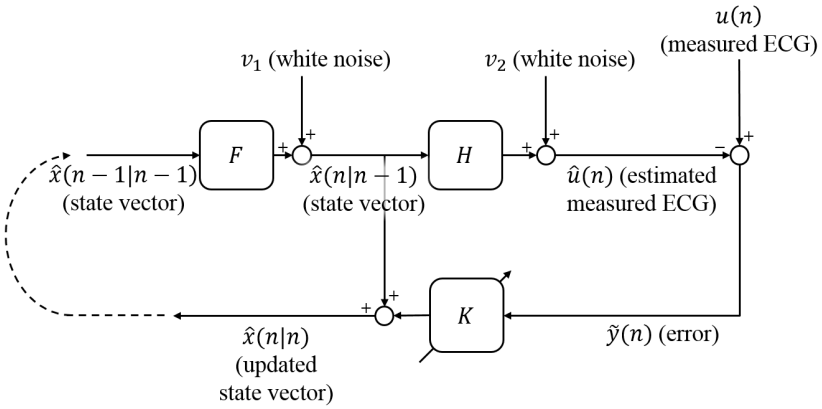

Figure A.2. *Schematic representation of a Kalman filter based on two steps. The upper rule is an estimation based on a state-space representation of the system. The lower rule updates the estimated state vector $\hat{x}$ with the Kalman gain based on the error and the covariance matrices of the state vector and the estimated measurement.*

The measured signal is used to find an optimal estimate of the state by updating the state according to the covariances of the predicted state and the measured signal.

$$\begin{aligned}
\tilde{y}(n) &= u(n) - H(n)\hat{x}(n|n-1) && \text{Error of measurement estimate}\\
S(n) &= H(n)P(n|n-1)H^T(n) + Q_2(n) && \text{Covariance of estimated measurement}\\
K(n) &= P(n|n-1)H^T(n)S^{-1}(n) && \text{Optimal Kalman gain}\\
x(n|n) &= \hat{x}(n|n-1) + K(n)\tilde{y} && \text{Update state}\\
P(n|n) &= (I - K(n)H(n))P(n|n-1) && \text{Update covariance of state}\\
\tilde{y}(n|n) &= u(n) - H(n)x(n|n) && \text{Final error of measurement estimate}
\end{aligned}$$

In most studies the state x is a vector that represents components of the CC artifact or the CC artifact and the uncorrupted ECG signal. The chosen variables differ per study but are almost always cosine and sines with variable phase and amplitude [68, 71, 83, 85]. The frequencies of the CC artifact are either based on a reference signal or on the ECG itself. In case that components of the ECG signal are also part of the state, frequencies were based on the PSD or fixed. Rheinberger et al. used a Kalman filter where the state was a vector of the last measured samples of one period. The period was variable, and the dimension of the state was set to the maximal period [84].

The two main advantages of the Kalman filter is its relatively low complexity and its ability to estimate the quality of the result in the form of the covariance matrix. However, a Kalman filter assumes Gaussian distributions and linear models. There are adaptations such as extended Kalman filter and particle filtering that can cope with non-linear models, but these are not used in CC artifact filtering.

A.4 Other indirect filters

There are three articles that use a filter method that can not be categorized in the four main used methods. These methods include Gabor multipliers, coherent line removal, and independent component analysis.

ICA is a method that finds multiple sources s such that $u = As$ with u being multiple measured signals. That means that it assumes that the measured signals are linear combinations of multiple independent sources. In the case of CC filtering, these sources are the different ECG rhythms and the CC artifact. Finding the sources can be done by different algorithms based on different minimization or maximization

problems. Granegger et al. did not provide a general solution to select the source that most closely corresponds to the clean ECG. ICA method requires the distributions to be non-Gaussian but can handle almost Gaussian distributions. The main disadvantage of this method is that it is not able to reconstruct the sign and power of the sources. Making this method unsuitable to correctly classify asystole and calculate waveforms. Another disadvantage is that this method requires at least as many input signals as possible sources. Granegger et al. used eight ECG leads, which is not applicable in a OHCA setting.

CLR, used by Amann et al. is a method that is used for removal of periodic signals with sufficiently strong harmonics. This is especially the case with mechanical chest compressions which are used in this study. CLR first finds the dominant frequency f_0 in a certain time window. The artifact is then modelled as

$$\begin{aligned} \hat{\eta}(t) &= \sum_{k=1}^{M} \alpha_k m^k(t) + \overline{\alpha_k m^k(t)} \\ m(t) &= r(t) \exp 2\pi i f_0 t \end{aligned} \tag{A.9}$$

Where α_k and $m(t)$ are calculated for each window, if no artifact is present $\alpha_k = 0$ for all k. This method is fast and does not require optimization of the parameters (number of harmonics, frequency band etc.). However, this method can not handle short periods with CCs because it works with a fixed interval of 10.24s in which the CC frequency is assumed to be constant

Wherter et al. [79] uses Gabor multipliers with IAP to remove the CC artifact. A Gabor transform or short-time Fourier transform is applied to the ECG and the IAP signal. When the transform of the IAP exceeds a certain threshold for a frequency, the transform of the ECG is set to zero for that frequency. After this alteration of the transform of the ECG an inverse transform is applied to recreate an estimate of the clean ECG. The advantage of this method is that it only filters when chest compressions are present in the small window of the Gabor transform (2.56s). Thus eliminates the need for selecting segments with only CCs or completely without CCs. A disadvantage of this method is that it removes a lot of information when the clean ECG frequencies coincide with the CC frequency or its harmonics. Unfortunately, this is the case for most ECG rhythms during cardiac arrest.

A.5 Direct methods

Direct methods do not reconstruct the uncorrupted ECG but directly apply an algorithm to categorize the rhythm or calculate its waveform features. Therefore, no additional SAA is needed. Unfortunately, these methods do not have the opportunity to visualize the uncorrupted CC. Three different methods were used in the included literature: wavelet transform, rule-based, and parameter optimization.

Li et al. reported three different variations of using the wavelet transform to identify the ECG rhythm [72, 73, 76]. The wavelet transformation is a method of describing a signal in the time-frequency domain. They selected four peak amplitudes in the wavelet transform and averaged them. If an organized rhythm is present the peak amplitudes will resemble the QRS complexes and will be similar in shape. The difference between the autocorrelation of the averaged peak amplitude and the crosscorrelation between the individual and averaged peak amplitude is a measure for the peak amplitudes resemblance. The difference is used to distinguish between organized and disorganized rhythms. If an organized rhythm is faster than 180bpm the rhythm is identified as pVT and shockable, otherwise it is non-shockable. If the rhythm is classified as unorganised, the AMSA is calculated to distinguish asystole (non-shockable) and VF (shockable).

Another direct method to categorize ECG segments into shockable and non-shockable is introduced by Krasteva *et al.* [69] They used bandpass filters in three different frequency bands and calculated six features out of the filtered ECG signals. The categorization of shockable and non-shockable rhythms is a rule-based categorization. That means that the optimal cut-off values for each feature are found and a decision is made based on the six features with respect to the cut-off values.

The latest article by Coult et al. [61] that used a direct method did not aim to categorize in shockable and non-shockable rhythms, but focused on calculating VF waveform measures. The measures such as

the median frequency and AMSA were calculated in the same way as for uncorrupted ECG. However, the parameters for calculating the measures were optimized for predicting functionally-intact survival to hospital discharge. A disadvantage of this method is that the VF waveform measures are calculated differently with and without CCs and have different cut-off values. This makes the waveform measures harder to compare between ECG segments.

APPENDIX B

An easy explanation of the DL based filter

The filter introduced in Section 4.5 is based on a neural network designed for audio separation described by Luo et al [101]. Neural networks are algorithms that can learn a given task by training with known data, such as classifying ECG segments into different rhythms. During training the network receives 'negative points' if it does the task wrong, also called the loss. Each iteration, the model-specific parameters are updated to decrease the loss. After training, the loss is minimal and the network has learned to perform a certain task.

During training of the CC filter, the model needs to 'know' what the correct ECG and CC-artifact should be. The loss that is minimized during training is defined as the difference between the outputs of the network and the real clean ECG and CC-artifact. Therefore, the network is trained with input signals that are combinations of a clean ECG signal and a ECG signal with only CCs. In that way, we know exactly what the two output signals should be.

A schematic representation of the network in Figure B.1, shows the five steps of the network. First, the input signal is cut into small pieces of 0.25s. This short segment length allows for the filtering of all clinical relevant signal lengths and (near) real-time implementation. Each piece of 0.25s is then transformed into a summation of different 'puzzle pieces' also called basis signals, where each basis signal receives a coefficient. This process is called encoding and is similar to a Fourier transform where an input signal is transformed into a summation of sine and cosine waves of different frequencies. The difference is that the basis signals are not sine waves but are learned during training. In the third step, an algorithm is trained to see temporal relations between the encoded signals. This temporal information is used to separate the encoded signals into encodings of clean ECG and the CC-artifact. Resulting into two vectors, one for clean ECG and one for the CC-artifact. The fourth step is a decoding step which is the same as encoding backward, the basis signals are added up again with their own coefficient each. Lastly, the small pieces are put after each other again to create two signals with the same length as the input signal. One represents the clean ECG and one the CC-artifact.

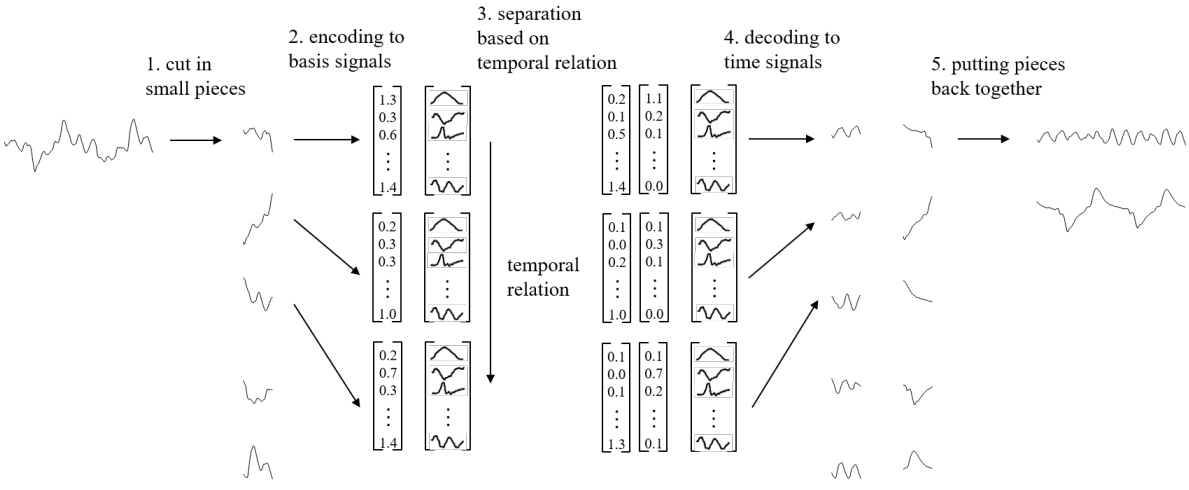

Figure B.1. *A schematic representation of the proposed deep learning filter with the five key steps.*

One of the main advantages of this filter is that the basis signals are not chosen. In other filter methods, we make assumptions on the morphology of the CC-artifact. One of the main assumptions is to represent the artifact as a summation of sine waves. However, this method does not require such an assumption because it optimizes the basis signals itself. The only set parameter is the length and amount of basis signals. Figure 4.6 shows all 400 basis signals that the network has learned. The other advantage is the

way of separation. The network does not only learn which basis signals are more common for ECG and which more common for CC-artifact. It also learns common sequences of basis signals. Therefore, it can operate near real-time with a delay in the order of 0.25s.

Filtered examples

In Chapter 5 we analyzed the signal quality of the ECG estimate after filtering by SNR, rhythm classification, and AMSA reconstruction. This Appendix gives several examples of ECG estimates after filtering of mixed segments.

Figure C.1 shows an example of asystole with a mechanical CC-artifact. The upper to graphs show the ECG and CC-artifact that are combined to create the mixed input ECG that is the input for a Wiener filter and the DL-based filter. The third and fourth row shows the ECG estimate and the CC-artifact estimate of the Wiener filter and the DL-based filter. The estimates of the Wiener filter show a short start-up time where the amplitude of the CC-artifact estimate increases. Even after the start-up time, the Wiener filter misses the sharp edges of the artifact and creating a spike-like rest-artifact in the ECG estimate. The DL-based filter does not leave any large visible rest-artifacts.

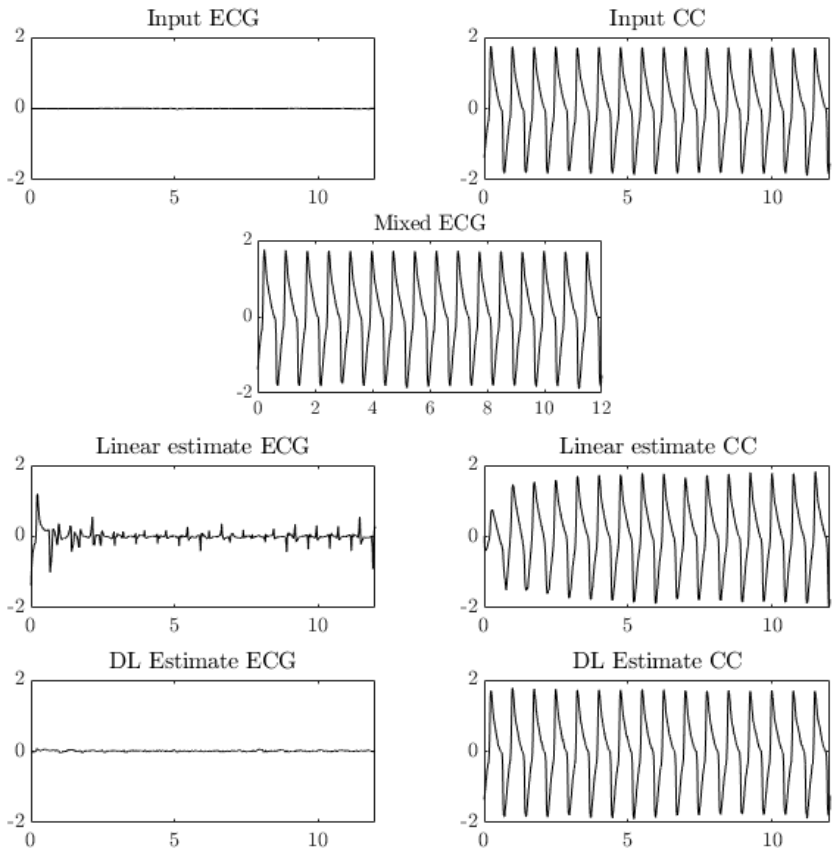

Figure C.1. *Example of filtered mixed ECG with asystole. Input SNR of -50.7, linear ECG estimate -35.2, and the DL ECG estimate -16.5*

An example of OR with a mechanical CC-artifact is shown in Figure C.2. The cardiac rhythm is a bradycardia with a narrow QRS complex. The estimate of the Wiener filer show a short start-up time as with the previous example. In both ECG estimates there are still some small disturbances and both fail to show the ST depression. However, the visual signal quality and SNR is better after DL filtering

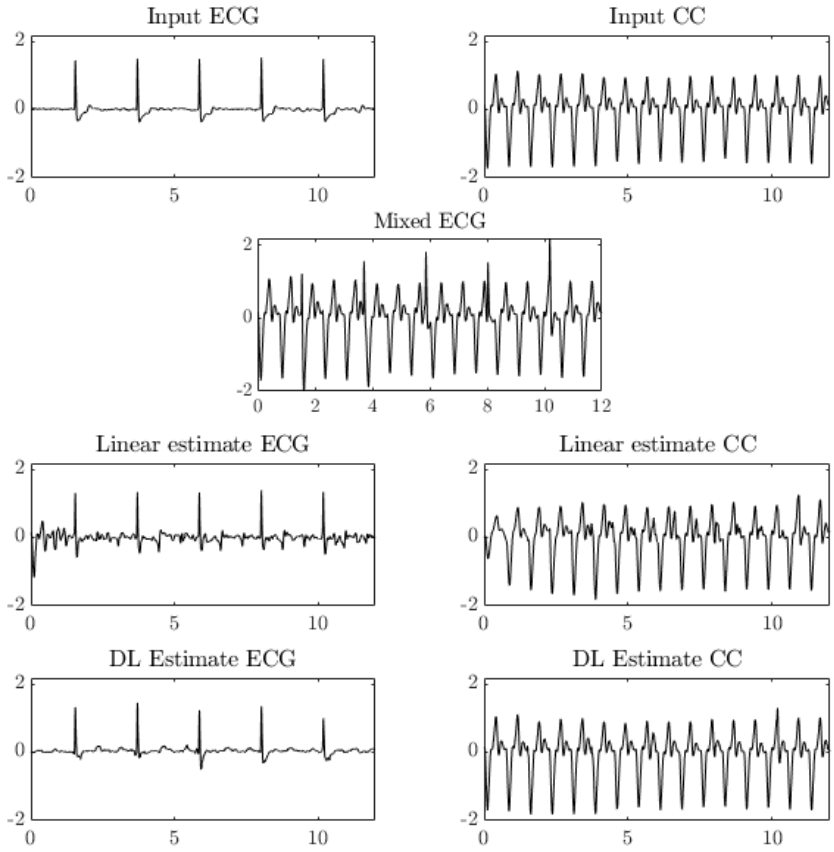

Figure C.2. *Example of filtered mixed ECG with an organized rhythm. Input SNR of -11.0, linear ECG estimate 1.1, and the DL ECG estimate 6.4*

Lastly, an example of VF with a mechanical CC-artifact is shown in Figure C.3. Both CC-artifact estimates visually resemble the real CC-artifact and both show a short start-up time. The ECG estimates both show a VF ECG but with different amplitudes and a different AMSA. This shows that the Wiener filter tends to remove too little and the DL filter too much. The DL filter behaves like a low-pass filter, because high frequency disturbances are not represented by the 400 basis signals.

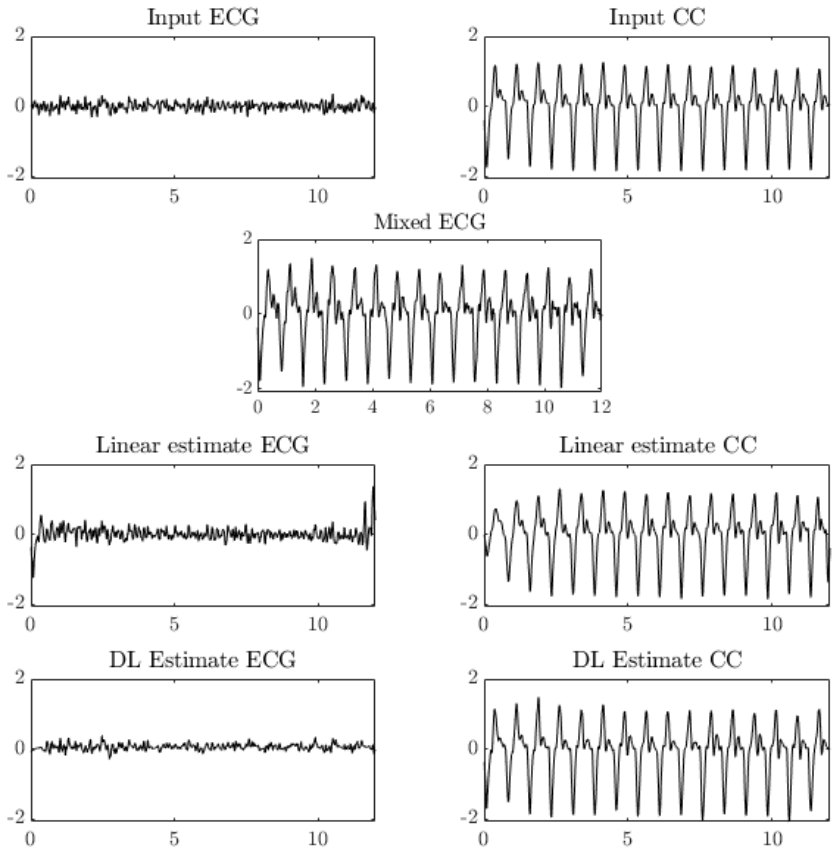

Figure C.3. *Example of filtered mixed ECG with ventricular fibrillation. Input SNR of -16.3, linear ECG estimate -4.4, and the DL ECG estimate 0.8. Input AMSA of 11.1, linear ECG estimate 13.1, and the DL ECG estimate 8.3*